Understanding Protostellar Jet Feedback on Disc and Cloud Scales

Christopher Andrew Nolan

A thesis submitted for the degree of

Doctor of Philosophy

of The Australian National University

Australian National University

Research School of Astronomy & Astrophysics

Submitted 13th April 2019

Disclaimer

I hereby declare that the work in this thesis is that of the candidate alone, except where indicated below or in the text of the thesis. The work was undertaken between February 2012 and March 2019 at The Australian National University, Canberra. It has not been submitted in whole or in part for any other degree at this or any other university.

Chapters 2, 3, and 4 have been submitted, accepted, or published as papers in *Monthly Notices of the Royal Astronomical Society* (*MNRAS*). No permission is required to include these articles in a thesis, provided the thesis is not published commercially (https://academic.oup.com/journals/pages/authors/authors_faqs/online_licensing#seven).
Therefore, commercial publication of any part of this thesis is strictly prohibited.

The 1.5D vertical disc-wind model used in Chapters 2 and 3 were provided in their original form by Dr Raquel Salmeron of The Research School of Astronomy and Astrophysics, The Australian National University. This model was adapted into a 1+1.5D configuration by the candidate, including extensive additions to the structure and complexity of the 1.5D model itself. All subsequent models employing the 1.5D and 1+1.5D models were performed by the candidate.

The Fyris Alpha shock-capturing code (Sutherland 2010) used in Chapter 4 was constructed by Dr Ralph Sutherland of The Research School of Astronomy and Astrophysics, The Australian National University. The simulations performed using this code were conducted by the candidate.

The theoretical model included in Chapter 4 was derived by Dr Christoph Federrath of The Research School of Astronomy and Astrophysics, The Australian National University, and the section of the discussion that refers to this model was also written by Dr Federrath. The remainder of Chapter 4 was written by the candidate.

For stylistic reasons, and as an acknowledgement of the status of Chapters 2, 3, and 4 as collaborative papers, this thesis retains the use of the pronoun 'we'. The text of each chapter was written solely by the candidate (except for the parts mentioned in the above paragraph), with input and review by the supervisory panel and collaborators.

Due to the nature of published papers, there is some unavoidable duplication between the main chapters. I have endeavoured, as far as is possible, to avoid unnecessary duplication between the main chapters and the thesis introduction and conclusions.

Christopher Andrew Nolan

17th December 2019

Acknowledgments

There are so many people involved in the process of writing a thesis, and I am no exception. I have a list as long as my arm of people that I would like to thank for getting me through this last seven years, and on this page I will try to do them justice.

First and foremost I would like to thank my amazing supervisory panel, consisting of Raquel Salmeron, Christoph Federrath, Geoff Bicknell and Ralph Sutherland. Each one of you has put an enormous amount of time into my thesis, through meetings, discussions, emails and paper revisions. I can't thank you enough. Without your encouragement and guidance I never would've made it this far, and that is simply a fact.

I would also like to thank all of the staff at The Research School of Astronomy & Astrophysics (RSAA) for their direct or indirect contributions which have helped me arrive at this point. Special thanks to Gary Da Costa and Astrid Bardelang for making sure I submitted all my paperwork on time (or helping to smooth things over when I didn't), and to Bill Roberts and Chris Delfs for employing me when my scholarship ran out. The RSAA IT Section have become a home for me, and I am really going to miss our morning and afternoon tea breaks!

Thanks to my officemates, Chris Owen and Luke Shingles, and fellow PhD inmates in the early years, Shaheen Iqbal, Cherie Fishlock, Tammy Roderick and Louise Howes, for making the PhD life so much easier by your friendship. I know that the bonds we forged back then will last the test of time. Similar thanks to all of the other students at RSAA who I have enjoyed the company of over the years.

Thanks to Paola Caselli for allowing me to finalize the corrections during my first few months at MPE. Thank you for your understanding!

A special thanks to all of my family and friends. Some of you have put up with PhD Chris for as long as I've known you, and I sincerely appreciate your patience with me!

I would like to thank my son Joel for all the Daddy time he has sacrificed for me to finish this thesis. While it's been hard on us both, you've given me so much joy these last two and a half years.

I would also like to thank my daughter Scarlett for all her smiles whenever she sees Daddy. You've helped get me through these last few months of corrections!

Lastly, I would like to thank my lovely wife Lily for supporting me on this long journey of

discovery. Through the development of the thesis we have courted, become engaged, married and had two children! She has stood by me in the joyful times and the dark times, and supported me even when my studies have resulted in us not seeing much of each other for months on end. I am so thankful for having you here with me Lily, and look forward to our post-PhD life together!

Abstract

Protostellar jets are a vital part of the star formation process. They are responsible for the removal of excess angular momentum critical to the growth of protostars, while feeding that angular momentum back into molecular clouds to regulate the formation of stellar cores and gravitational collapse. To better understand the origin and impact of protostellar jets, this thesis investigates the launching of protostellar disc winds and the driving of non-isothermal turbulence in the interstellar medium.

In the first part of this thesis, we explore how the structure of protostellar discs relates to the properties of the wind-launching region, which directly effects the large-scale properties of the jet. In order to study the launching of disc winds, we first design a 1+1.5D magnetohydrodynamic (MHD) model of the launching region in the [r,z] plane. We take into account the three diffusion mechanisms of non-ideal MHD (Ohm, Hall, and ambipolar) by calculating their contributions at the disc midplane and using a simplified, vertically-scaled approach for higher z. We observe that most of the mass launched by the wind is concentrated within a radially localized region a fraction of an astronomical unit (au) in width, in agreement with current observations. We find that the footprint radius and the wind efficiency, measured by the ratio of the wind mass-loss rate to the rate of material accreted onto the star, are a strong function of the model parameters, namely the mass accretion rate, magnetic field strength, and surface density profile of the disc. Understanding the structure of the wind-launching region has important

We subsequently improve the 1+1.5D models by removing the vertical scaling approximation to the non-ideal MHD terms and calculate the magnetic diffusivities self-consistently at all heights above the disc midplane. This results in increased field-matter coupling surrounding the midplane, increasing the poloidal magnetic field bending and compressing the disc via enhanced magnetic pressure gradients. It also shifts the wind-launching region to smaller radii, decreases the overall wind mass-loss rate by an order of magnitude, and generates a radially symmetric wind mass-loss profile.

In the second part of this thesis, we investigate the properties of driven, turbulent, adiabatic gas. The density variance–Mach number relation of the turbulent interstellar medium is a key ingredient for analytical models of star formation. We examine the robustness of the standard, isothermal form of this relation in the non-isothermal regime, specifically testing ideal gases with diatomic molecular and monatomic adiabatic indices. Stirring the gas with purely solenoidal

forcing at low wavenumbers, we find that as the gas heats in adiabatic compressions, it evolves along a curve in the density variance-Mach number plane, but deviates significantly from the standard isothermal relation. We provide new empirical and theoretical relations that take the adiabatic index into account and provide good fits for a range of Mach numbers.

Contents

List of Figures

List of Tables

CHAPTER 1

Introduction

> The scientist does not study nature because it is useful to do so. He studies it because he takes pleasure in it, and he takes pleasure in it because it is beautiful. If nature were not beautiful, it would not be worth knowing, and life would not be worth living. I am not speaking, of course, of the beauty which strikes the senses, of the beauty of qualities and appearances. I am far from despising this, but it has nothing to do with science. What I mean is that more intimate beauty which comes from the harmonious order of its parts, and which a pure intelligence can grasp.
>
> – Henri Poincaré[1]

Protostellar jets and winds are a ubiquitous feature of star formation (McKee & Ostriker 2007). They are observed during the formation of stars of all stellar masses, from brown dwarfs (e.g. Whelan et al. 2005, 2012) to high-mass stars (e.g. Zhang et al. 2007; Qiu et al. 2007, 2008; Carrasco-González et al. 2010; Qiu et al. 2011; Motogi et al. 2013), and at all stages of protostellar evolution, from the embedded phase (Class 0) all the way to the classical stage (Class II, e.g. Bodenheimer 2011; Frank et al. 2014). These outflows are directly correlated with accretion onto young stellar objects (YSOs; e.g. Cabrit 2007; Watson et al. 2016), and are now thought to be the prime means of angular momentum removal from these systems, given that the magnetorotational instability

[1] *Science and Method* 1914, pp22, as translated by Francis Maitland. (Poincaré 1914).

(MRI, Balbus & Hawley 1991; Balbus & Hawley 1998) has been shown to be relatively ineffective at transporting angular momentum in the inner regions of protostellar discs (e.g. Turner et al. 2014). Recent studies have found that high speed jets may extend out to parsec scales (e.g. Frank et al. 2014), depositing angular momentum back into the surrounding molecular clouds and regulating further star formation (Federrath 2015).

Within protostellar systems, outflows are coupled to the discs that they are launched from: they play a significant role in shaping protostellar discs (e.g. Bans & Königl 2012; Bai 2017; Suriano et al. 2017, 2018; Simon et al. 2018), substantially influencing the distribution of dust and gas involved in the formation of planets (e.g. Dullemond et al. 2007)[2], while also interacting with the surrounding environment at a range of scales (Frank et al. 2014). Hence understanding their origin and influence is critical to understanding star formation as a whole.

These outflows arise as a result of contributions from a number of launching mechanisms of magneto-centrifugal origin (e.g. Frank et al. 2014). Which one of these mechanisms dominates the flow is still unclear. However, in recent years observational studies have shown increased support for disc winds as the most likely candidate to account for the majority of the outflow (e.g. Watson et al. 2016; Banzatti et al. 2019). There are two main approaches to modelling disc winds in the literature. At large scales, time-dependent simulations are able to capture global effects, but simplify the driving mechanism, which occurs at much smaller scales within the disc (e.g. Ouyed & Pudritz 1997a,b; Casse & Keppens 2002, 2004; Zanni et al. 2007; Sheikhnezami et al. 2012). In a complementary approach, steady-state semi-analytical models address disc winds from the opposite end: they model the driving mechanism, but do not incorporate fully the global effects (e.g. Wardle & Königl 1993; Königl et al. 2010; Salmeron et al. 2011; Teitler 2011; Bai 2016). These steady-state models include non-ideal MHD effects and have been used to study the vertical structure of wind-driving protostellar discs for a given radial location, however, no study to date has used these models to investigate how the wind-launching region changes with radius.

At larger scales, jets drive supersonic turbulence in molecular clouds (Krumholz et al. 2014). This has a dual effect: on the one hand, supersonic turbulence replenishes regions of high density, creating sites for subsequent gravitational collapse and the formation of stars, while on the other, turbulent kinetic energy stabilizes molecular clouds against gravitational collapse (Elmegreen

[2]Outflows can stir up dust grains and counteract the settling process, in turn impacting on the magnetic diffusion and chemistry within the disc.

& Scalo 2004; Mac Low & Klessen 2004; McKee & Ostriker 2007). As a result, a thorough understanding of supersonic turbulence, specifically the relationship between the driving of the turbulence and the hierarchical density structure of molecular clouds, is key for models of star formation. While this has been studied extensively for the general case of isothermal clouds (e.g. Padoan et al. 1997; Passot & Vázquez-Semadeni 1998; Kritsuk et al. 2007; Beetz et al. 2008; Federrath et al. 2008b; Price et al. 2011; Burkhart & Lazarian 2012; Konstandin et al. 2012; Seon 2012), to date no investigation has been performed into the behaviour of adiabatic gases, which are important in the case of molecular clouds of hydrogen (Mac Low & Klessen 2004).

In this thesis, we investigate the origin and influence of protostellar jets on their surrounding environment using advanced numerical simulations. Firstly, we develop the first 1+1.5D model including all three non-ideal MHD effects (Ohm, Hall, and ambipolar), in order to investigate how disc structure relates to the properties of the wind-launching region (Chapter 2). This is achieved by coupling a series of vertical 1.5D models together in the radial direction using mass conservation. Employing this model, we are able to investigate the radial extent and ejection/accretion ratio ($\dot{M}_{\rm out}/\dot{M}_{\rm in}$, the ratio of the rate of material lost in the wind to the rate of material accreted onto the star) of these winds and compare with constraints provided by observations of outflows in protostellar systems. We find good agreement with observations regarding these two wind characteristics, whilst also demonstrating that winds are inherently radially localized as a result of the magnetic field and ionization structure of the disc, and show that the position and ejection/accretion ratio of these winds are highly dependent on the properties of the disc. We also find that the location and structure of disc winds are highly dependent on the vertical profile of the magnetic diffusion coefficients (Chapter 3), with weaker diffusion above the midplane leading to enhanced field bending and disc compression, lower mass loss rates and a launching region closer to the central star.

Secondly, we investigate the properties of driven turbulence in the adiabatic regime (Chapter 4) in the first ever study of its kind. Specifically, we measure the dependence of the density variance–Mach number relation on the adiabatic exponent of the turbulent gas. We find that adiabatic turbulence is inherently distinct from the isothermal case, with the injection of energy via turbulent driving continuously increasing the temperature of the gas. We also calculate new prescriptions for the density variance–Mach number relation including the adiabatic exponent, for a range of Mach numbers.

In the remainder of this chapter, we provide a brief overview of protostellar outflows (Section 1.1),

including diagnostics for determining the origin of outflows (Section 1.1.1), the different launching mechanisms that could account for these outflows (Section 1.1.2), and discriminating observational evidence (Section 1.1.3), as well as a summary of the latest numerical models of disc winds (Section 1.1.4). We then provide an outline of driven interstellar turbulence and its role in star formation (Section 1.2), including the derivation of the star formation rate (Section 1.2.1) and an overview of qualitative relations of turbulence discovered through the use of numerical simulations (Section 1.2.2). In Section 1.3 we outline the structure of the thesis.

1.1. Protostellar outflows

Outflows are a ubiquitous feature of protostellar systems (McKee & Ostriker 2007; Frank et al. 2014). They are commonly observed out to parsec scales (Eisloffel & Mundt 1997; Reipurth et al. 1997; Stanke et al. 2000; McGroarty et al. 2004), with opening angles dropping from 20–30 degrees initially to a few degrees beyond 50 au of the source (Cabrit 2007; Frank et al. 2014). Although they vary considerably in their morphology, outflows typically consist of an 'onion-like' structure, with a narrow, high speed ($\sim$ 100–1000 km s^{-1}) jet surrounded by a slower, wide-angle wind ($\sim$ 1–30 km s^{-1}; Frank et al. 2014). This layered configuration was first discovered in observations of the accreting young star DG Tauri, and has been observed in all cases where the jet base can be resolved laterally (Beck et al. 2007; Coffey et al. 2008; Pyo et al. 2009; Agra-Amboage et al. 2011; Frank et al. 2014). The onion-like shape can be explained by either a range of launch radii in a MHD disc wind (Agra-Amboage et al. 2011), or a magnetospheric wind surrounded by a disc wind (Pyo et al. 2009). Turbulent mixing and entrainment of the high speed jet may also contribute to this low-velocity 'sheath' (Pyo et al. 2003; Garcia Lopez et al. 2008; López-Cámara & Raga 2010).

Mass loss rates from outflows are tightly correlated with disc accretion (e.g. Bally et al. 2007; Frank et al. 2014), expelling roughly 0.1–0.2 times the amount of material accreted onto the star (e.g. Cabrit 2007; Ellerbroek et al. 2013; Watson et al. 2016). This correlation, combined with the prevalence of outflows across protostellar mass and age (e.g. Frank et al. 2014) indicates a universal mechanism responsible for jet launching driven by accretion. Early studies quickly realized that the momentum observed in protostellar jets could not be explained by radiation pressure alone (Lada 1985), nor by thermal pressure, as the high temperatures required are not observed at the base of the outflow (e.g. Glassgold et al. 2004). This led to the consensus that

outflows are the result of the interaction between the accreting flow and the stellar and/or disc magnetic fields (McKee & Ostriker 2007; Frank et al. 2014).

1.1.1. Observational constraints

The launching of outflows can be accounted for by a number of magneto-centrifugal mechanisms, however their exact origin is still a hotly debated topic. Each of these possible mechanisms (stellar winds, X-winds, and disc winds) generate slightly different characteristic outflows, and observational studies take advantage of these differences in order to try to determine the contribution of each mechanism (e.g. Ferreira et al. 2006; Watson et al. 2016). Two important diagnostics for distinguishing the contributions of different magneto-centrifugal mechanisms to large scale outflows are the ejection/accretion ratio $\dot{M}_{\rm out}/\dot{M}_{\rm in}$ – the ratio of the wind mass-loss rate ($\dot{M}_{\rm out}$) to the rate of material accreted onto the star ($\dot{M}_{\rm in}$) – and the footprint radius of the wind (r_0). We now summarize our current knowledge about these two quantities, followed by a discussion of the different launching mechanisms and their expected values for $\dot{M}_{\rm out}/\dot{M}_{\rm in}$ and r_0 in Section 1.1.2.

The ejection/accretion ratio

As noted by Königl & Pudritz (2000), the ejection/accretion ratio of disc winds is approximated by:

$$\frac{\dot{M}_{\rm out}}{\dot{M}_{\rm in}} \simeq \left(\frac{r_0}{r_{\rm A}}\right)^2, \tag{1.1}$$

where $r_{\rm A}$ is the cylindrical radius of the field line anchored to the disc at r_0, where the flow velocity exceeds the Alfvén velocity. This condition assumes that the rate of angular momentum transport by the wind ($\sim \dot{M}_{\rm out}\Omega_0 r_{\rm A}^2$) equals the rate of angular momentum advected inward by the accretion disc ($\sim \dot{M}_{\rm in}\Omega_0 r_0^2$), where Ω_0 is the angular velocity of the matter at the disc midplane. Equation (1.1) involves the magnetic lever arm parameter

$$\lambda = \left(\frac{r_{\rm A}}{r_0}\right)^2, \tag{1.2}$$

a measure of the magnetic lever arm braking the rotating disc. This parameter is essential to models of MHD winds and jets, and efforts have been made to constrain λ through observations (e.g. Bacciotti et al. 2002; Ferreira et al. 2006).

The footprint radius

Many key properties of outflows are constants along magnetic field lines as a consequence of the conservation equations of MHD; this allows the derivation of the radial anchor point on the disc or star from which the flow originates, given relatively few observed quantities (see equation 1.4). For magneto-centrifugally driven axisymmetric winds, the specific energy of the flow, defined by:

$$E = \frac{1}{2}(v_{\rm p}^2 + v_\phi^2) + h + \phi + \Omega_0(\Omega_0 r_{\rm A}^2 - \Omega r^2), \tag{1.3}$$

is constant along field lines (e.g. Königl & Pudritz 2000; Königl & Salmeron 2011; White et al. 2014). Here h is the specific enthalpy, ϕ is the gravitational potential, r is the cylindrical radius from the central star, Ω is the angular velocity, and $v_{\rm p}$ and v_ϕ are the poloidal and azimuthal velocities of the flow, respectively. For cold gas at large distances from the disc, the enthalpy and gravitational terms can be neglected. Assuming that $E \approx v_{\rm p,\infty}^2/2$ as $r \to \infty$, where $v_{\rm p,\infty}$ is the poloidal velocity of the jet at large distances from the star, that $(r_{\rm A}/r_0) \gg 1$, and that $\Omega_0 = v_{\rm K}/r_0$, where $v_{\rm K} = (GM_*/r_0)^{1/2}$ is the disc Keplerian velocity, the asymptotic poloidal velocity can be approximated by

$$v_{\rm p,\infty} \simeq \sqrt{2} v_{\rm K} \left(\frac{r_{\rm A}}{r_0}\right) = \sqrt{2} \left(\frac{GM_*}{r_0}\right)^{1/2} \left(\frac{r_{\rm A}}{r_0}\right). \tag{1.4}$$

In terms of physical parameters, equation (1.4) can be expressed as

$$v_{\rm p,\infty} \simeq 133 {\rm km\ s^{-1}} \left(\frac{r_0}{0.1\ {\rm au}}\right)^{-1/2} \left(\frac{M_*}{M_\odot}\right)^{1/2} \lambda^{1/2}, \tag{1.5}$$

therefore, if we can measure observationally the poloidal velocity, $v_{\rm p,\infty}$, stellar mass, and ejection/accretion ratio, we are able to derive the footprint radius using equations (1.1) and (1.5).

1.1.2. Launching mechanisms

As mentioned in Section 1.1.1, there are a number of different possible mechanisms which can account for the launching of outflows, each one operating at a different radial location in the star-disc system. As we explain below, stellar winds can launch from the stellar surface, MHD disc winds from outside the truncation region of the disc, and X-winds in the region in-between.

Stellar winds

At the centre of young stellar systems, protostars rotate exceptionally slowly given the amount of angular momentum they accumulate via accretion (e.g. Bouvier et al. 2014). For many decades,

stellar winds have been theorized to remove this angular momentum directly from the stellar surface (e.g. Shu et al. 1988), accounting for the slow rotation while also launching powerful outflows (e.g. Matt & Pudritz 2005; Matt et al. 2012). The precise mechanism driving stellar winds is still unknown, however the 1D models of Cranmer (2008, 2009) suggest that the energy released by variable accretion drives MHD waves. These waves travel from the accretion hot-spots on the stellar surface to the polar regions, leading to enhanced MHD wave activity and stellar winds. If the winds are driven by accretion (accretion-powered stellar winds; APSWs), then the accretion luminosity – which is often used as a diagnostic for protostellar accretion rates (e.g. Frank et al. 2014) – is a fraction of the total accretion power incident on the stellar surface. Matt & Pudritz (2008) calculated an upper bound to the ejection/accretion ratio of $\dot{M}_{\rm out}/\dot{M}_{\rm in} \lesssim 0.6$, noting that if the mass outflow rate is too high, there will not be enough accretion power to launch a wind. Zanni & Ferreira (2011) demonstrated that APSWs require substantial large-scale magnetic fields in order to be efficient, however the observed fields are only just enough to meet the minimum requirements (see Gregory et al. 2012). Therefore, while APSWs are a viable option for the launching of jets and spin-down of protostars, they are unlikely to be the sole mechanism responsible (Zanni & Ferreira 2011).

X-winds

Moving outwards from the star, X-winds harness the magnetic interaction of the stellar magnetosphere and the surrounding disc to explain the slow spin rates of accreting protostars. Fig. 1.1 shows the general picture of an X-wind (Shu et al. 2000): all of the stellar magnetic flux initially threading the entire disc is trapped within a narrow annulus (X-region) at the disc inner edge. This region surrounds the co-rotation radius R_X, the point where the disc and stellar angular velocities are equal. At this point magnetic energy dominates due to the concentration of magnetic flux, and hence the entire X-region rotates as one solid body. As a result, disc material slightly interior to R_X rotates at sub-Keplerian velocities given its place in the disc, and can easily transfer onto sufficiently inward bending magnetic field lines and accrete onto the protostar. Conversely, disc material slightly exterior to R_X rotates at super-Keplerian velocities, allowing it to ascend open field lines bent sufficiently outwards and escape into a wind (Bouvier et al. 2014).

As material accretes, angular momentum is transferred to disc material at the inner edge of the X-region, pushing it outwards. Conversely, as a wind is launched, angular momentum is removed from material at the outer edge of the X-region, allowing it to fall inwards. This

effectively pinches the material in the X-region, trapping it there. The net result of the entire process is that angular momentum is transferred from accreting material into a wind.

There is now significant evidence for the generalized form of the X-wind model (Johns-Krull & Gafford 2002; Mohanty & Shu 2008; Cauley et al. 2012), which removes the assumption of a dipolar field. However, support from numerical simulations is varied (Romanova et al. 2007; Long et al. 2007, 2008). X-wind theory can at best only represent the time-averaged behaviour of a time-varying system, hence more numerical simulations are required to confirm the validity and importance of this mechanism (e.g. Romanova et al. 2011; Long et al. 2011).

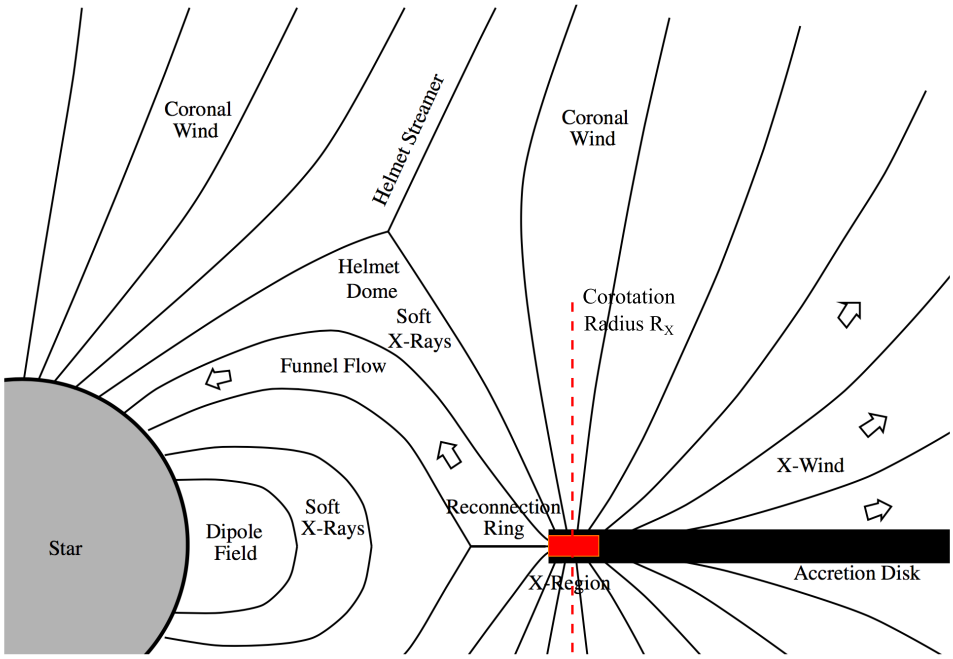

Figure 1.1 Schematic diagram of the X-wind model (Shu et al. 2000). The stellar magnetic flux is contained within a small region (X-region; red square) at the disc inner edge, which rotates as a solid body due to magnetic pressure. Magnetic torques allow infalling material to transfer angular momentum to the X-region, and then onwards to the X-wind. *Sourced from* http://adsabs.harvard.edu/abs/2000prpl.conf..789S.

MHD disc winds

At larger radii within the disc itself, winds can be launched through magneto-centrifugal acceleration, independent of the stellar magnetic field. Discs are dynamically cold and thin, so winds cannot be accelerated to escape speed by thermal processes alone (Turner et al. 2014). However, winds may be accelerated using rotational energy extracted from a large scale magnetic field anchored in the disc.

The vertical structure of a disc wind can be separated into three regions (Fig. 1.2): a quasi-hydrostatic region surrounding the disc midplane, where matter dominates and mass accretion and field bending occur; a transition zone, where the flow changes from accretion to outflow and becomes magnetically dominated; and an outflow region corresponding to the base of the wind (Wardle & Königl 1993; Königl & Salmeron 2011).

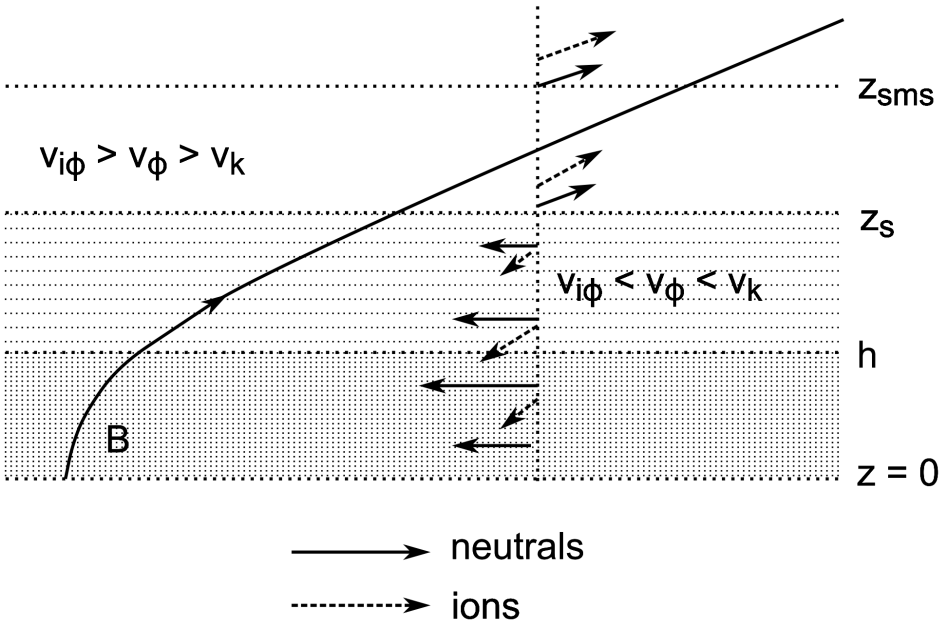

Figure 1.2 Schematic diagram of a disc wind, including the layered structure bounded by the midplane ($z = 0$), the disc scaleheight (h), the disc surface (z_s), and the sonic/slow magnetosonic point (z_{sms}) (Königl & Salmeron 2011). *Sourced from* https://arxiv.org/abs/1004.1875.

- *Quasi-hydrostatic region*: The region surrounding the disc midplane is matter dominated, with the magnetic field and ionized component carried around by the neutral gas. The magnetic field – which is anchored high up in the surrounding cloud – provides a torque on the ionized particles, slowing them down. The ions lag behind the neutrals, therefore collisional drag leads to the transfer of angular momentum from the neutrals to the ionized component, which is coupled to the magnetic field. Thus the neutrals transfer angular momentum to the field lines, creating an enhanced azimuthal field above the disc. This allows the neutrals to drift inwards, exerting a radial drag on the field lines, which is balanced by magnetic tension (if the field lines do not drift inwards), leading to bending of the magnetic field lines outwards. As described above, once the angle of the poloidal field to the rotation axis reaches 30 degrees, a wind is launched from the disc.

- *Transition zone*: Moving higher above the midplane, the radial and azimuthal field components continue to grow and magnetically compress the disc. Here also, the magnetic energy density becomes dominant over the thermal and gravitational energy densities as a result of the drop in gas density with z, leading to locally straight field lines.
- *Outflow region*: Moving still higher, the azimuthal velocity eventually becomes super-Keplerian, and the ions begin to drive the neutrals out in the radial and vertical directions. The magnetic field begins returning angular momentum to the gas, and when the flow reaches the sonic speed, the mass outflow rate becomes fixed.

Other mechanisms

As well as those listed above, there are a number of other mechanisms that could also operate in the disc to remove angular momentum and drive outflows. These mechanisms include the launching of hot 'plasmoids' from the protostar, similar to coronal mass ejections from the sun (Skinner et al. 2011), or 'magnetospheric ejections' arising from the expansion and subsequent reconnection of closed magnetic field lines connecting the star and disc (the 'reconnection X-wind', Hayashi et al. 1996; Goodson et al. 1999; Ferreira et al. 2000; Zanni & Ferreira 2013). However, in this chapter we only focus on the dominant theoretical mechanisms: APSWs, X-winds, and disc winds.

1.1.3. Constraining the launching mechanism

Each of the proposed launching mechanisms in Section 1.1.2 is expected to exhibit a range of values for the ejection/accretion ratio ($\dot{M}_{\rm out}/\dot{M}_{\rm in}$) and operate at a range of footprint radii r_0 within the disc, including substantial overlap. Stellar wind models have footprint radii on the central object, while for disc wind models they lie much further out, beyond the influence of the stellar magnetic field. X-wind footprints lie in-between, at the X point: the radius at which the magnetosphere of the protostar truncates the rotating disc. Similarly, each launching mechanism is consistent with a range of values for $\dot{M}_{\rm out}/\dot{M}_{\rm in}$. X-winds are characteristic of large $\dot{M}_{\rm out}/\dot{M}_{\rm in}$; values are in the range 0.1–1 (e.g. Najita & Shu 1994). APSW models can range from $\dot{M}_{\rm out}/\dot{M}_{\rm in} = 0.06$ up to a hard limit of 0.6 (Matt & Pudritz 2008), while disc winds can account for a much larger range: from $\dot{M}_{\rm out}/\dot{M}_{\rm in} = 10^{-5}$ (Wardle & Königl 1993), up to 0.3 (Pelletier & Pudritz 1992).

A recent study by Watson et al. (2016) measured outflow and accretion rates for a sample of 84 protostars of different Classes in mid- and far-infrared emission. From the sample, they found that ~50 per cent matched a range of $\dot{M}_{\rm out}/\dot{M}_{\rm in}$ indicative of an X-wind, while APSWs and disc winds could account for 56 and 74 per cent, respectively. However, 43 per cent of their sample could be explained by all three mechanisms. They also found an upper edge in the distribution of $\dot{M}_{\rm out}/\dot{M}_{\rm in}$ at 0.6, consistent with an APSW origin. They concluded that if there are only three mechanisms responsible for outflows (APSWs, X-winds, and disc winds), the observed distribution of $\dot{M}_{\rm out}/\dot{M}_{\rm in}$ suggests that disc winds dominate the ejection of angular momentum in objects with low $\dot{M}_{\rm out}/\dot{M}_{\rm in}$, while APSWs dominate near the cutoff at $\dot{M}_{\rm out}/\dot{M}_{\rm in} \simeq 0.6$.

Observational studies of optical forbidden emission from [O I] 6300 Å, [O I] 5577 Å, and [S II] 6731 Å have been able to separate protostellar outflows into a high-velocity component (HVC) and a low-velocity component (LVC) (e.g. Hartigan et al. 1995; Hirth et al. 1997; Rigliaco et al. 2013; Simon et al. 2016). Spatially resolved observations have shown that HVCs, with typical velocities of 30–200 km s^{-1}, are formed in extended collimated jets (e.g. Bacciotti et al. 2000; Lavalley-Fouquet et al. 2000; Woitas et al. 2002), most likely linked to MHD disc winds (e.g. Ferreira et al. 2006). The slower (~ 5 km s^{-1}) and denser LVC exists distinct from the HVC (e.g. Hartigan et al. 1995; Rigliaco et al. 2013; Natta et al. 2014), but is kinematically linked to both the HVC and accretion (Banzatti et al. 2019). Recently, several studies have shown that the LVC may often be separated into a broad component (BC) and a narrow component (NC) (Rigliaco et al. 2013; Simon et al. 2016). The launching radii of 0.05–0.5 au inferred for the BC excludes the possibility of a photoevaporative wind due to the strong gravity of the star and disc, instead pointing to an origin in MHD disc winds (Simon et al. 2016). The origin of the NC, with projected launch radii of 0.5–5 au, has been more hotly debated, but the recent study of Banzatti et al. (2019) finds that the kinematics of the BC and NC are correlated, suggesting that they are both part of the same radially extended wind, with most of the mass outflow rate in the BC (Simon et al. 2016; Fang et al. 2018; Banzatti et al. 2019).

Furthermore, more recent studies using ALMA have been able to obtain high-resolution maps of molecular outflows in the millimetre and sub-millimetre range (e.g. Bjerkeli et al. 2016; Hirota et al. 2017; Louvet et al. 2018), which have lead to a number of key findings. Rotating outflows have been confirmed in TMC-1A (Bjerkeli et al. 2016), Orion Source I (Hirota et al. 2017), HH212 (Tabone et al. 2017) and HH30 (Louvet et al. 2018), carrying significant angular momentum away from the underlying discs (e.g. Aso et al. 2015; Bjerkeli et al. 2016; Hirota et al. 2017; Zhang

et al. 2018). These outflows also map to a large range of launching radii on the disc (0.5–25 au, e.g. Bjerkeli et al. 2016; Hirota et al. 2017; Lee et al. 2018; Louvet et al. 2018; Zhang et al. 2018).

The above studies demonstrate increased support for the disc wind mechanism as the most likely candidate to account for the majority of the outflow. Combining this with the renewed theoretical emphasis on disc winds to account for the majority of angular momentum transport in the inner regions of protostellar discs (e.g. Turner et al. 2014; Gressel et al. 2015; Bai 2016, 2017), and the lack of observational evidence for MRI-driven turbulence in the outer disc (Flaherty et al. 2015, 2017, 2018), reinforces the importance of understanding and constraining the disc wind launching mechanism.

1.1.4. A short history of disc wind models

Magnetocentrifugal disc winds were first modelled in the context of active galactic nuclei (AGN) and black holes (Lovelace 1976; Blandford 1976; Blandford & Znajek 1977). The seminal paper of (Blandford & Payne 1982) was instrumental in quantifying the nature of these winds using a self-similar model, assuming a cold, axisymmetric wind from a thin disc. They showed that if the magnetic field is sufficiently strong, with magnetic energy of the order of the thermal energy, and sufficiently inclined to the rotation axis, then it is only necessary to expel a small fraction of the inflowing mass from the disc surface in order to transport away all of the excess angular momentum.

Disc wind models were subsequently applied to outflows from young stellar objects (YSOs) (e.g. Pudritz & Norman 1983), with the first numerical simulations of YSO disc winds performed by Uchida & Shibata (1985) and Shibata & Uchida (1985, 1986). Early disc wind models used a combination of Ohmic diffusivity and turbulent viscosity to prevent the build-up of magnetic flux at the centre of the system (Ferreira & Pelletier 1993a,b; Li 1995; Ferreira 1997), or strong ambipolar diffusion (Konigl 1989; Wardle & Königl 1993; Li 1996), which is applicable to regions farther out in the disc ($>$ 10 au). These early models showed that there were three basic requirements for steady wind launching:

1. At the base of the wind, the magnetic field must be strong enough for the poloidal component to act as a rigid wire. This is satisfied if the ratio of the thermal to magnetic pressure $\beta \lesssim 1$.

2. The poloidal field must be inclined to the rotation axis by at least 30 degrees.

3. The disc material is allowed to flow through the field lines via diffusion, in the form of either turbulent resistivity, or Ohmic or ambipolar diffusion.

Subsequent models focussed on including more detailed physics to probe the structure of these regions. Due to the complexity of the calculations, the problem was simplified by only modelling a localized region of the disc/wind system. This included modelling the wind, whilst treating the disc diffusivity and turbulence simply (e.g. Ouyed & Pudritz 1997a,b; Casse & Keppens 2002, 2004; Zanni et al. 2007; Sheikhnezami et al. 2012), or focussing on detailed models of localized regions within the disc (e.g. Wardle & Königl 1993; Suzuki & Inutsuka 2009; Königl et al. 2010; Salmeron et al. 2011; Fromang et al. 2013; Bai & Stone 2013a,b). Only in more recent years, with state-of-the-art simulation techniques and advanced computing power, have simulations been able to take a more global approach (Gressel et al. 2015; Béthune et al. 2017; Bai 2017).

Global simulations are very effective in their ability to investigate the kinematics and dynamics of outflows. They can incorporate thermochemical networks to explore the chemical evolution and grain processing of the disc and wind (e.g. Wang et al. 2019), follow the influence of turbulence from MHD and hydrodynamic instabilities on wind launching, and investigate flux transport and the formation of rings and gaps in the disc (e.g. Bai & Stone 2017; Suriano et al. 2019). However, local semi-analytical models are still important in their own right. They are generally numerically cheaper to run, allowing for large parameter studies, have less overall complexity, which aids in the disentangling of the complex relationships between competing forces in the disc and wind, while still including quite realistic physics. In recent years, semi-analytical models have been used in modelling the vertical structure of outflows (e.g. Chapters 2 and 3; Jacquemin-Ide et al. 2019), and investigating magnetic flux transport (e.g. Leung & Ogilvie 2019), hydrodynamical instabilities (Pfeil & Klahr 2019), and dust transport in outflows (Giacalone et al. 2019).

One of the more serious restrictions of local models is their limited domain range. In this thesis, we develop the first ever 1+1.5D model of wind-launching discs including all three non-ideal MHD effects (Ohm, Hall, and ambipolar), extending the vertical semi-analytical models of Wardle & Königl (1993), Königl et al. (2010), and Salmeron et al. (2011) into the radial dimension. Using this model we investigate the ejection/accretion ratio ($\dot{M}_{\rm out}/\dot{M}_{\rm in}$) and launch footprint of disc winds from discs with a range of parameters, in order to better differentiate between launching mechanisms in observations of jets and outflows (e.g. Ferreira et al. 2006; Banzatti et al. 2019).

1.2. Interstellar turbulence and the star formation rate

Protostellar jets efficiently remove angular momentum from their system of origin, initially transferring it from the rotating disc or star to the magnetic field via a number of mechanisms (Section 1.1.2). Once the flow reaches the base of the wind, this momentum is transferred back to the material and the wind is accelerated away (Königl & Salmeron 2011). At larger scales, the jet breaks through the remaining cloud envelope and injects this momentum back into its surrounding environment. Momentum is transferred through the entrainment of material at the jets' leading edge, or through turbulent mixing layers at the outer edge of the jet beam (Raga et al. 1993). The efficiency with which the angular momentum is transferred back to the clouds is inversely proportional to the jet-to-cloud density ratio (Masson & Chernin 1993). Overdense jets will 'punch' quickly through clouds without depositing much momentum into the swept-up gas. However, when the jet reaches a denser region in the cloud such as a molecular cloud core, the transfer efficiency increases. In this type of interaction the jet is initially deflected around the surface of the overdensity, but subsequently bores a hole into the core, transferring momentum to the core material as it goes (Raga & Murdin 2002). Momentum efficiency is also increased when the jet direction and base velocity are time varying. These effects break the jet into a series of independent projectiles, which slow down much more quickly than a steady, well-aligned jet with a continuous supply of reinforcing material behind it (Raga & Biro 1993).

Momentum transfer through jet feedback both perpetuates and limits star formation in molecular clouds (Elmegreen & Scalo 2004; Mac Low & Klessen 2004; McKee & Ostriker 2007). The injection of angular momentum via jets back into GMCs contributes to the driving and sustaining of supersonic turbulence. Without this feedback, hydrodynamic and MHD turbulence decays quickly (Stone et al. 1998; Mac Low 1999), preventing the generation of dense regions required for gravitational collapse. Conversely, supersonic turbulence contributes to the observed inefficiency of star formation in local molecular clouds through turbulent support against gravitational collapse (Krumholz et al. 2014). Observational estimates of star formation efficiency (defined as the ratio of the mass of the gas turned into stars and the total mass of the cloud) give typical values ranging between 0.01 and 0.1 (Frank et al. 2014). These estimates were recently connected to jet feedback in the study of Federrath (2015).

1.2.1. Star formation theory

Protostellar jets are just one of a number of different sources driving turbulence in molecular clouds. The list also includes supernova explosions, large-scale gravitational contraction, and galactic spiral density shocks to name a few (e.g. Elmegreen & Scalo 2004; Mac Low & Klessen 2004; Federrath & Klessen 2012). These energy sources drive supersonic turbulence, creating hierarchical density structures in the form of a log-normal distribution (Vázquez-Semadeni 1994). In log-space this distribution has the form

$$p(s)\mathrm{d}s = \frac{1}{\sqrt{2\pi\sigma_s^2}} \exp\left[-\frac{1}{2}\frac{(s-\bar{s})^2}{\sigma_s^2}\right]\mathrm{d}s, \tag{1.6}$$

where $s \equiv \ln(\rho/\bar{\rho})$, and $\bar{s}$ and σ_s^2 are the mean and variance of the logarithm of the density ρ, scaled by the mean density of the cloud $\bar{\rho}$, respectively. The parameters $\bar{s}$ and σ_s^2 are related by $\bar{s} = -\sigma_s^2/2$ as a result of mass conservation (Vázquez-Semadeni 1994; Federrath et al. 2008b), hence equation (1.6) can be described solely by the density variance σ_s^2. Fig. 1.3 displays the probability density function (PDF) described by equation (1.6) for supersonic, isothermal turbulence, characterized by different values of the standard deviation of the logarithm of the density σ_s. This turbulent PDF is vital to the formation of stars, as it includes a high-density tail which can result in the formation of self-gravitating cores and subsequent collapse into single and multiple star systems.

The star formation rate in any particular cloud, $\dot{M}_*$, is measured in units of $M_\odot\ \mathrm{yr}^{-1}$. Values for the SFR differ between individual clouds, therefore theoretical derivations often use the more general dimensionless measurement, the star formation rate per free-fall time, $\mathrm{SFR}_{\mathrm{ff}}$ (Krumholz & McKee 2005). This is defined as the fraction of cloud mass converted into stars per cloud mean free-fall time, $\bar{t}_{\mathrm{ff}} = \sqrt{3\pi/32G\bar{\rho}}$:

$$SFR_{\mathrm{ff}} = \frac{\dot{M}_*(t)}{M_{\mathrm{cl}}(t)}\bar{t}_{\mathrm{ff}}, \tag{1.7}$$

where M_{cl} is the mass of the cloud and all quantities are time dependent. Current theories derive the SFR as the mass fraction above an effective critical density for star formation, $\tilde{\rho}_{\mathrm{crit}}$. The general formula for the star formation rate was first proposed by Hennebelle & Chabrier (2011) and explored in more detail in Federrath & Klessen (2012):

$$SFR_{\mathrm{ff}} = \frac{\epsilon}{\phi_{\mathrm{t}}}\int_{\tilde{\rho}_{\mathrm{crit}}}^{\infty}\frac{\bar{t}_{\mathrm{ff}}}{t_{\mathrm{ff}}(\tilde{\rho})}p(\tilde{\rho})\mathrm{d}\tilde{\rho}, \tag{1.8}$$

where $p(\tilde{\rho})\mathrm{d}\tilde{\rho} = \tilde{\rho}p(s)\mathrm{d}s$, $p(s)\mathrm{d}s$ is given by equation (1.6), ϵ is an efficiency coefficient, and ϕ_{t} is the replenishment factor (see discussion below). Substituting in the formulae for $\bar{t}_{\mathrm{ff}}$, $t_{\mathrm{ff}}(\tilde{\rho})$, and

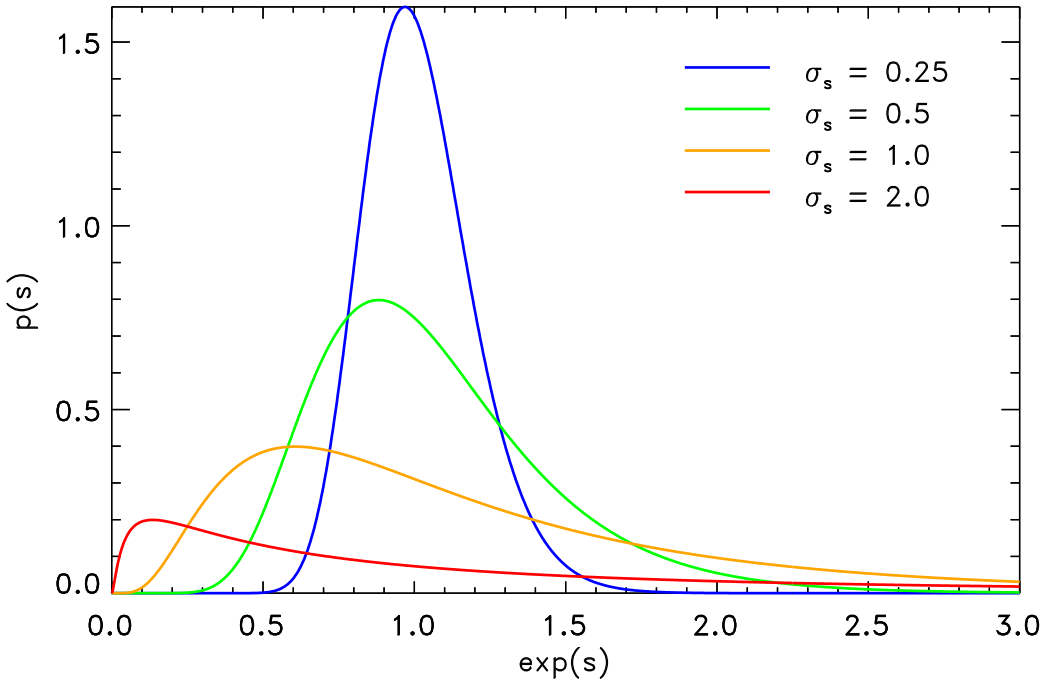

Figure 1.3 The log-normal density PDF of supersonic isothermal turbulence, assuming different values of the standard deviation of the logarithm of the density σ_s. The density PDF $p(s)$, described by equation (1.6), is plotted as a function of the normalized density $\exp(s) = \rho/\bar{\rho}$.

$p(s)$, the general solution for equation (1.8) is:

$$SFR_{\rm ff} = \frac{\epsilon}{2\phi_{\rm t}} \left(\frac{3}{8}\sigma_s^2\right) \left[1 + {\rm erf}\left(\frac{\sigma_s^2 - s_{\rm crit}}{\sqrt{2\sigma_s^2}}\right)\right], \tag{1.9}$$

which only depends on $s_{\rm crit} = \ln(\tilde{\rho}_{\rm crit})$ and σ_s^2 (Padoan et al. 2014).

The density PDF in equation (1.8) is divided by the free-fall time at each density $t_{\rm ff}(\tilde{\rho})$ ('multi-freefall' model), because the unstable gas with densities above $\tilde{\rho}_{\rm crit}$ is expected to collapse and turn into stars in a free-fall time. Previous estimates of the SFR used approximations to this value, such as $\bar{t}_{\rm ff}$ (Krumholz & McKee 2005) or $t_{\rm ff}(\tilde{\rho}_{\rm crit})$ (Padoan & Nordlund 2011), which allowed the free-fall factor to appear outside the integral ('single-freefall' model), simplifying the problem.

Assuming a steady-state, the shape of the density PDF will remain constant, however the extraction of material above $\tilde{\rho}_{\rm crit}$ to form stars depletes the high-density gas, hence the turbulent flow must replenish this region of the PDF. This may take longer than the free-fall time at any given density, hence the replenishment factor, $\phi_{\rm t} \geq 1$, is introduced in equation (1.8). Hennebelle & Chabrier (2011) approximated $\phi_{\rm t}$ by the turbulence cross-over time, giving $\phi_{\rm t} \sim 3$, while Krumholz & McKee (2005) used the global free-fall time. Padoan & Nordlund (2011) assumed

that the replenishment time was on the order of the free-fall time of the critical density $\tilde{\rho}_{\rm crit}$, and did not introduce the parameter $\phi_{\rm t}$ into the derivation of $\mathrm{SFR}_{\rm crit}$. Comparing theoretical models to numerical simulations, (Federrath & Klessen 2012) find that $\phi_{\rm t} \sim 2$–5 in the best-fit cases.

The coefficient ϵ in equation (1.8) accounts for two separate efficiencies in the star formation process, and hence satisfies $\epsilon \leq 1$. Firstly, it accounts for the mass of material above $\tilde{\rho}_{\rm crit}$ that can collapse gravitationally. Even though a parcel of material might be denser than $\tilde{\rho}_{\rm crit}$, it may be too small, or have too much turbulent energy to collapse. Secondly, ϵ accounts for the fraction of material that actually ends up in stars (the core-to-star efficiency). Observational, numerical and analytical constraints suggest a value of $\epsilon \simeq 0.3$–0.7 (Matzner & McKee 2000; Federrath & Klessen 2012, 2013; Federrath et al. 2014).

Differences between various SFR models are generally due to the choice of the critical density $\tilde{\rho}_{\rm crit}$, given that most models use equation (1.8) to calculate the SFR. Federrath & Klessen (2012) and Padoan et al. (2014) summarize a number of different analytical models for $\tilde{\rho}_{\rm crit}$, in particular those derived by Krumholz & McKee (2005), Padoan & Nordlund (2011), and Hennebelle & Chabrier (2011, 2013). The different formulations of $\tilde{\rho}_{\rm crit}$ is beyond the scope of this thesis, hence we direct the reader to the above references for more information.

1.2.2. The density variance–Mach number relation

In early simulations of isothermal, supersonic turbulence, Padoan et al. (1997) and Nordlund & Padoan (1999) discovered that the standard deviation of the density scales linearly with the rms Mach number, $\sigma_{\tilde{\rho}} = b\mathcal{M}$, where $\mathcal{M} = \sigma_v / c_{\rm s}$, given the standard deviation of the velocity field σ_v, and sound speed $c_{\rm s}$, with $b \approx 0.5$. Transforming this equation to log space, it becomes

$$\sigma_s^2 = \ln\left(1 + b^2\mathcal{M}^2\right). \tag{1.10}$$

Equation (1.10) is important for understanding supersonic turbulence, as it relates the properties of the density PDF (via σ_s^2), to the properties of the velocity field (via $\mathcal{M}$). The value of b depends on the type of driving of the turbulence, with $b = 1$ corresponding to purely compressive driving, while $b = 1/3$ corresponds to purely solenoidal driving (Federrath et al. 2008b, 2010)

Equation (1.10) has been tested numerically for a number of different cases, including polytropic gases (Passot & Vázquez-Semadeni 1998; Scalo et al. 1998; Nordlund & Padoan 1999; Federrath & Banerjee 2015), using heating and cooling curves (e.g. Wada & Norman 2001; Kritsuk & Norman 2002; Audit & Hennebelle 2005; Hennebelle & Audit 2007; Audit & Hennebelle 2010; Seifried

et al. 2011; Gazol & Kim 2013) or a detailed chemical network (Glover et al. 2010; Micic et al. 2012), and including the effects of magnetic fields (e.g. Ostriker et al. 2001; Lemaster & Stone 2008; Padoan & Nordlund 2011; Molina et al. 2012) and gravity (e.g. Klessen 2000; Federrath et al. 2008a; Collins et al. 2011; Kritsuk et al. 2011a; Cho & Kim 2011; Collins et al. 2012; Federrath & Klessen 2013; Kainulainen et al. 2013). There have also been a number of studies performed to derive more precise values of b (e.g. Ostriker et al. 1999; Klessen 2000; Glover & Mac Low 2007; Kritsuk et al. 2007; Federrath et al. 2008b; Schmidt et al. 2009; Federrath et al. 2010; Price et al. 2011; Konstandin et al. 2012; Federrath 2013a).

In the case of magnetized turbulence, equation (1.10) is modified to

$$\sigma_s^2 = \ln\left(1 + b^2\mathcal{M}^2\frac{\beta}{\beta+1}\right) \tag{1.11}$$

(Padoan & Nordlund 2011; Molina et al. 2012), where β is the ratio of gas to magnetic pressure,

$$\beta = \frac{2c_s^2}{v_A^2} = \frac{2\mathcal{M}_A^2}{\mathcal{M}^2}, \tag{1.12}$$

$v_A = B/\sqrt{4\pi\rho}$ is the Alfvén speed, and $\mathcal{M}_A$ is the Alfvén Mach number. However, this equation only takes into account the magnetic pressure, but not the magnetic tension; it neglects the anisotropy of MHD turbulence which tends to align the magnetic and velocity fields, resulting in a breakdown of the relation in MHD turbulence with strong magnetic fields, and in trans- or sub-Alfvénic turbulence (Padoan et al. 2014). Equation (1.11) simplifies to the hydrodynamic case (equation 1.10) for $\beta \to \infty$.

While the relation between the density variance and Mach number in isothermal turbulence has been studied extensively, to date no investigation has been performed into the behaviour of adiabatic turbulence, important for modelling the inner regions of GMCs where strong shielding allows molecular gas to form (Mac Low & Klessen 2004). In isothermal gas, the internal energy reservoir is essentially infinite, hence adding energy through turbulent driving has no effect on the gas temperature. In the adiabatic regime, as opposed to the isothermal case, the gas has a finite number of degrees of freedom, resulting in an increase in gas temperature as energy is injected. As a result, equation (1.10) is expected to take on a different form in response to an adiabatic exponent greater than unity ($\gamma > 1$). In this thesis, we develop the first ever hydrodynamical simulations of driven turbulence in the adiabatic regime, to investigate the dependence of the density variance–Mach number relation on the adiabatic exponent of the turbulent gas. We vary the adiabatic exponent γ, testing diatomic molecular ($\gamma = 7/5$) and

monatomic ($\gamma = 5/3$) gases, while also varying the driving amplitude to examine the robustness of these relations for a wide range of Mach numbers.

1.3. Thesis outline

Our investigation into the origins and impacts of protostellar jets is organized as follows.

In Chapter 2, we present the first ever 1+1.5D model of protostellar disc winds including all three non-ideal MHD terms (Ohm, Hall, and ambipolar). The design of this model allows us to gain significant insight into the radial and vertical structure of the wind-launching region. We specifically investigate the radial location and efficiency of disc winds, as these two diagnostics are important for understanding the origins of large scale jets. We find that the majority of wind mass loss is centred within a radially localized region in the planet-forming region of protostellar discs ($\sim$ 0.5–2 au). We find that both the footprint radius and wind efficiency are significantly influenced by the mass accretion rate, magnetic field strength, and surface density profile of the disc.

In Chapter 3, we update the calculation of the diffusivities in the 1+1.5D model from vertically scaled to self-consistent, based off the local ionization rate. We find that the wind remains localized, however the self-consistent formulation results in increased field-matter coupling above and below the disc midplane. This increases the magnetic field bending and compresses the disc, resulting in a shift of the wind-launching region to smaller radii, and an order of magnitude drop in the wind efficiency. We also find that the radial profile of wind mass loss is modified into a radially symmetric configuration resembling a Gaussian profile.

We change topics in Chapter 4, moving outwards from the source of jets and outflows to look at their effects on the statistics of large-scale turbulence. We investigate the relationship between the density and velocity fields in non-isothermal adiabatic turbulence, finding that adiabatic turbulence behaves in a very different way to the well studied isothermal case. Due to limited internal energy modes and the subsequent continual heating of the gas via turbulent driving, the gas evolves steadily along a defined relation in density variance–Mach number space, independent of the amplitude of the driving. This relation is steeper than its isothermal equivalent, and using large-scale numerical simulations of driven adiabatic turbulence, we calculate an empirical relation between the density variance and Mach number for low Mach numbers ($b\mathcal{M} \lesssim 1$), as a function of the adiabatic index, γ. We derive a similar relation at high Mach numbers ($b\mathcal{M} > 1$)

using the Rankine-Hugoniot shock-jump conditions (Rankine 1870; Hugoniot 1887).

We summarize our results in Chapter 5. We also discuss the implications of our work in the field of protostellar outflows. We conclude by briefly proposing some interesting lines of investigation for future work, in order to expand our work and further advance the field.

CHAPTER 2

Centrifugally driven winds from protostellar accretion discs - I. Formulation and initial results

This chapter has been published as ***Nolan, C. A., Salmeron, R., Federrath, C., Bicknell, G. V., & Sutherland, R. S. 2017, MNRAS, 471, 1488****, referenced as Nolan et al. (2017). This chapter is not modified from the published version, except in the following respects:*

- *Section, figure, footnote, and table numbering, and general formatting, have been modified for consistency with the remainder of the thesis;*
- *References to future work actually completed in Nolan et al. (2019) has been changed to point to Chapter 3 of this thesis;*
- *Appendices A, B, and C to this paper have been moved to Appendices A, B, and C of this thesis.*

The original paper is available at `https://academic.oup.com/mnras/article/471/2/1488/3906601`.

The 1.5D vertical disc-wind model used in this chapter was provided in its original form by Dr Raquel Salmeron. This model was adapted into a 1+1.5D configuration by the candidate, including extensive additions to the structure and complexity of the 1.5D model itself. All subsequent simulations employing the 1.5D and 1+1.5D models were performed by the candidate.

Abstract

Protostellar discs play an important role in star formation, acting as the primary mass reservoir for accretion onto young stars and regulating the extent to which angular momentum and gas is released back into stellar nurseries through the launching of powerful disc winds. In this study, we explore how disc structure relates to the properties of the wind-launching region, mapping out the regions of protostellar discs where wind launching could be viable. We combine a series of 1.5D semi-analytic, steady-state, vertical disc-wind solutions into a radially extended 1+1.5D model, incorporating all three diffusion mechanisms (Ohm, Hall, and ambipolar). We observe that the majority of mass outflow via disc winds occurs over a radial width of a fraction of an astronomical unit, with outflow rates attenuating rapidly on either side. We also find that the mass accretion rate, magnetic field strength, and surface density profile each have significant effects on both the location of the wind-launching region and the ejection/accretion ratio $\dot{M}_{\rm out}/\dot{M}_{\rm in}$. Increasing either the accretion rate or the magnetic field strength corresponds to a shift of the wind-launching region to smaller radii and a decrease in $\dot{M}_{\rm out}/\dot{M}_{\rm in}$, while increasing the surface density corresponds to launching regions at larger radii with increased $\dot{M}_{\rm out}/\dot{M}_{\rm in}$. Finally, we discover a class of disc winds containing an ineffective launching configuration at intermediate radii, leading to two radially separated regions of wind launching and diminished $\dot{M}_{\rm out}/\dot{M}_{\rm in}$. We find that the wind locations and ejection/accretion ratio are consistent with current observational and theoretical estimates.

2.1. Introduction

Protostellar discs are an integral part of the star and planet formation processes (Li et al. 2014). They are formed via angular momentum conservation as a pre-stellar core collapses, and become the primary source of material for the young, central protostar as it builds up to its final mass. For material to accrete through the disc and onto the growing star, angular momentum, since conserved, must be redistributed within the disc or ejected from the system (Turner et al. 2014). This process may be facilitated by bipolar outflows and winds, which are also important for star formation, including the initial mass function and star formation rate (Federrath et al. 2014; Frank et al. 2014; Krumholz et al. 2014; Li et al. 2014; Offner et al. 2014; Padoan et al. 2014; Federrath 2015).

Observations show that the occurrence of accretion and outflow are correlated (e.g. Bally et al. 2007), and this correlation is marked by accretion diagnostics and outflow signatures. The rates of accretion and outflow in these systems are also correlated, with bipolar jets expelling between 0.1–0.2 times the amount of material accreted onto the star (Cabrit 2007; Ellerbroek et al. 2013; Watson et al. 2016). Any theory of wind-launching must reproduce these correlations in order to be viable.

Mass transport through protostellar discs onto their host stars is likely to take place via a combination of different accretion mechanisms operating within different regions of the disc. Two main accretion mechanisms stand out: magnetohydrodynamic (MHD) turbulence induced by the magnetorotational instability (MRI, Balbus & Hawley 1991; Balbus & Hawley 1998; Bai & Stone 2014), and centrifugally driven winds (CDWs) (Blandford & Payne 1982, hereafter BP82). In recent years, through developments in modelling of turbulent diffusive discs, there has been serious doubts raised as to the effectiveness of MRI turbulence in the range of 1–10 astronomical units (au) (see the recent review of Turner et al. 2014). The MRI is sensitive to the dominant magnetic diffusion mechanism in the disc and within this range Hall diffusion is expected to be the strongest at the disc midplane (Wardle & Salmeron 2012). Kunz & Lesur (2013) found that if the Hall term is large enough, the MRI turbulence transforms into self-sustaining zonal structures with poor angular momentum transport. Similarly, Wardle & Salmeron (2012) discovered that if the magnetic field is anti-parallel to the rotation axis and small dust grains are present, the vertical column available to the MRI is insignificant. This has led to a renewed focus on disc winds as the dominant angular momentum removal mechanism in this region.

Since the pioneering work of BP82 – which focussed on radio jets launched from active galactic nuclei – and its re-application to protostellar jets by Pudritz & Norman (1983) and Pudritz & Norman (1986), there have been many advances in our understanding of disc winds and the methods used to model them. Early work established the connection between disc properties, mass loading of winds and angular momentum transport by including the disc as a specific region within a 2D simulation domain (e.g. Shibata & Uchida 1985, 1986), or as a fixed boundary condition (e.g. Ustyugova et al. 1995; Ouyed et al. 1997). Subsequent studies involved self-similar solutions (Li 1995, 1996; Ferreira 1997), which emphasized the importance of the magnetic field in driving the wind, and in some cases were able to predict the large-scale behaviour of the flow (Teitler 2011). More recently, shearing-box simulations have been employed to investigate the properties of winds using realistic microphysics (Suzuki & Inutsuka 2009; Suzuki et al. 2010;

Fromang et al. 2013; Bai & Stone 2013a,b; Lesur et al. 2013; Simon et al. 2013; Bai 2014). These simulations reinforce the role disc winds play in mass transport in protostellar discs and accretion onto the protostar.

Local simulations such as the ones listed above are important for understanding the dynamical behaviour in particular parts of the disc, but are limited in scope. The challenge for global disc models is to accurately represent non-ideal effects while modelling large portions of the disc. This task was first attempted by Dzyurkevich et al. (2010) in the context of the MRI, using a fixed Ohmic resistivity distribution, and more recently Gressel et al. (2015) added ambipolar diffusion and time-dependent gas-phase electron and ion fractions.

In this paper, we develop a new approach for investigating protostellar disc winds, which allows for the resolving of steady-state axisymmetric wind solutions in the non-ideal MHD regime. We achieve this by linking together a set of radially localized, vertical 1.5D solutions of the type designed by Wardle & Königl (1993, hereafter WK93), Königl et al. (2010, hereafter KSW10) and Salmeron et al. (2011, hereafter SKW11), to create a radially extended, 1+1.5D model of the wind-launching region in axisymmetric cylindrical coordinates (r, z). We employ these models to investigate how the structure of the underlying disc affects the properties of the wind. We find that the location of the wind-launching region and the ejection/accretion ratio $\dot{M}_{\rm out}/\dot{M}_{\rm in}$ are significantly influenced by the mass accretion rate, magnetic field strength, and surface density profile, while still satisfying observational and theoretical constraints. Most importantly, we find that the wind-launching region is radially localized, with the outflow rate decreasing rapidly at larger and smaller radii, and we discover a class of disc winds containing an ineffective launching configuration at intermediate radii.

We begin by summarizing the numerical method in Section 2.2, before providing a comprehensive description of the 1.5D and 1+1.5D models in Sections 2.3 and 2.4, respectively. In Section 2.5, we present a detailed analysis of two distinct wind models, followed by a more general parameter study in Section 2.6. We discuss the implications of our results in Section 2.7 and summarize our conclusions in Section 2.8.

2.2. Method summary

In the following sections, we describe our method for modelling the wind-launching region of protostellar discs. We provide here a brief summary of the basic method before moving on to

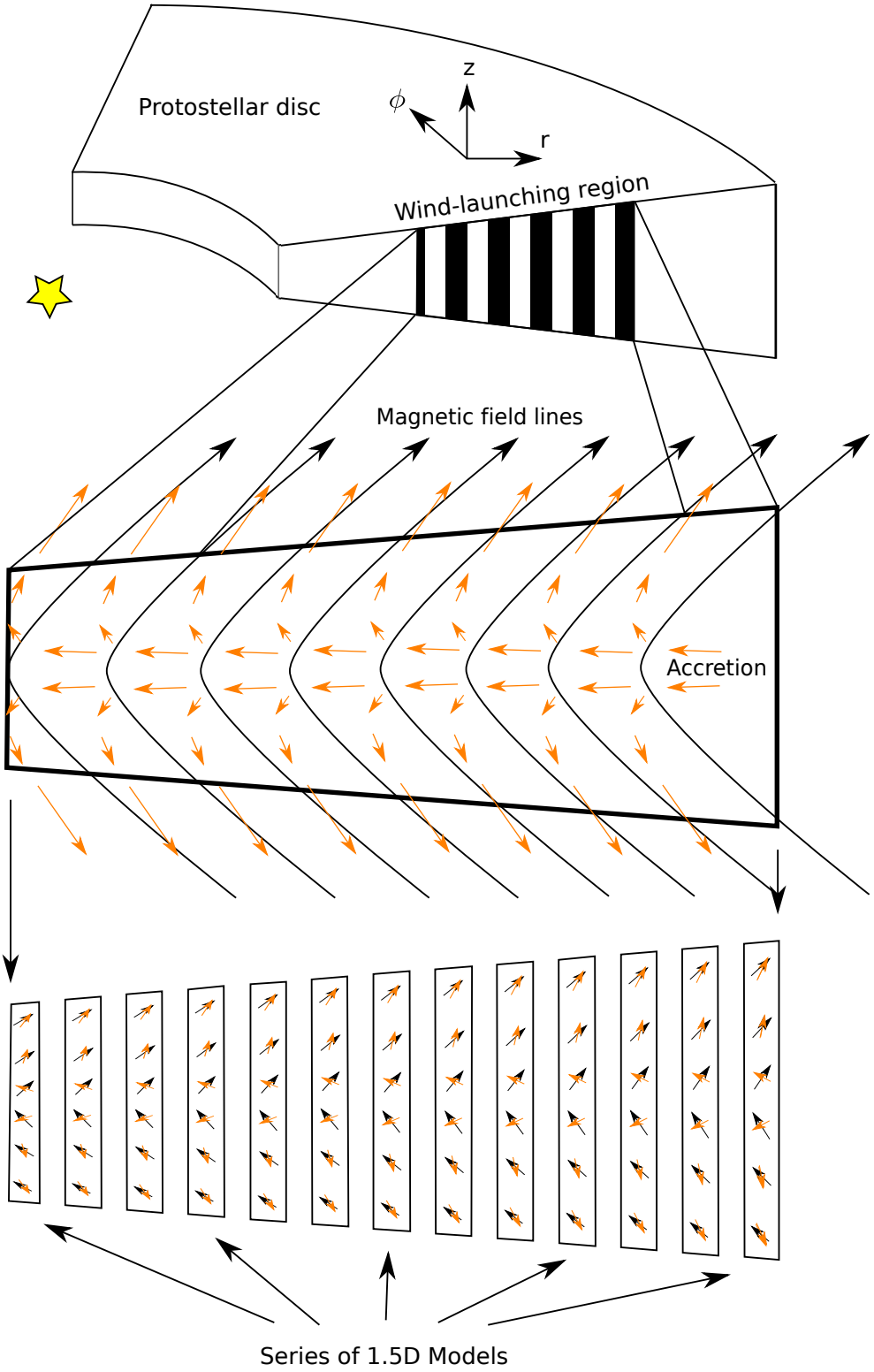

Figure 2.1 Schematic diagram showing the construction of the 1+1.5D models. Each model consists of a series of vertical, 1.5D radially-localized solutions positioned at consecutive radii, from the inner radius of the wind-launching region $r_{\rm in}$ to its outer radius $r_{\rm out}$. All 1.5D solutions provide disc/wind properties from the disc midplane up to the sonic point $z_{\rm s}$, including radial, azimuthal, and vertical vector components.

the full derivations in Sections 2.3 and 2.4.

To model the wind region, we link together a number of vertical, axisymmetric, 1.5D radially-localized solutions in radius, in such a way as to form a self-consistent 1+1.5D model in (r,z)-coordinates (see Fig. 2.1). Each 1.5D model is the integrated solution to a set of six ordinary differential equations (ODEs) in the vertical coordinate z, from the disc midplane up to the sonic point z_s[1] (see Section 2.3.2), and provides normalized values for the density ρ, velocity $\mathbf{v}$, magnetic and electric fields ($\mathbf{B}$ and $\mathbf{E}$ respectively), and current density $\mathbf{J}$ within this vertical range.

Each 1.5D solution is uniquely characterized by a number of dimensionless parameters listed in Section 2.3.1. By specifying conditions at the disc midplane (e.g. ρ_0, B_0, and the temperature T_0) at a particular radius, and calculating the diffusion coefficients η using our ionization model (see Appendix C) we can calculate these input parameters and solve for the vertical structure of the disc and wind. However, instead of specifying all of the conditions at the disc midplane directly, we obtain them by prescribing the values of the surface density (Σ), the local mass accretion rate ($\dot{M}_{\rm acc}$), the midplane ratio of the Alfvén speed to the isothermal sound speed (a_0), and the vertically isothermal temperature (T_0) at that radius, in addition to the stellar mass ($M_\star$), and iterate on the midplane density (ρ_0) and radial velocity ($v_{\rm r0}$) until the vertically integrated Σ and $\dot{M}_{\rm acc}$ of the solution matches the prescribed Σ and $\dot{M}_{\rm acc}$. Hence, by assigning values for Σ, $\dot{M}_{\rm acc}$, a_0, and T_0 at a particular radius within the disc, orbiting around a protostar of mass $M_\star$, we can calculate the vertical structure of the disc and wind at that point.

In order to create a 1+1.5D model, we assign the disc parameters Σ, $\dot{M}_{\rm acc}$, a_0, and T_0 at each radius, which allows us to calculate the vertical structure of the disc across a range of radii. However, these parameters must be chosen so that the 1+1.5D model does not violate the equations of non-ideal MHD, in the limit of a disc that is in a steady state and is geometrically thin, vertically isothermal, nearly Keplerian, and in dynamical equilibrium in the gravitational potential of the central protostar (KSW10). To do this, we tie each pair of radially adjacent solutions together using mass conservation, and check to make sure that the thin disc approximation is not violated. We also ensure that the $\nabla \cdot \mathbf{B} = 0$ condition is satisfied (see Section 2.4.3 for more details).

Finally, the inner and outer edges of our 1+1.5D model are defined by four constraints (listed in

[1]Ideal MHD flows have three critical surfaces, beginning with the slow magnetosonic point. However, when the flow is diffusive, the thermal sonic point becomes the first critical point of the flow (see Königl & Salmeron 2011, pp. 326)

Section 2.3.3), which set the region of parameter space in which the 1.5D solutions are physically viable (WK93, KSW10). Hence we arrive at a self-consistent 1+1.5D model, which maps out the structure of the wind-launching region of a protostellar disc from the midplane up to the sonic point. We note here that these models are still localized in that they do not take into account the global magnetic field structure (being limited in height by the thin disc approximation) and are also simplified by the use of parametrized conductivity profiles.

2.3. 1.5D radially-localized disc wind models

The 1.5D models of KSW10 form the basis of our 1+1.5D approach to disc winds. Hence, before describing our 1+1.5D models in Section 2.4, we pause here to summarize the properties and derivation of the 1.5D solutions.

Each 1.5D solution assumes that the disc is in a steady state, geometrically thin, vertically isothermal, nearly Keplerian, and is in dynamic equilibrium within the gravitational potential of the central protostar. Within the disc, the degree of ionization is low due to radiation shielding, causing non-ideal effects to become important. We incorporate finite conductivity effects via a conductivity tensor formulation (e.g. Wardle 1999), allowing the three basic field-matter diffusion mechanisms (Ohm, Hall, and ambipolar) to be included without the need for separate equations for each fluid component (KSW10). For reference, the Ohm, Hall, and ambipolar diffusion coefficients in the limit of a weakly-ionized ion-electron plasma are

$$\eta_{\rm O} = \frac{c^2 m_{\rm e} \gamma_{\rm e} \rho}{4\pi e^2 n_{\rm e}}, \tag{2.1}$$

$$\eta_{\rm H} = \frac{cB}{4\pi e n_{\rm e}}, \tag{2.2}$$

and

$$\eta_{\rm A} = \frac{B^2}{4\pi m_{\rm i} \gamma_{\rm i} \rho n_{\rm i}} \tag{2.3}$$

respectively (e.g. Wardle & Salmeron 2012), where c is the speed of light, e is the charge of an electron, and for the electron and ion subscripts 'e' and 'i' respectively, we have the particle mass $m_{\rm e,i}$, the number density $n_{\rm e,i}$, and $\gamma_{\rm e,i} = \langle \sigma v \rangle_{\rm e,i}/(m_{\rm e,i} + m)$, where $\langle \sigma v \rangle_{\rm e,i}$ is the rate coefficient for collisional momentum transfer between the charged species and the neutrals.

In the remainder of this section we define the model parameters that characterize each radially-localized solution, summarize the method of solving for the vertical structure of the disc using

these parameters as boundary conditions, and define the requirements for these solutions to be physically viable, before progressing on to the development of the 1+1.5D framework in Section 2.4.

2.3.1. Parameters

Each 1.5D radially-localized disc-wind solution is described by six dimensionless parameters, which determine the boundary conditions of the 1.5D problem (see Section 2.3.2). They are:

(i) The ratio of the Alfvén speed ($v_{\rm A0}$) to the isothermal sound speed ($c_{\rm s}$) at the disc midplane

$$a_0 \equiv \frac{v_{\rm A0}}{c_{\rm s}} = \frac{B_0}{\sqrt{4\pi\rho_0}}\frac{1}{c_{\rm s}}. \tag{2.4}$$

This parameter quantifies the strength of the ordered magnetic field that threads the disc.

(ii) The ratio of the gravitational tidal scale height $h_{\rm T}$ to the disc radius

$$\frac{h_{\rm T}}{r} = \frac{c_{\rm s}}{v_{\rm K}}, \tag{2.5}$$

where $v_{\rm K}$ is the Keplerian velocity. This parameter provides a measure of the geometric thickness of the disc and also constrains physically viable solutions (see equation 2.16). It was used by SKW11 to match solutions to BP82-type winds.

(iii) The midplane ratios of the magnetic diffusivity components[2],

$$\left[\frac{\eta_{\rm H}}{\eta_{\rm O}}\right]_0 \qquad \text{and} \qquad \left[\frac{\eta_{\rm A}}{\eta_{\rm O}}\right]_0. \tag{2.6}$$

In general, the diffusivity components and their ratios vary with height above the disc midplane, reflecting the change in disc conditions with height. However we adopt the simplification of KSW10 in which the ratios described by equation (2.6) are constant with height, z. Specifically, we scale the components of the conductivity tensor with the density and the magnetic field strength as ρ/B^2, so that the field-matter coupling (see below) is constant with height. This simplification will be relaxed in a subsequent paper.

[2]Previously, KSW10 used the midplane conductivity ratios $[\sigma_{\rm P}/\sigma_\perp]_0$ and $[\sigma_\perp/\sigma_{\rm O}]_0$ to characterize solutions (where $\sigma_\perp = \sqrt{\sigma_{\rm H}^2 + \sigma_{\rm P}^2}$ and the subscripts O, H, and P denote the Ohm, Hall, and Pedersen conductivities respectively), however in this paper we adopt the diffusivity ratios as they are more intuitively connected to the three diffusivity regimes.

(iv) The midplane Elsasser number

$$\Lambda_0 = \left(\tilde{\eta}_H^2 + (\tilde{\eta}_A + \tilde{\eta}_O)^2\right)^{-1/2}, \tag{2.7}$$

where

$$\tilde{\eta} = \frac{\eta}{v_{A0}^2/\Omega_K}, \tag{2.8}$$

and Ω_K is the Keplerian angular velocity. The Elsasser number measures the degree of coupling between the magnetic field and the neutrals, with the regimes of weak and strong coupling prescribed by $\Lambda_0 \ll 1$ and $\Lambda_0 \gg 1$ respectively. For future reference, the Elsasser numbers describing each diffusivity regime are defined as follows:

$$\Lambda_O = \frac{1}{\tilde{\eta}_O}, \qquad \Lambda_H = \frac{1}{\tilde{\eta}_H}, \qquad \Lambda_A = \frac{1}{\tilde{\eta}_A}. \tag{2.9}$$

(v) The inward radial Mach number at the midplane

$$\epsilon \equiv \frac{-v_{r0}}{c_s}, \tag{2.10}$$

which is a free parameter of the disc solution. We determine its value for the 1+1.5D model by constraining the local accretion rate $\dot{M}_{acc}$ at each radius (see Section 2.4.2).

(vi) The normalized azimuthal component of the electric field **E**

$$\epsilon_B \equiv \frac{-cE_{\phi 0}}{c_s B_z}, \tag{2.11}$$

which measures the radial drift of the poloidal magnetic field lines. WK93, using a similar radially localized model, derived solutions for positive and negative values of ϵ_B and found that configurations with the same value of $(\epsilon - \epsilon_B)$ were similar. This suggests that setting $\epsilon_B = 0$ should not significantly impact the generality of the results (see Section 2.7 and Appendix A of KSW10). We adopt $\epsilon_B = 0$ for the remainder of the paper.

2.3.2. Numerical integration of the localized disc equations

The dimensionless parameters listed in Section 2.3.1 are used to derive the boundary conditions for solving a set of six ODEs in the normalized vertical coordinate $\tilde{z} = z/h_T$, where the disc scale height h_T is defined by equation (2.5). These ODEs are derived from the equations of non-ideal MHD using the thin disc approximation, and determine the vertical structure of ρ, v_r, v_ϕ, B_r, B_ϕ, and E_r in dimensionless form. What follows is a brief summary of the method of

vertical integration for these equations; we refer the reader to SKW11 for a more comprehensive description.

To solve for the vertical structure of the disc, we begin by assigning the midplane values of ρ, $v_{\rm r}$, v_ϕ, $B_{\rm r}$, B_ϕ, and $E_{\rm r}$ in terms of the dimensionless parameters listed in Section 2.3.1 (see equations 18 and 20 – 22 of SKW11). We then guess the midplane value of $\tilde{v}_{\rm z0} = v_{\rm z0}/c_{\rm s}$ and the position of the sonic point $\tilde{z}_{\rm s}$, and integrate from the midplane towards $\tilde{z}_{\rm s}$. If the guessed value for $\tilde{v}_{\rm z0}$ is too high then $\tilde{v}_{\rm z}$ diverges, and if it is too low, $\tilde{v}_{\rm z}$ peaks and begins to decrease with $\tilde{z}$, which is unphysical. This gives upper and lower limits for the value of $\tilde{v}_{\rm z0}$. We then use an iterative bisection method to improve upon $\tilde{v}_{\rm z0}$ until we are close enough to the physical solution ($\tilde{v}_{\rm zs} = 1$) to estimate the position of $\tilde{z}_{\rm s}$ and the values of the variables there. We then simultaneously integrate from $\tilde{z} = \tilde{z}_{\rm s}$ and the midplane ($\tilde{z} = 0$) to an intermediate fitting point (usually ~ 0.7–0.9 $\tilde{z}_{\rm s}$), and adjust the guessed variables at each end iteratively until the solution converges.

2.3.3. Constraints for physically viable solutions

As previously shown by WK93 and KSW10, viable wind-driving disc solutions for which Λ_0 is not $\ll 1$ (where $\Lambda_0 \ll 1$ is indicative of very weak field-matter coupling) exist within a limited region of parameter space. This region is determined by the following four requirements:

(i) *Sub-Keplerian flow*: The flow remains sub-Keplerian ($v_\phi < v_{\rm K}$) within the disc. Super-Keplerian flow below the disc surface would require that the excess rotation be balanced by inwardly directed radial forces from the magnetic field. However, no mechanism provides super-Keplerian support of the flow in this region. The ions still lag behind the neutrals, providing an azimuthal drag which decelerates the neutrals (WK93). For the flow to remain sub-Keplerian within the disc, the configuration must satisfy

$$\frac{{\rm d}B_{\rm r}}{{\rm d}B_\phi} = -\frac{J_\phi}{J_{\rm r}} \approx -\frac{\left(\tilde{\eta}_{\rm H}+2\right)B_{\rm z}^2 + \tilde{\eta}_{\rm A}B_{\rm r}B_\phi}{\tilde{\eta}_{\rm O}B_{\rm z}^2 + \tilde{\eta}_{\rm A}\left(B_{\rm r}^2+B_{\rm z}^2\right)} < 0 \tag{2.12}$$

below the disc surface (see Section 4.1 of KSW10).

(ii) *Wind launching*: A wind is driven from the disc surface (i.e. a wind launching criterion is satisfied). As shown by BP82 in the ideal-MHD limit, a minimum inclination angle is required between the surface magnetic field (denoted by the subscript b) and the rotation axis to launch a wind. In Section 4.2 of KSW10, this constraint was generalized for non-ideal

MHD to the following:

$$\left[3+\frac{3}{2}\tilde{\eta}_{\rm H}-\tilde{\eta}_{\rm A}\tilde{\eta}_{\rm P}\right]B_{\rm rb}^2 \;>\; \left[1+\frac{5}{2}\tilde{\eta}_{\rm H}+\tilde{\eta}_{\rm T}^2\right]B_{\rm zb}^2 + \tilde{\eta}_{\rm A}\tilde{\eta}_{\rm P}B_{\phi\rm b}^2+\frac{3}{2}\tilde{\eta}_{\rm O}B_{\rm rb}B_{\phi\rm b}, \tag{2.13}$$

below the disc surface, where $\tilde{\eta}_{\rm T}^2 \equiv \tilde{\eta}_{\rm O}^2+\tilde{\eta}_{\rm H}^2+\tilde{\eta}_{\rm A}^2$ and $\tilde{\eta}_{\rm P}\equiv\tilde{\eta}_{\rm O}+\tilde{\eta}_{\rm A}$. This is used as a necessary condition for wind launching in our models. If this constraint is not satisfied, then there is either insufficient field-matter coupling to bend the magnetic field lines past the critical angle required for wind-launching, or the magnetic field is too strong to be bent. In the ideal-MHD limit, equation (2.13) reduces to the BP82 wind-launching criterion $B_{\rm rb}/B_{\rm zb} > 1/\sqrt{3}$.

(iii) *Mass loading*: Only the upper layers of the disc participate in the outflow. According to both theoretical and observational arguments (e.g. Königl & Pudritz 2000), only a small fraction of the disc material should participate in the outflow. If the wind torque is too strong, the disc wind is inherently unstable (Cao & Spruit 2002). The mass loading condition is implemented in KSW10 by requiring that the base of the wind $z_{\rm b}$ (which we identify as the height above which $v_\phi > v_{\rm K}$) be located above the magnetically reduced density scale height $z_{\rm h}$, defined as the height at which the density drops to $\rho_0/\sqrt{e}$,

$$z_{\rm b} > z_{\rm h}. \tag{2.14}$$

WK93 showed that if equation (2.14) is not satisfied, the gradient of B_ϕ changes sign within the disc. They explained this behaviour by noting that, as the midplane inflow Mach number ϵ decreases, the normalized height of the sonic point $\tilde{z}_s$ decreases, and the scale height increases. Eventually, $\tilde{\rho}_{\rm s} = \rho_{\rm s}/\rho_0$ becomes so large that the upwards mass flux transports more angular momentum than that brought in by the accretion flow. As a result, the gradient of B_ϕ changes sign as the magnetic field begins transferring angular momentum back into the flow before the top of the disc is reached. Such a configuration is unphysical, and likely unstable. Since the gradient of B_ϕ changes sign to a small degree below the sonic point in all of our 1.5D solutions, we have devised a new constraint based on the magnitude of this change.

In practice we expect that magnetic energy dominates up to the Alfvén surface, occuring at heights of order the footpoint radius, for $r_{\rm A}/r_0 \sim 3$ and typical inclinations of the magnetic field. This is also the scale at which collimation takes place. Hence, we define a new

constraint for the mass loading by requiring that the extrapolated value of B_ϕ at $z = r$ be less than zero, i.e.

$$B_\phi(z = r) < 0. \tag{2.15}$$

Due to the high sensitivity of the radial splitting and ejection/accretion ratio of the wind-launching region to this constraint, we treat all consequential results with caution, noting that our current models are not able to follow B_ϕ beyond z_s. Thus, the mass loading constraint is only an approximate constraint that results from extrapolating the solution to $z > z_s$ and therefore, the radial location where it is violated is approximate.

(iv) *Energy conservation*: The rate of heating by Joule dissipation at the midplane is bounded by the rate of gravitational potential energy released at that location (Königl 1997),

$$(\mathbf{J} \cdot \mathbf{E}')_0 < \frac{\epsilon v_K}{2a_0^2} \frac{B_0^2}{4\pi h_T}. \tag{2.16}$$

Diffusion-regime specific simplifications of each of these constraints may be found in WK93 (Ambipolar regime) and KSW10 (Hall and Ohm regimes). Here we use the generalized form which applies to all three regimes.

2.4. 1+1.5D disc wind models

Having established the basis for the 1.5D solutions, we now discuss the 1+1.5D framework in detail. We begin by describing the parameters which define the structure of the disc, and then outline the method used to find each 1.5D solution that matches this structure, in order to build the 1+1.5D wind-launching model. Finally, we provide an overview of the requirements for such a model, in the interest of self-consistency and physical viability.

2.4.1. 1+1.5D parameters

To build a 1+1.5D model, a framework must be constructed which connects the 1.5D solutions together in a physically consistent way. In our model, this framework is constructed from four disc parameters. The first three are defined as analytic functions of radius, while the fourth depends primarily on a single value at the innermost radius, and is calculated for all other radii using mass conservation. We now describe each parameter in detail.

Magnetic field strength: The ratio of the Alfvén speed to the isothermal sound speed at the disc midplane a_0 ($\equiv v_{A0}/c_s$) is a measure of the magnetic field strength. We assume that a_0 is constant for the entire wind-launching region of the disc, and consider values of $a_0 \sim 1$ in this study. This parameter is bounded for wind solutions, since weaker magnetic fields ($a_0 \ll 1$) cause the MRI to dominate and drive redistribution of angular momentum. On the other hand, stronger magnetic fields ($a_0 \gtrsim 1$) inhibit wind launching due to their stiffness (KSW10).

Temperature: We assume that the disc is vertically isothermal and prescribe the radial temperature profile via the minimum mass solar nebula (MMSN) prescription (Hayashi 1981; Hayashi et al. 1985),

$$T(r) = T_0 \left(\frac{r}{1\ \mathrm{au}} \right)^{-q}, \tag{2.17}$$

for which $T_0 = 280$ K and $q = 0.5$. Recent observations confirm $q = 0.5$ as a reasonable value for circumstellar discs (Andrews & Williams 2005, 2007). The disc temperature is a complex function of key parameters, such as composition, abundance and properties of dust grains, density, ionization state, disc activity, chemistry, as well as the penetration of external radiation fields (X-rays, cosmic rays, and stellar irradiation).

Surface density: For the surface density, we adopt a radial power-law dependence of the form

$$\Sigma(r) = \Sigma_0 \left(\frac{r}{1\ \mathrm{au}} \right)^{-p}, \tag{2.18}$$

similar to the MMSN formulation, where the surface density at any radius is defined by

$$\Sigma = 2 \int_0^{z_s} \rho \mathrm{d}z. \tag{2.19}$$

$\Sigma(r)$ directly influences the amount of ionizing radiation that reaches the disc midplane. This in turn controls the ionization balance, and resulting conductivity structure, which governs the dynamics and evolution of the disc. The radial surface density structure of a purely wind-driving disc is expected to be flatter and thinner than a MMSN disc (Combet & Ferreira 2008), however according to observations, both Σ_0 and p have large ranges (see Andrews & Williams 2007; Persson et al. 2016). This is taken into account in the present models by choosing a range of values for Σ_0 that are lower than that of the MMSN, as well as flatter radial profiles (lower values of p).

Mass accretion rate: We define the 'local' mass accretion rate as

$$\dot{M}_{\rm acc}(r) = -2\pi r \int_{-z_{\rm b}}^{z_{\rm b}} \rho v_{\rm r} {\rm d}z. \tag{2.20}$$

This measures the mass of material falling inward through a disc annulus centred at radius r per unit time. Using equation (2.20), we define the mass accretion rate at the inner radius of the wind-launching region ($r_{\rm in}$) as

$$\dot{M}_{\rm in} = \dot{M}_{\rm acc}(r_{\rm in}). \tag{2.21}$$

Following this, we calculate $\dot{M}_{\rm acc}$ at larger radii r by adding the wind mass flux between $r_{\rm in}$ and r to $\dot{M}_{\rm in}$ (see Section 2.4.2). The accretion rate and wind mass flux are derived by vertical integration of the steady-state mass conservation law in cylindrical coordinates

$$\frac{1}{r}\frac{\partial}{\partial r}\left(r\rho v_{\rm r}\right) + \frac{\partial}{\partial z}\left(\rho v_z\right) = 0. \tag{2.22}$$

This integration is performed between $-z_{\rm b}$ and $z_{\rm b}$, where $z_{\rm b}$ is the vertical height of the disc surface (the height above which $v_\phi > v_{\rm K}$), since material begins to move radially outward via the magnetocentrifugal mechanism above $z_{\rm b}$. Thus we obtain

$$\frac{\rm d}{{\rm d}r}\int_{-z_{\rm b}}^{z_{\rm b}} 2\pi r\rho v_{\rm r}{\rm d}z + 4\pi r\rho_{\rm b} v_{\rm zb} = 0. \tag{2.23}$$

Combining equation (2.20) with the wind mass loss rate

$$\dot{M}_{\rm wind}(r) = 4\pi \int_{r}^{r_{\rm out}} r'\rho_{\rm b} v_{\rm zb}{\rm d}r', \tag{2.24}$$

where $r_{\rm out}$ is the outer radius of the wind-launching region, equation (2.23) can be rewritten as

$$\frac{\rm d}{{\rm d}r}\dot{M}_{\rm acc}(r) = 4\pi r\rho_{\rm b} v_{\rm zb} = -\frac{\rm d}{{\rm d}r}\dot{M}_{\rm wind}(r). \tag{2.25}$$

This implies

$$\dot{M} = \dot{M}_{\rm acc}(r) + \dot{M}_{\rm wind}(r) = {\rm const} \tag{2.26}$$

(e.g. Kuncic & Bicknell 2004), where $\dot{M}$ is the total mass flux at large radii. Hence the radial profiles of mass accretion rate and wind mass loss rate are inextricably linked.

In addition to the quantities listed above, we define the cumulative wind mass loss rate over the entire wind-launching region as

$$\dot{M}_{\rm out} = \dot{M}_{\rm wind}(r_{\rm in}). \tag{2.27}$$

The ratio $\dot{M}_{\rm out}/\dot{M}_{\rm in}$ is the ejection/accretion ratio, which is a key observational parameter for constraining the acceleration mechanism in protostellar disc winds and jets. For disc winds, the

Table 2.1 A listing of both the parameters used to describe the 1+1.5D solutions and those that describe the 1.5D radially localized wind-driving disc solutions.

1+1.5D parameters	
$a_0(r)$	Radial profile of the ratio v_A/c_s at the disc midplane
$T(r)$	Radial isothermal disc temperature profile
$\Sigma(r)$	Radial surface density profile
$\dot{M}_{in}$	Mass accretion rate at the inner radius r_{in}
1.5D parameters	
a_0	Ratio v_A/c_s at the disc midplane
c_s/v_K	Geometric disc thickness ratio
$[\eta_H/\eta_O]_0$	Midplane Hall-to-Ohm diffusivity ratio
$[\eta_A/\eta_O]_0$	Midplane ambipolar-to-Ohm diffusivity ratio
Λ_0	Midplane field-neutral coupling parameter
ϵ	Normalized inward radial speed at the disc midplane

one-sided ejection/accretion ratio ($\dot{M}_{out}/2\dot{M}_{in}$) is predicted to be 0.1 (Pelletier & Pudritz 1992), with recent observations confirming this (e.g. Cabrit 2007; Ellerbroek et al. 2013; Watson et al. 2016). In Section 2.6, we determine the dependence of $\dot{M}_{out}/\dot{M}_{in}$ on the accretion rate $\dot{M}_{in}$ and the radial profiles of the magnetic field strength via $a_0(r)$, and the surface density $\Sigma(r)$.

2.4.2. Constructing the disc model

Now that we have set the 1+1.5D framework, we can begin building our model from 1.5D solutions. In order to convey the method clearly, we first describe how we arrive at a 1.5D solution for any given combination of values for the set of four 1+1.5D parameters a_0, T, Σ, and $\dot{M}_{acc}$. We then outline our procedure for finding both r_{in} and its corresponding local solution given these values, and conclude with our approach for extending the model outward from r_{in} and how we determine the outer edge of the wind-launching region r_{out}.

For any given combination of values for a_0, T, Σ, and $\dot{M}_{acc}$, defined at a particular radius r, and for a stellar mass $M_\star$, there may exist a unique local solution which satisfies these values. Each 1.5D solution is characterized by six parameters (see Table 2.1 and Section 2.3.1 for more detail), and each of these local parameters must be derived from the 1+1.5D parameters (including

r and $M_\star$) in order to calculate the matching 1.5D solution. While a_0, T, r, and $M_\star$ are used to directly calculate the local parameters, Σ and $\dot{M}_{\rm acc}$ may only be determined once the local solution is known. Therefore, we begin by estimating the values of ρ_0 and $v_{\rm r0}$, the midplane density and radial velocity respectively, and evaluate Σ and $\dot{M}_{\rm acc}$ from the resulting solution. We then adjust the values of ρ_0 and $v_{\rm r0}$ accordingly, and iterate on them until the resulting Σ and $\dot{M}_{\rm acc}$ match their assigned values to within 10^{-6}. Using this method, we can now find the inner radius of the wind-launching region and its corresponding solution.

To find $r_{\rm in}$ and its solution, we begin by specifying the radial profiles of $a_0(r)$, $T(r)$, $\Sigma(r)$, and the accretion rate at the inner edge of the wind region, $\dot{M}_{\rm acc} = \dot{M}_{\rm in}$ (we vary these profiles in Section 2.6 in order to measure the dependency of the wind-launching region on them). We then search for the innermost radius which satisfies these requirements while being physically viable (see Section 2.3.3 for a detailed description of the constraints which determine whether a solution is physically viable). This involves first finding a valid solution at any radius that satisfies the 1.5D constraints, and then stepping inwards in r until solutions become invalid. We then take the smallest radius which gives a valid solution and designate it $r_{\rm in}$, and its solution becomes the basis for constructing the rest of the 1+1.5D model.

Once the inner radius and its solution are known, we calculate solutions at logarithmically increasing intervals of radius until they are no longer valid. These discrete intervals are defined by

$$r_{\rm i+1} = 10^{1/k} r_{\rm i}, \tag{2.28}$$

or

$$\Delta r_{\rm i} = r_{\rm i+1} - r_{\rm i} = (10^{1/k} - 1) r_{\rm i}, \tag{2.29}$$

where k is the number of 1.5D solutions per decade of radius. We choose $k = 1000$ for all models described in this paper based on a numerical convergence study, which is included in Appendix A.

The 1+1.5D profiles $a_0(r)$, $T(r)$, and $\Sigma(r)$ are already defined for all r, so that the only parameter remaining to calculate at each new radial step $r_{\rm i} + \Delta r$ is the local mass accretion rate. This is determined by adding the wind flux in the interval $[r_{\rm i}, r_{\rm i} + \Delta r]$ to the local accretion rate at $r_{\rm i}$,

$$\begin{aligned} \dot{M}_{\rm acc}(r_{\rm i} + \Delta r) &= \dot{M}_{\rm acc}(r_{\rm i}) + \dot{M}_{\rm wind}(r_{\rm i}) - \dot{M}_{\rm wind}(r_{\rm i} + \Delta r) \\ &= \dot{M}_{\rm acc}(r_{\rm i}) + 4\pi \int_{r_{\rm i}}^{r_{\rm i}+\Delta r} r \rho_{\rm b}(r) v_{\rm zb}(r) {\rm d}r \\ &\simeq \dot{M}_{\rm acc}(r_{\rm i}) + 4\pi r_{\rm i} \rho_{\rm b}(r_{\rm i}) v_{\rm zb}(r_{\rm i}) \Delta r \end{aligned} \tag{2.30}$$

(see equation 2.25). This process is repeated until we reach a radius where the solution is no longer valid, thus defining the outer radius of the wind-launching region, $r_{\rm out}$.

2.4.3. Constraints on the disc model

In order for our 1+1.5D models to be self-consistent, they must not violate the equations and assumptions on which the individual 1.5D solutions are based. These solutions are described in detail by WK93 and KSW10, and we summarized their main characteristics in Section 2.3. We now discuss how we preserve the assumptions of each solution, and other continuity properties within our 1+1.5D model.

The primary assumption employed by KSW10 in their 1.5D models is that of geometrical thinness, which permits neglecting the radial derivative terms ($|\partial/\partial r| \sim 1/r$) in the equations of MHD in comparison with vertical derivative terms ($|\partial/\partial z| \sim 1/z_{\rm h}$), where $z_{\rm h}$ ($\ll r$) is the disc density scaleheight. In Sections 3.2–3.10 of KSW10, this assumption simplifies the axisymmetric equations of non-ideal MHD into a set of six ODEs in z. For each of the 1+1.5D models, we ensure that the disc remains geometrically thin at all radii, thereby fulfilling this requirement.

The 1+1.5D models must also satisfy $\nabla \cdot \mathbf{B} = 0$ to prevent an unrealistic magnetic field configuration. In the axisymmetric limit, this constraint is:

$$\frac{1}{r}\frac{\partial}{\partial r}\left(rB_{\rm r}\right) + \frac{\partial}{\partial z}\left(B_z\right) = 0, \tag{2.31}$$

and by neglecting the radial derivative, equation (2.31) implies that B_z is constant with height. This result is used in the 1D solution.

In order to adequately satisfy the divergence constraint in the 1+1.5D models, it is sufficient to show that the scale height of B_z implied by the radial component of the magnetic flux density, $B_{\rm r}(r,z)$ is much larger than the disc scale height. To check this, we take the profile of $B_{\rm r}(r,z)$, calculated by interpolating $B_{\rm r}$ over the extend of the completed 1+1D model in $(r,\, z)$ space, calculate $r^{-1}\partial(rB_{\rm r})/\partial r$, and then use equation (2.31) to estimate a local scale length, L, for B_z, that is,

$$L = B_z\left(\frac{\partial B_z}{\partial z}\right)^{-1}. \tag{2.32}$$

If $L \gg z_{\rm h}$ then the $\nabla \cdot \mathbf{B} = 0$ condition is adequately met. We have checked that this condition is satisfied at all points in all of our 1+1.5D models, and include results for L in Appendix B for the strong-wind model described in Section 2.5.2.

2.5. A comparison of weak and strong wind-driving discs

We now examine in detail the internal structure of the wind-launching region in protostellar discs for two distinct cases. We prescribe both discs with a surface density profile $\Sigma(r) = 630(r/\mathrm{au})^{-1.0}$ g cm^{-2}, and a magnetic field strength B_z corresponding to $a_0 = 1.0$. We purposely choose the surface density constant Σ_0 and power-law index p (see equation 2.18) to be lower than the MMSN values of $\Sigma_0 = 1700$ g cm^{-2} and $p = 1.5$ respectively, because of the expectation that the radial surface density structure of a purely wind-driving disc is thinner and flatter than a MMSN disc (Combet & Ferreira 2008). However, we investigate the effect of changing Σ_0 and p in Section 2.6.

We prescribe the first model with an accretion rate of $\dot{M}_{\rm in} = 1.0 \times 10^{-5} M_\odot$ yr^{-1}, and the second with $\dot{M}_{\rm in} = 1.6 \times 10^{-5} M_\odot$ yr^{-1}, then calculate the extent of the 1+1.5D model via the procedure described in Section 2.4. We find that the first model exhibits a weak wind ($\dot{M}_{\rm out}/\dot{M}_{\rm in} = 1.3 \times 10^{-2}$) relative to the second ($\dot{M}_{\rm out}/\dot{M}_{\rm in} = 3.5 \times 10^{-2}$) and hence we refer to them as the weak and strong wind models for the remainder of this paper.

2.5.1. Weak-wind model

The density, velocity, and magnetic field structure of the weak-wind model is displayed in Fig. 2.2. The magnetic field lines in Figs. 2.2 and 2.3 are calculated from their vertical and radial components, where all three components of the magnetic field ($B_{\rm r}$, B_ϕ, B_z) are calculated in each 1.5D vertical model. To make the 2D images in Figs. 2.2 and 2.3, we simply interpolate the $B_{\rm r}$ and B_z components in (r, z) space. We use a similar procedure for the velocity field, and perform a basic interpolation for the density.

The wind-launching region of the disc is radially localized, and extends from ~ 0.60 to 1.14 au. However, between ~ 0.63 and 0.92 au there exists a region, which the mass loading constraint defines as ineffective to wind launching, which we denote the 'inactive' region (see Section 2.3.3). Essentially, the extrapolated B_ϕ in this region changes sign below $z = r$, signalling an unphysical transfer of angular momentum from the field back to the matter. Hence a stable CDW cannot operate within this radial range, and we do not include the contribution of the solutions in this region to the total wind mass loss rate $\dot{M}_{\rm out}$. Despite there being no capacity to launch a stable wind in the inactive region, this does not rule out unstable launching configurations such as episodic outbursts from existing here, however in order to verify this and determine the

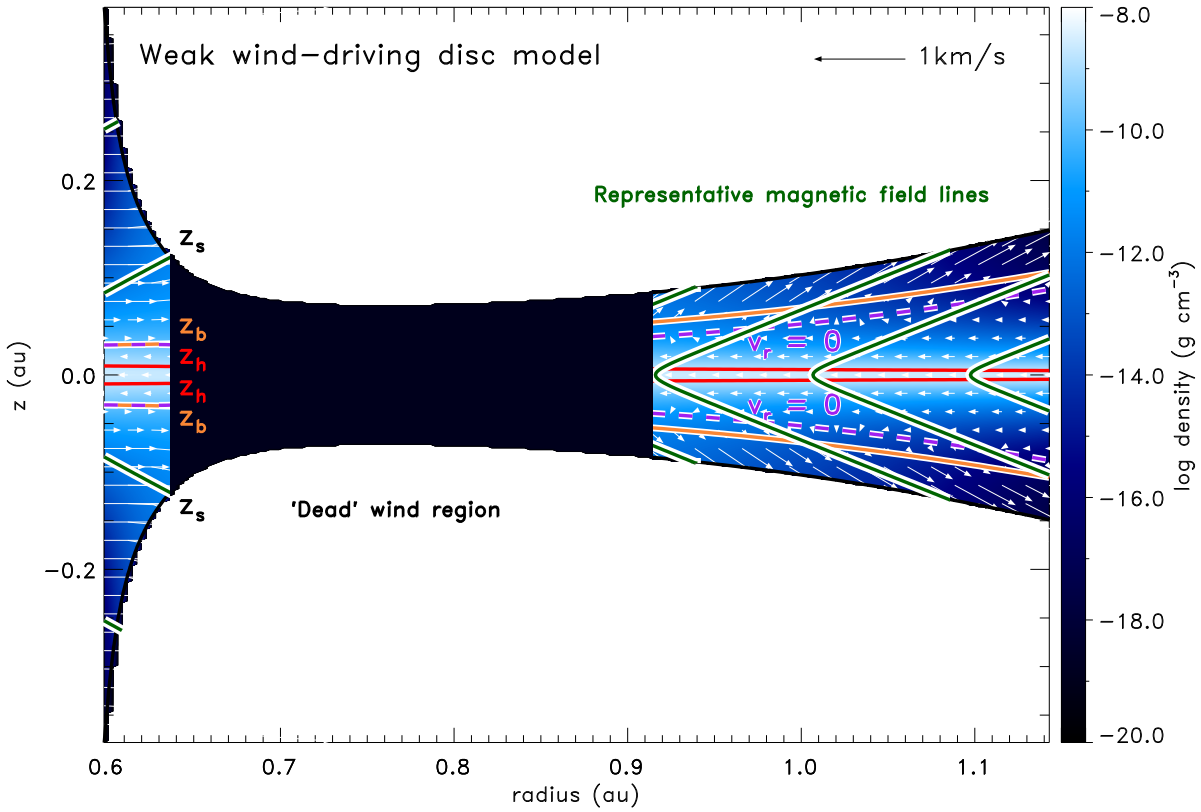

Figure 2.2 A poloidal slice of the weak-wind (lower ejection/accretion ratio) disc model. The density contour plot is overlaid with velocity vectors in white and green lines to show the bending of magnetic field lines. The black area defines the region where wind solutions are unphysical according to the mass-loading constraint; the 'inactive' region (see Section 2.3.3). The red lines indicate the magnetically reduced disc scale height z_h and the orange lines show the location of the disc surface/base of the wind z_b, defined as the height at which the azimuthal velocity of the gas transitions from sub-Keplerian ($z < z_b$) to super-Keplerian ($z > z_b$). The black lines indicate the sonic surface z_s. The purple dashed lines indicate the extents of the accretion region within the disc, where $v_r < 0$.

dominant mode of angular momentum transport in this region, a time-dependent treatment of the disc is necessary, which is beyond the scope of this paper.

It is worth noting that despite the appearance of a sharp cutoff for the inactive region in Fig. 2.2, the assumptions used in formulating the mass-loading constraint are approximate. Hence the radial extent of this region is to be treated as a first approximation, and likewise the values for the total bipolar wind mass-loss rate, as they are directly connected to the radial extent of the wind-launching region.

The accretion region within the disc is the zone where the flow proceeds inwards ($v_r < 0$). The boundaries of this region are marked by the purple dashed lines in Fig. 2.2. At the inner wind radius ($r = 0.6$ au), the accretion region is located between ±0.031 au, which is, equivalently,

$\pm 3.3\ z_h$ and $\pm 1.8\ h_T$. Similarly, at the outer wind radius ($r = 1.14$ au), the accretion region is located between ± 0.088 au, equivalently $\pm 19\ z_h$ and $\pm 2.2\ h_T$.

Note that the disc in Fig. 2.2 exhibits the three distinct layers described by Königl & Salmeron (2011). The *quasi-hydrostatic region* straddles the disc midplane ($|z| < z_h$), and is matter dominated; the majority of mass accretion and magnetic field bending and shearing take place in this region (as apparent by the white velocity vectors and overlaid magnetic field lines in green). Above the quasi-hydrostatic layer lies the *transition zone* ($z_h < |z| < z_b$). In this layer the magnetic field lines become locally straight as the density decreases and the flow becomes magnetically dominated. The inward radial flux of matter gradually decreases, and the flow transitions to a CDW (as shown by the white velocity vectors). At the top of the transition zone the flow changes from sub-Keplerian ($v_\phi < v_K$) to super-Keplerian ($v_\phi > v_K$). This point represents the base of the wind (z_b), above which lies the *outflow region* ($z_b < |z| < z_s$). Here the flow continues to accelerate until it reaches the sonic surface (z_s) which defines the extent of the model.

The mass accretion rate through the inner boundary for the weak-wind model is $\dot{M}_{in} = 1.0 \times 10^{-5} M_\odot\ \mathrm{yr}^{-1}$, with a total bipolar-wind mass loss rate $\dot{M}_{out} = 1.3 \times 10^{-7} M_\odot\ \mathrm{yr}^{-1}$. This equates to an ejection/accretion ratio $\dot{M}_{out}/\dot{M}_{in} = 1.3 \times 10^{-2}$, which is approximately an order of magnitude lower than the observationally inferred average of 0.1–0.2, but nonetheless it is exhibited by some protostellar systems (see Cabrit 2007, Fig. 1). These and other properties of the disc at the inner and outer radii of the wind-driving region, such as the Ohm, Hall, and ambipolar diffusivities and scale heights, are listed in Table 2.2.

2.5.2. Strong-wind model

The strong-wind model (Fig. 2.3) has a similar radial profile to the weak-wind model, with an elevated disc surface (z_b) and sonic surface (z_s) at small radii, however this model does not possess an internal magnetically inactive region. The wind-launching region of the disc extends from ~ 0.56 to 0.93 au, and is located closer to the star than that of the weak-wind model discussed above. Similar to the weak-wind model, the wind-launching region is localized, with maximum wind output at $r = 0.65$ au, and rapid attenuation of wind output on either side (see Section 2.5.3).

At the inner wind radius of the strong-wind model ($r = 0.56$ au), the accretion region is located between ± 0.034 au, or equivalently, $\pm 4.7\ z_h$ and $\pm 2.1\ h_T$. At the outer wind radius, this region expands to ± 0.076 au, or $\pm 21\ z_h$, and $\pm 2.5\ h_T$.

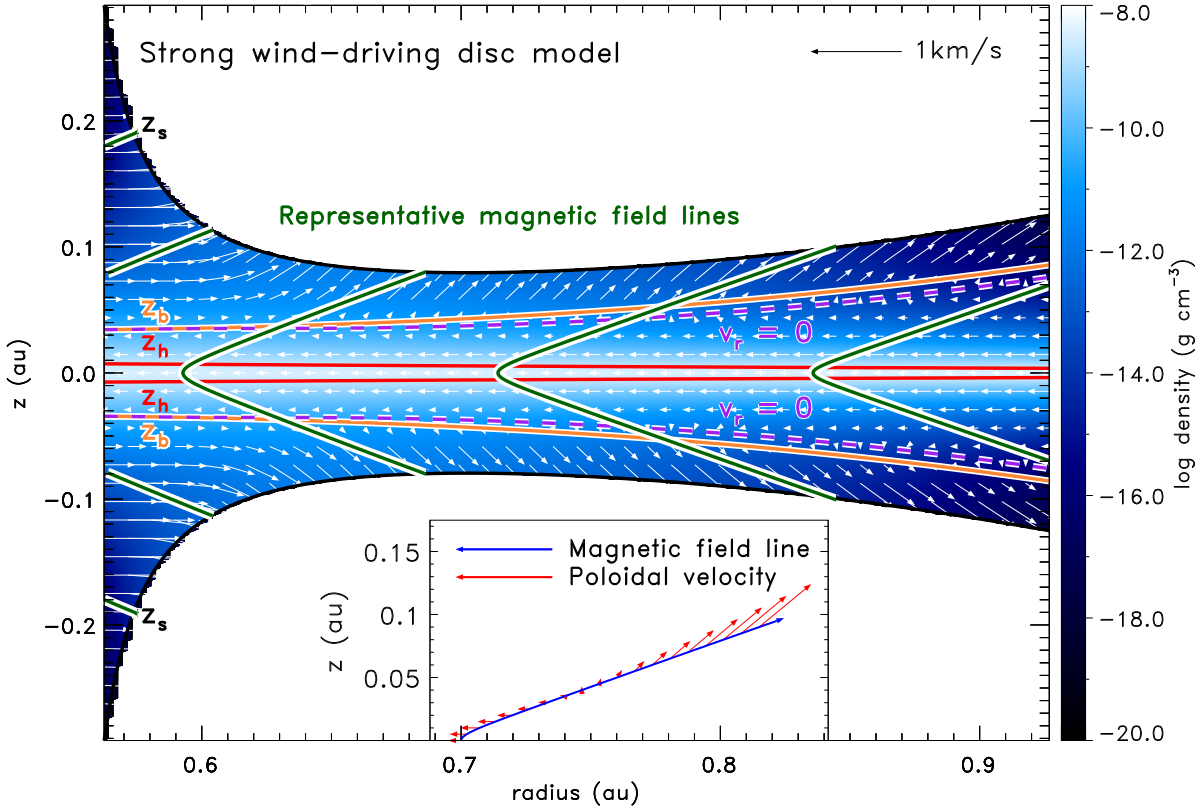

Figure 2.3 A poloidal slice of the strong-wind disc model. See Fig. 2.2 for a description of the features of this plot. In addition, this plot includes an inset, comparing a sample magnetic field line anchored at 0.7 au with the velocity field along its length. We discuss the features of this comparison in Section 2.5.2.

The mass accretion rate through the inner boundary of this model is $\dot{M}_{\rm in} = 1.6 \times 10^{-5} M_\odot$ yr^{-1}, with a total bipolar-wind mass loss rate of $\dot{M}_{\rm out} = 5.6 \times 10^{-7} M_\odot$ yr^{-1}. This results in an ejection/accretion ratio $\dot{M}_{\rm out}/\dot{M}_{\rm in} = 3.5 \times 10^{-2}$, which is also lower than the mean observed range of $\simeq$ 0.1–0.2 for protostellar discs, but some individual observed discs show such low values (Cabrit 2007; Ellerbroek et al. 2013; Watson et al. 2016). This value is a factor of 2.7 larger than that of the weak-wind model. The relation between $\dot{M}_{\rm in}$ and $\dot{M}_{\rm out}$ as a function of 1+1.5D disc properties is explored in further detail in Section 2.6.

In the inset of Fig. 2.3, we compare the angle between the magnetic and velocity field vectors along a single magnetic field line. As expected, the magnetic field begins at right angles to the flow, and is bent outward, consistent with the flow of neutrals towards the centre of the system, and the support of matter against gravity by magnetic tension, given that the flow is sub-Keplerian. Moving up to the transition zone, the field line becomes locally straight as the flow transitions to being magnetically dominated. This causes the velocity field to gradually align with the magnetic field as it moves away from the disc midplane. It is expected that the

two fields will eventually align perfectly when moving into the ideal MHD regime. This is not seen in our models, because we do not follow the wind solutions into the regions of near-ideal MHD, and in particular, our current model does not account for the physical dependence of the Elsasser number on z (which will be addressed in a subsequent paper).

2.5.3. Radial dependence of mass accretion and outflow rates

The radial dependence of the local mass accretion rate $\dot{M}_{\rm acc}$ and wind mass loss rate per unit radius $\mathrm{d}\dot{M}_{\rm wind}/\mathrm{d}r$ for the weak-wind and strong-wind models are shown as the dashed and solid lines in Fig. 2.4, respectively. For the weak-wind model, the local wind outflow rate increases towards intermediate radii, but above $\mathrm{d}\dot{M}_{\rm wind}/\mathrm{d}r \approx 3\times10^{-6} M_\odot\ \mathrm{yr}^{-1}\ \mathrm{au}^{-1}$ the wind solutions become unphysical and the disc becomes ineffective to wind-launching. For the strong-wind model, the region of highest wind mass loss is between $0.6 < r < 0.8$ au, peaking at $r = 0.65$ au.

To understand why the outflow is radially localized, we break down the explanation into two parts: Firstly, we explain the decrease in the wind outflow rate towards smaller radii in the inner section of the wind-launching region. This is primarily a result of weakened coupling between the field and the matter in the inner regions of the disc, with the midplane Elsasser number approaching $\Lambda_0 = 1$ towards the inner limit of the wind region, from a value of $\Lambda_0 = 12$ at the outer limit (see Table 2.2). As shown by KSW10, disc properties behave quite differently for $\Lambda_0 \lesssim 1$. Referring to the description of a CDW mechanism by Königl & Salmeron (2011), decreased coupling between the field and the neutrals leads to the following effects: the azimuthal velocity v_ϕ increases as the magnetic torque diminishes and as such, the inward flow of neutrals decreases. This reduces the radial drag on the magnetic field lines, contributing to a decrease in $B_{\rm r}/B_{\rm z}$, which reduces the magnetic compression of the disc and results in lower density stratification. The angle between the surface magnetic field and the rotation axis is critical to launching a wind (BP82), hence, as $B_{\rm r}/B_{\rm z}$ decreases the local wind mass loss rate $\mathrm{d}\dot{M}_{\rm wind}(r)/\mathrm{d}r \to 0$. In effect, this drop in wind mass loss rate supports the validity of the simplified wind launching criterion for non-ideal MHD (equation 2.13), for none of the models in this paper actually violate equation (2.13), as the solutions approach the inward radius where this criterion would be violated, the wind drops to negligible levels.

The increase in the height of the sonic surface with decreasing r for $r < 0.7$ au can also be explained via the field-matter coupling. The decrease in $B_{\rm r}/B_{\rm z}$ combined with lower coupling reduces the extraction of angular momentum via the wind, and therefore the vertical distance

required for v_z to reach the sound speed (z_s) grows. Hence the height of the sonic surface above the disc increases as the field-matter coupling weakens.

Secondly, we explain the decrease in the wind outflow rate towards larger radii in the outer region of the wind. In this region, the field-matter coupling continues to increase with radius (see Fig. 2.5). This reduces the azimuthal velocity v_ϕ as the magnetic torque increases, increasing the inward flow of neutrals and leading to greater field bending in both the radial and azimuthal directions (i.e. the ratios B_r/B_z and B_ϕ/B_z). However, even though these are favourable conditions for wind launching, another effect becomes important here which counters the launching of a wind. Due to the increased field bending at larger radii, magnetic compression of the disc material results in a lower density at the disc surface, producing a lower density wind with a lower mass loss rate. This is amplified by the rising of the disc surface z_b with radius, leading to an even lower density wind. Since the azimuthal velocity at the disc midplane ($v_{\phi 0}$) decreases with radius as a result of increased field-matter coupling, the vertical distance required for v_ϕ to reach the Keplerian speed (v_K) grows. Hence the disc surface, defined as the height at which $v_\phi = v_K$, rises with radius, and as a result the wind density decreases, and the outflow rate becomes negligible. Thus the wind-launching region is radially localized as a consequence of two independent mechanisms, one operating at inner radii, and the other at outer radii.

2.5.4. Comparison with other models

Comparing our work to the models of Bai & Stone (2013b), we find some significant differences. Firstly, the values of z_b/h_T are twice as large as those found in our study over the entire radial range. In Bai & Stone (2013b) the models are centred at 1 au, and give values of $z_b/h_T \sim 4.6$, whereas those found in our two fiducial models have values between 1.8 and 2.7 for the weak wind, and 2.1–2.8 for the strong wind. This difference is caused by the vastly different magnetic field strengths in both simulations. In our models, the midplane magnetic field is 10^5 times stronger, leading to much larger compressive forces on the disc.

Secondly, the field morphologies of both models are completely different. The models of Bai & Stone (2013b) contain a laminar region near the disc midplane, associated with relatively little field-line bending due to the strong diffusion and weak field strength (see their Figure 6). On the other hand, the field lines in our models begin to bend immediately above the disc midplane as expected (see inset to Fig. 2.3), given the relatively large field strength.

Thirdly, Bai & Stone (2013b) find that both the Ohmic and ambipolar Elsasser numbers must

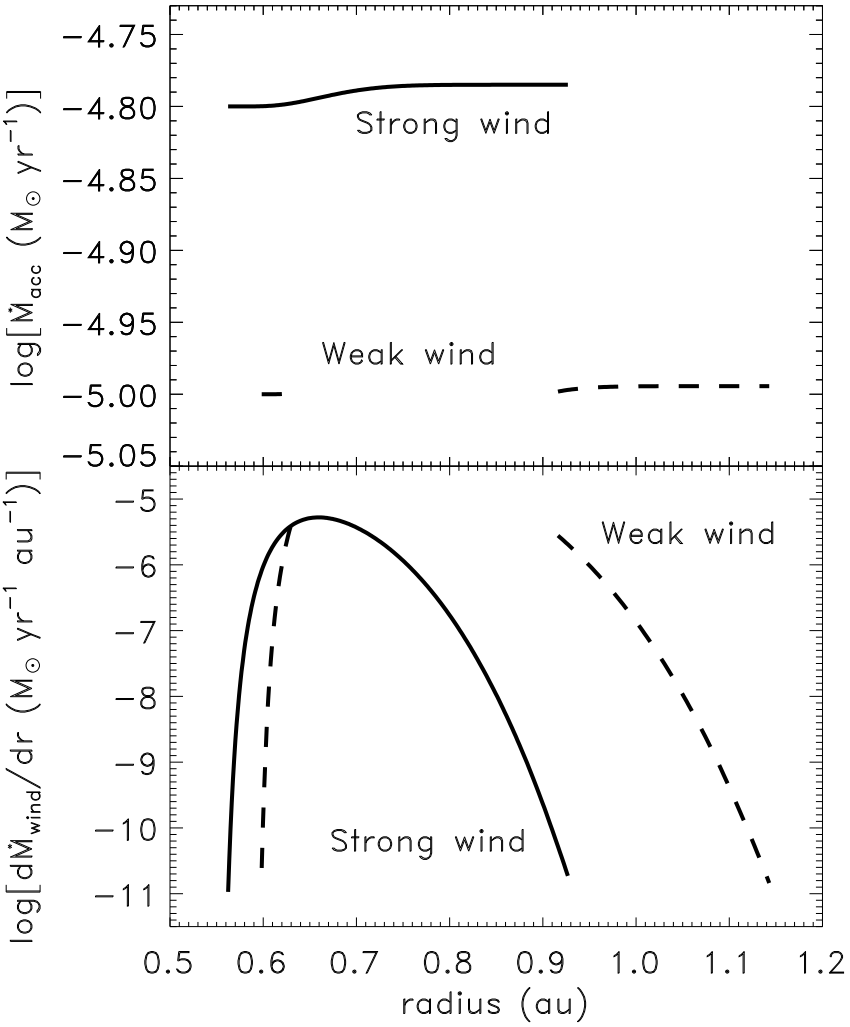

Figure 2.4 Local mass accretion rate $\dot{M}_{\rm acc}$ (top panel) and wind mass loss rate per unit radius $\mathrm{d}\dot{M}_{\rm wind}/\mathrm{d}r$ (bottom panel) as a function of radius for the weak-wind (dashed line) and strong-wind (solid line) models displayed in Figs. 2.2 and 2.3 respectively.

exceed unity in order to facilitate wind launching, which means that the total Elsasser number must remain above unity. Due to the simplifications of our model, the Elsasser numbers remain constant with height, however we can still check the dependence of this parameter on radius. Fig. 2.5 displays the three Elsasser numbers for both fiducial models as a function of radius. We find agreement with Bai & Stone (2013b), in that wind launching occurs where both $\Lambda_{\rm O}$ and $\Lambda_{\rm A}$ exceed unity. Hence we find it to be a necessary but not sufficient condition for wind launching.

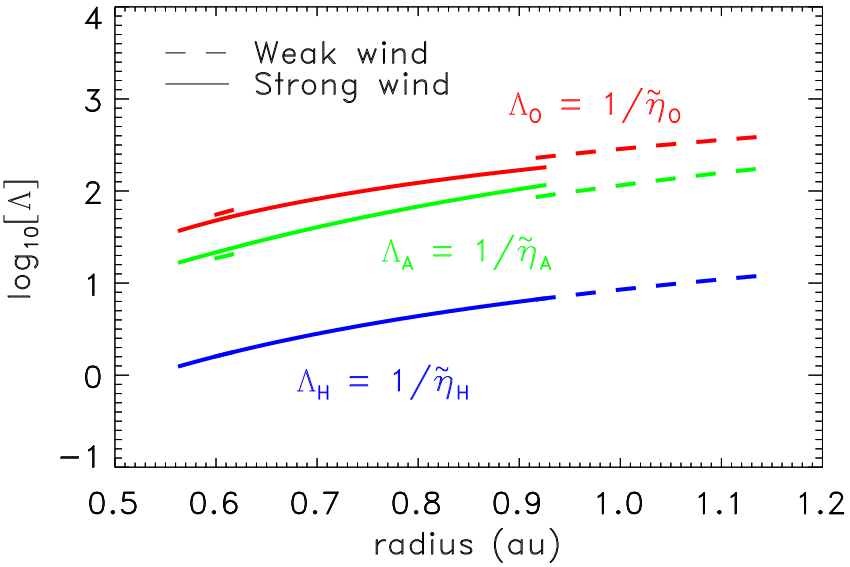

Figure 2.5 Radial profile of the Ohmic (Λ_O), Hall (Λ_H), and ambipolar (Λ_A) Elsasser numbers, for both the weak and strong wind models (given the simplifications of the model, Elsasser numbers are constant with z).

Table 2.2 Properties of the weak and strong-wind disc models presented in Section 2.5. These properties are given at the inner (r_{in}) and outer (r_{out}) radial extents of the wind-launching region.

Disc property		Weak-wind model				Strong-wind model	
		Inner region		Outer region			
		r_{in}	r_{out}	r_{in}	r_{out}	r_{in}	r_{out}
r	[au]	0.60	0.63	0.92	1.14	0.56	0.93
ρ_0	[g cm^{-3}]	2.5×10^{-9}	2.4×10^{-9}	2.5×10^{-9}	2.9×10^{-9}	3.5×10^{-9}	4.3×10^{-9}
$\tilde{\rho}_s$		3.2×10^{-9}	7.9×10^{-4}	2.6×10^{-4}	1.0×10^{-9}	1.0×10^{-9}	1.0×10^{-9}
ϵ		0.10	0.10	0.077	0.073	0.14	0.12
η_O	[cm^2 s^{-1}]	5.4×10^{14}	4.5×10^{14}	2.0×10^{14}	1.4×10^{14}	7.6×10^{14}	2.5×10^{14}
η_H	[cm^2 s^{-1}]	1.9×10^{16}	1.6×10^{16}	6.9×10^{15}	4.7×10^{15}	2.3×10^{16}	6.7×10^{15}
η_A	[cm^2 s^{-1}]	1.6×10^{15}	1.4×10^{15}	5.3×10^{14}	3.2×10^{14}	1.7×10^{15}	4.0×10^{14}
$\Lambda_0 \approx 1/\tilde{\eta}_H$		1.6	2.0	6.6	12.	1.2	6.8
z_h	[au]	0.0092	0.0087	0.0062	0.0045	0.0072	0.0037
z_b	[au]	0.031	0.032	0.055	0.11	0.034	0.086
z_s	[au]	0.38	0.13	0.085	0.15	0.29	0.13
$[B_r/B_z]_b$		1.0	1.1	1.4	1.4	1.2	1.4
$[B_\phi/B_z]_b$		-0.037	-0.034	-0.015	-0.0090	-0.049	-0.015
$\dot{M}_{acc}$	[$M_\odot$ yr^{-1}]	1.0×10^{-5}	1.0×10^{-5}	1.0×10^{-5}	1.0×10^{-5}	1.6×10^{-5}	1.6×10^{-5}
$\dot{M}_{out}/\dot{M}_{in}$		1.3×10^{-2}				3.5×10^{-2}	

2.6. 1+1.5D wind-driving disc solutions

Now that we have studied in detail the structure of two disc-wind models, we generalize our search to include a range of models with unique disc characteristics. We use the weak-wind model analysed in Section 2.5.1 as our fiducial model, and vary the parameters $\dot{M}_{\rm in}$, a_0, Σ_0, and p (equation 2.18) one by one to investigate the resulting effects on the wind-launching region. We specifically focus on how the radial extent and ejection/accretion ratio of the wind change with disc properties, since these may be compared to other observational and theoretical predictions for disc winds.

2.6.1. Impact of the mass accretion rate $\dot{M}_{\rm in}$

We begin by exploring the result of modifying $\dot{M}_{\rm in}$, the accretion rate at the inner-most radius of the wind-launching region. This is important for studying how the wind would respond to variations in accretion rate over periods longer than a dynamical time $\tau_{\rm d}$ (i.e. the Keplerian orbital time), which could occur via fluctuations during quiescence, or throughout the restorative decline in accretion rate following an outburst event (see Audard et al. 2014). We define each 1+1.5D wind model by $a_0 = 1.0$, and a surface density profile of $\Sigma(r) = 630(r/\mathrm{au})^{-1}$ g cm^{-2}.

The results of this investigation are shown in Fig. 2.6. The top panel shows the local mass accretion rate as a function of radius, with each curve corresponding to a different choice of $\dot{M}_{\rm in}$. The wind-launching region for all models is radially localized, as can be observed from the colour-coded wind mass loss rates in the figure, with a maximum wind output between $r \sim 0.6$–0.8 au, and rapid attenuation on either side. For an explanation of why the wind is radially localized, see Section 2.5.3.

As $\dot{M}_{\rm in}$ is decreased, the radial extent of the wind-launching region expands. This can be understood using the following explanation. At lower $\dot{M}_{\rm in}$, there is less material moving radially through the disc. This corresponds to less magnetic field bending in the radial and azimuthal directions, and hence a reduction of the magnetic compression of the disc. As we described in Section 2.5.3, the less the disc is compressed, the more dense the resulting wind is. Hence lower values of $\dot{M}_{\rm in}$ lead to a higher wind mass loss rate across the radial extent of the wind, expanding the wind region where the mass loss rate is significant, and increasing the ejection/accretion ratio, as can be seen in the lower panel of Fig. 2.6.

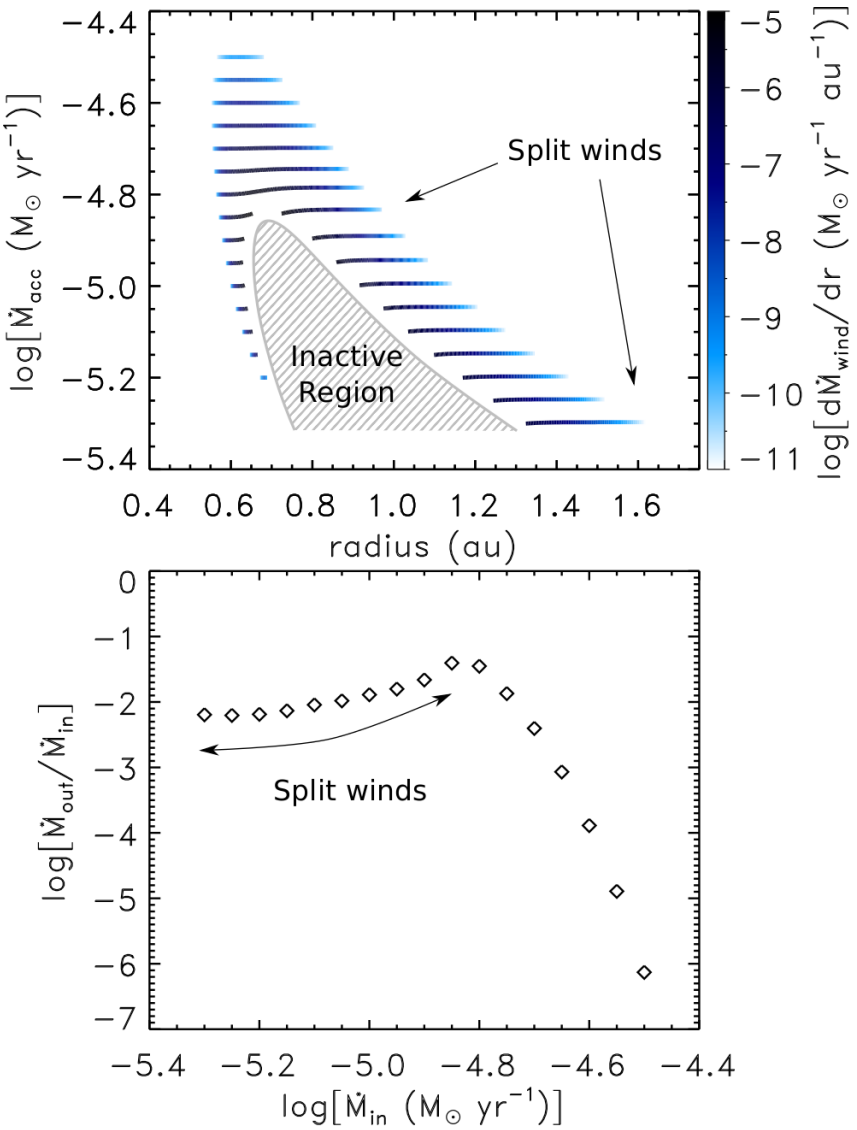

Figure 2.6 Local mass accretion rate $\dot{M}_{\rm acc}$ as a function of radius (top panel) and ejection/accretion ratio $\dot{M}_{\rm out}/\dot{M}_{\rm in}$ (bottom panel) for a series of 1+1.5D disc wind models with different $\dot{M}_{\rm in}$. Each disc is defined by an equipartition magnetic field strength at the midplane ($a_0 = 1$), and a surface density profile $\Sigma(r) = 630(r/{\rm au})^{-1}$ g cm^{-2}. The colouring in the top panel indicates the local wind mass loss rate at the disc surface along the radial extent of each model. The grey hatched area indicates the region where wind solutions are defined as unphysical due to the mass loading constraint; the 'inactive' region (see Section 2.3.3).

Below $\dot{M}_{\rm in} = 10^{-4.8} M_\odot$ yr^{-1}, however, the wind-launching region is divided in two, resulting from an intermediate portion of the disc wind becoming ineffective for launching a wind. In this 'inactive' region, the vertical mass flux would be so large that it would transport more angular momentum out of the disc than that brought in by the accretion flow, and similarly $\dot{M}_{\rm wind} \ll \dot{M}_{\rm acc}$, leading to an unphysical launching configuration and no wind (see the mass loading constraint, Section 2.3.3). High mass loss rates in protostellar disc winds lead to instability (Cao & Spruit 2002). As described above, lower values of $\dot{M}_{\rm in}$ lead to a higher wind mass loss rate across the radial extent of the wind, and hence a greater portion of the disc becomes magnetically inactive. As a result of the radial increase of the inactive region, $\dot{M}_{\rm out}/\dot{M}_{\rm in}$ steadily decreases.

2.6.2. Impact of the magnetic field strength parameter a_0

The strength of the magnetic field is important for determining not only the behaviour of disc winds, but also the characteristics of the MRI (e.g. Turner et al. 2014), and X winds (e.g. Shu et al. 1994). We now consider the impact of changing the magnetic field strength by calculating a series of 1+1.5D disc wind models with $\dot{M}_{\rm in} = 1 \times 10^{-5} M_\odot$ yr^{-1} and a surface density profile $\Sigma(r) = 630(r/{\rm au})^{-1}$ g cm^{-2}, while varying the midplane ratio of the Alfvén speed to the sound speed, a_0 (see equation 2.4).

The results of varying a_0 are shown in Fig. 2.7, and display similar trends to those of the $\dot{M}_{\rm in}$ study. All solutions are radially localized, with maximum wind output around $r \sim 0.8$–0.9 au. As a_0 is decreased, the wind-launching region expands and the ejection/accretion ratio increases. This can be explained as follows. Similar to a decrease in $\dot{M}_{\rm in}$, if the magnetic field strength is decreased, the magnetically-compressed density scaleheight ($z_{\rm h}$) increases due to less magnetic pressure, and the launch point ($z_{\rm b}$) decreases, leading to a higher wind density, and hence larger wind output and ejection/accretion ratio. This is evidenced in the bottom panel of Fig. 2.7. Changing a_0 does significantly shift the radius where the wind output peaks, however, below $a_0 = 1.25$ the launching region is divided in two due to a central section of no wind. As this inactive region expands at lower a_0, the split wind-launching regions move further away from the central radius. The splitting of the wind into two separate regions below $a_0 = 1.25$ also disrupts the rapid increase in $\dot{M}_{\rm out}/\dot{M}_{\rm in}$ leading it into a steady decline.

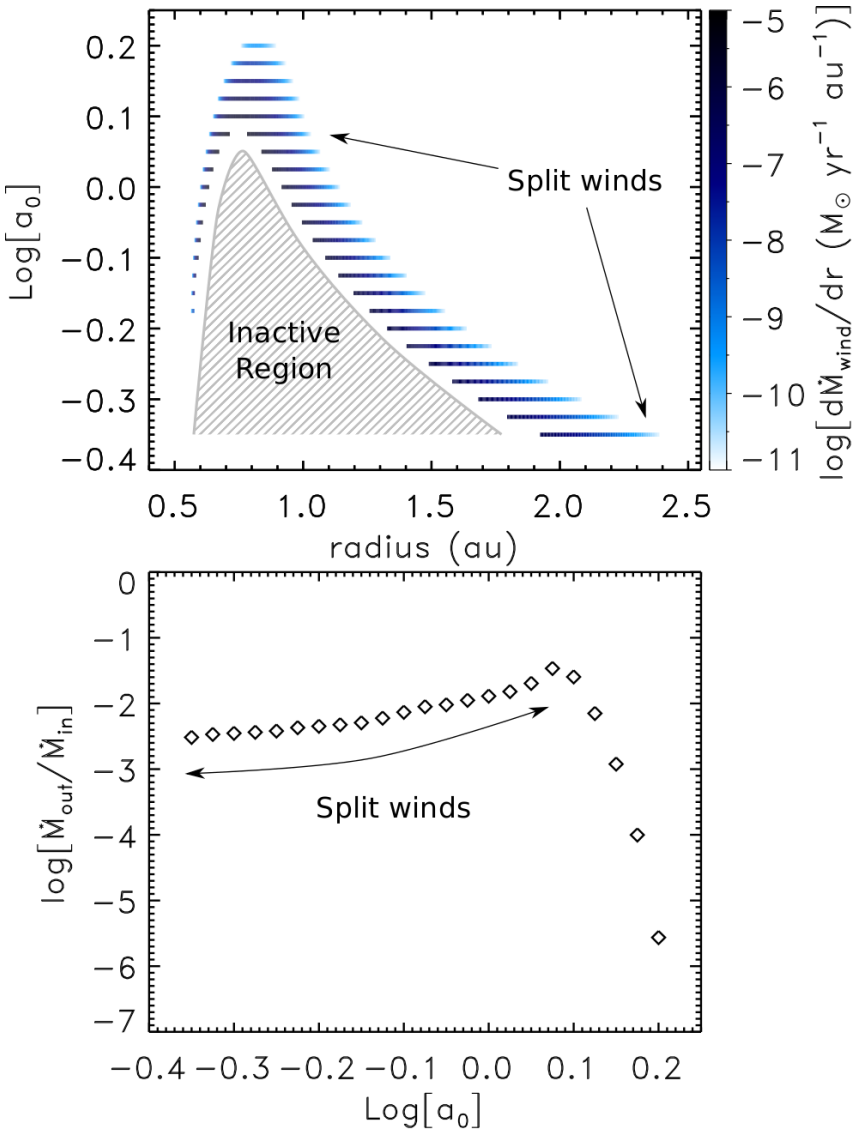

Figure 2.7 As per Fig. 2.6, however this time varying the midplane magnetic field strength via $a_0 \equiv v_{A0}/c_s$. For reference, the plasma beta is related to a_0 via the equation $\beta_0 = 2/a_0^2$.

2.6.3. Impact of the surface density normalization Σ_0

We now investigate how the behaviour of disc winds change with Σ_0 (see equation 2.18). We define each model by $a_0 = 1.0, \dot{M}_{\rm in} = 1{\times}10^{-5} M_\odot\ {\rm yr}^{-1}$, and a surface density profile $\Sigma(r) = \Sigma_0 (r/{\rm au})^{-1}$, while varying the surface density coefficient Σ_0. A change in Σ_0 corresponds to a variation in the mass of the disc. We expect to observe this in discs that are being emptied out via quiescent mass accretion (e.g. Williams & Cieza 2011; Armitage 2015), or on local scales as a result of episodic accretion (see Audard et al. 2014). Current observational estimates of Σ_0 vary substantially in the range $\Sigma_0 \sim$ 1–2000 g cm^{-2} (Andrews & Williams 2007; Persson et al. 2016).

The results are given in Fig. 2.8. The top panel shows the variation in the radial extent of the wind as a function of Σ_0. Similar to the previous two studies in Sections 2.6.1 and 2.6.2, all solutions are radially localized. For low Σ_0, the launching region exists quite close to the protostar, and moves further out for larger values. Larger surface densities decrease the amount of radiation incident upon the disc midplane (see Appendix C), which leads to higher magnetic diffusivity and lower field-matter coupling (eqns. 2.1–2.3 and 2.7). Since the field-matter coupling determines the inner boundary of the wind-launching region (see Section 2.5.3 for details), and Λ_0 increases with radius (see Fig. 2.5), a lower overall Λ_0 means that the inner radius of the wind region moves outward, shifting the entire wind region to larger radii.

We also observe that the wind-launching region expands as Σ_0 increases. This is a result of the power-law description of the surface density profile. As explained above, the wind-launching region is highly dependent on the value of the field-matter coupling, which is a function of surface density. Since the surface density profile is shallower at larger radii, we would expect that the optimal region for wind launching would have a larger extent. Since the wind has a larger extent at higher Σ_0, it also has a larger ejection/accretion ratio, as seen in the bottom panel of Fig. 2.8. However, above $\Sigma_0 = 400$ g cm^{-2} the wind splits in two due to no wind being launched at intermediate radii, leading to a steady decrease in $\dot{M}_{\rm out}/\dot{M}_{\rm in}$.

2.6.4. Impact of the surface density exponent, p

Finally, we explore the impact of changing the power-law dependence of the surface density, defined by the parameter p in equation (2.18), on the properties of the wind-launching region. Current power-law estimates give values for p most commonly between 0–1 (Bergin 2011; Persson et al. 2016), while $p = 1.5$ in the MMSN model. We examine discs with p between 0.1 and 1.5,

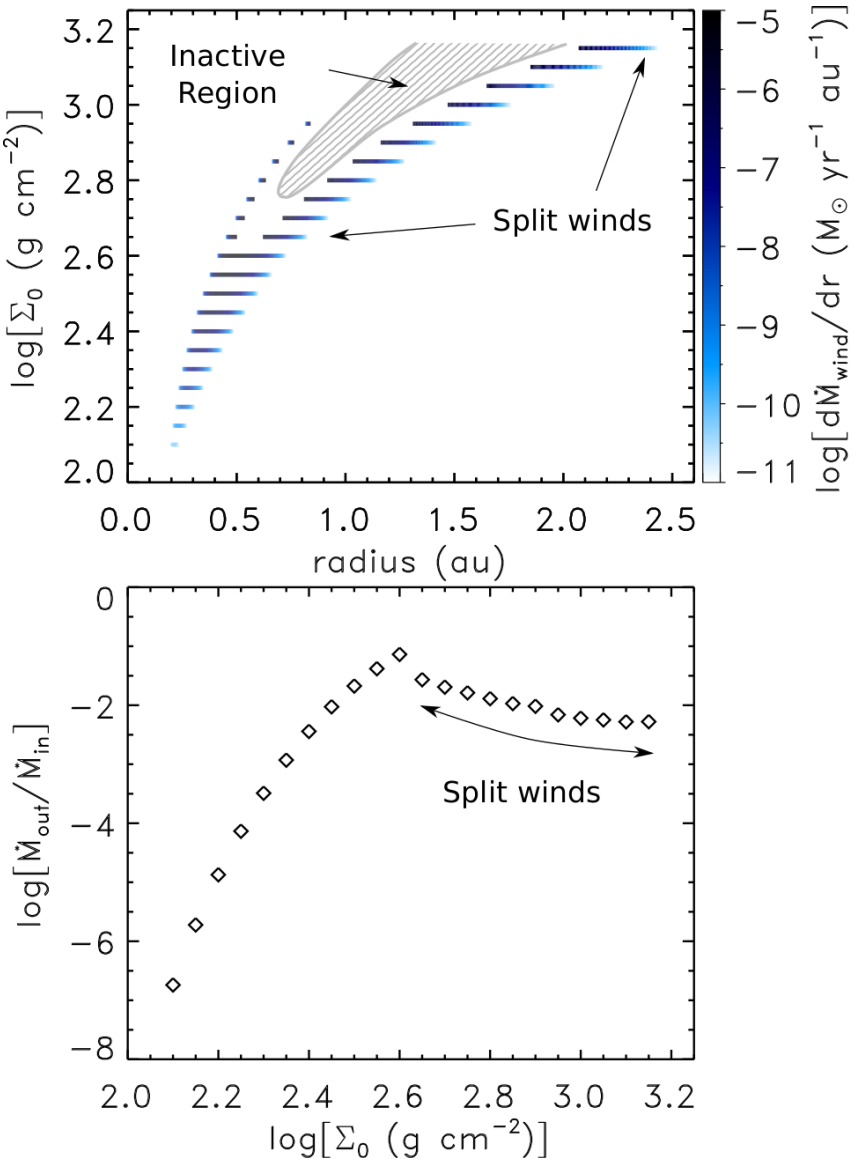

Figure 2.8 As per Fig. 2.6, however this time varying the surface density profile, specifically Σ_0 in the profile $\Sigma(r) = \Sigma_0(r/\mathrm{au})^{-1}$.

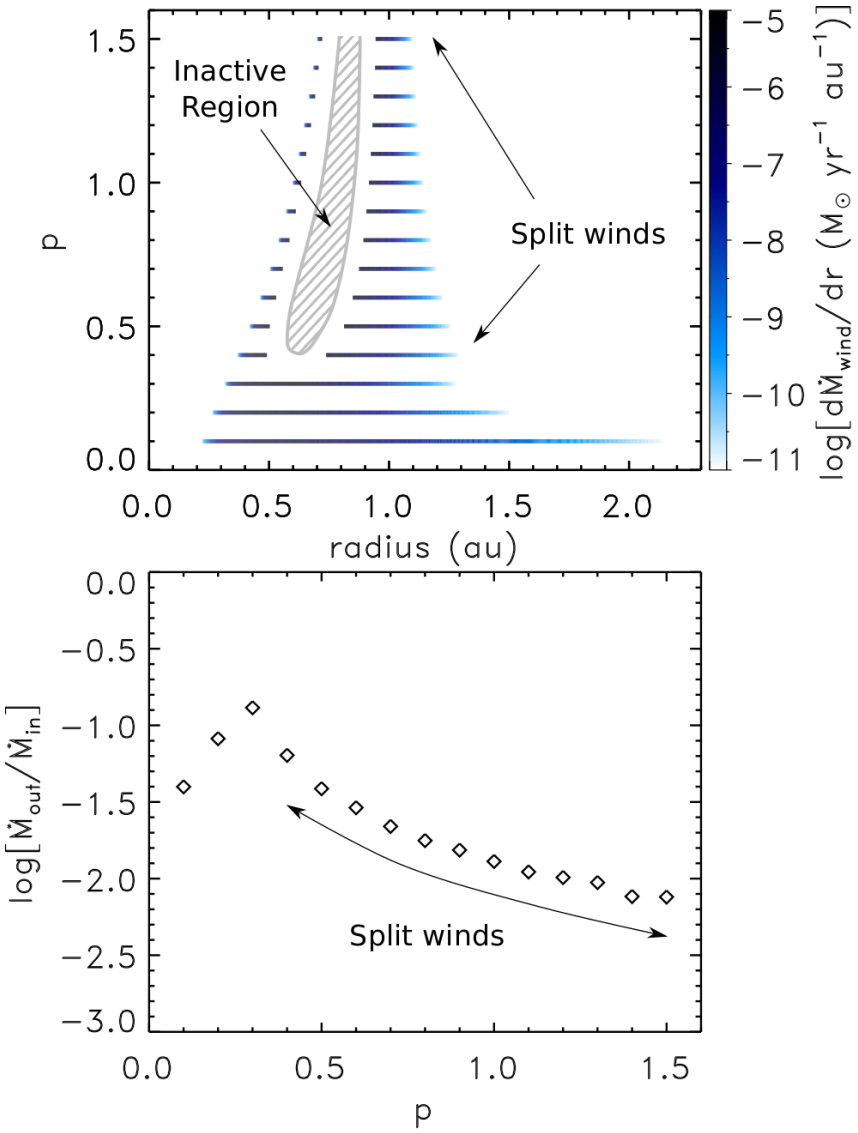

Figure 2.9 As per Fig. 2.6, however this time varying the surface density profile, specifically p in the profile $\Sigma(r) = 630(r/\mathrm{au})^{-p}$ g cm^{-2}.

assuming a disc characterized by $a_0 = 1$, $\dot{M}_{\rm in} = 1 \times 10^{-5} M_\odot$ yr^{-1}, and a surface density profile $\Sigma(r) = 630(r/{\rm au})^{-p}$ g cm^{-2}.

The results are shown in Fig. 2.9, with radial estimates for the extent of the disc wind as a function of p displayed in the top panel. Similar to the other three studies of Section 2.6, all solutions are radially localized, with no wind launching at intermediate radii for $p > 0.3$. For an almost flat profile ($p = 0.1$), the disc wind extends from $\sim$ 0.2–2.1 au, and decreases in width as p increases, until it is less than 0.4 au wide for $p = 1.5$. This occurs because as p increases, the surface density profile steepens, narrowing the region which provides field-matter coupling values favourable for wind launching.

Interestingly, $\dot{M}_{\rm out}/\dot{M}_{\rm in}$ decreases as p is lowered (ignoring split winds). This occurs because for flatter surface density profiles, the maximum local wind output is lower than for steeper profiles. As seen in the other studies, once the wind-launching region splits in two, the ejection/accretion ratio steadily declines.

2.7. Discussion

The results presented in Sections 2.5 and 2.6 provide a detailed study into the properties of disc winds and how they vary with the characteristics of the underlying disc. We specifically focus on how the radial extent and ejection/accretion ratio of the winds change with disc properties, as these two attributes may be compared to observations and theoretical predictions for disc winds.

2.7.1. Comparison with observations

For mass accretion rates in the range $10^{-5.4}$–$10^{-4.5} M_\odot$ yr^{-1}, midplane Alfvén-to-sound speed ratios between 0.45 and 1.6, surface density profiles with Σ_0 in the range 130–1400 g cm^{-2}, and p between 0.1 and 1.5 (given $\Sigma(r) = \Sigma_0(r/{\rm au})^{-p}$), we obtain disc winds in the range of 0.2–2.4 au from the central protostar. Observations vary on their predictions for where these winds exist, however a number of studies agree on a value between $\sim$ 0.3–5 au (Bacciotti et al. 2002; Anderson et al. 2003; Ray et al. 2007). On the other hand, theoretical predictions give values between 0.2 and 10 au (Ferreira et al. 2006; Pudritz et al. 2007; Turner et al. 2014). Hence our numerical models are consistent with independent theoretical constraints and with observations. However,

this does not mean that these are the only wind-driving regions in the disc. Other regions may exist for different relevant parameters.

We find that increasing the inner accretion rate $\dot{M}_{\rm in}$ while leaving the midplane ratio of the Alfvén speed to the sound speed (a_0) and the surface density profile unchanged, moves the disc wind region inwards. Similarly, increasing a_0 independent of the other parameters has the same effect. On the other hand, increasing the overall surface density via Σ_0 (see equation 2.18) moves the disc wind outwards. Decreasing the power-law index of the surface density p widens the extent of the disc wind.

We also find that the ejection/accretion ratios ($\dot{M}_{\rm out}/\dot{M}_{\rm in}$, see Cabrit 2007) of our disc wind models are in the range 10^{-1}–10^{-7} for the parameter combinations investigated here. We regard these values to be upper limits for realistic wind-launching regions, given our assumptions for the mass loading constraint derived in Section 2.3.3. For this constraint we assume that the angular momentum contained by the magnetic field is transferred back into the flow on a length scale $z \approx r$ above the disc midplane. In practice this could occur at even greater heights, which would increase the radial range of the intermediate magnetically-inactive region and hence decrease the ejection/accretion ratios in our models. The range of $\dot{M}_{\rm out}/\dot{M}_{\rm in}$ we find agrees closely with the 1.5D predictions of WK93 and Pelletier & Pudritz (1992), who calculate values for $\dot{M}_{\rm out}/\dot{M}_{\rm in}$ between 10^{-1} and 10^{-5}. Observational estimates of $\dot{M}_{\rm out}/\dot{M}_{\rm in}$ also overlap our results, with values between 10^{-1} and 10^{-4} (Cabrit 2007; Ellerbroek et al. 2013; Watson et al. 2016). From our findings, $\dot{M}_{\rm out}/\dot{M}_{\rm in}$ generally increases as $\dot{M}_{\rm in}$ and a_0 decrease, while the opposite is true for Σ_0 and the power-law index p. However, each of these trends is altered significantly by excessive mass loading of the field lines at intermediate radii, causing the fluid configuration in this region to be ineffective for wind launching (see Section 2.6.1 and Fig. 2.6). This leads to a steady decrease in $\dot{M}_{\rm out}/\dot{M}_{\rm in}$ with each parameter as the magnetically inactive region widens.

2.7.2. Comparison with current global simulations

Many studies have been performed using the shearing box approximation to investigate disc structure and wind launching in protostellar discs (e.g. Suzuki & Inutsuka 2009; Suzuki et al. 2010; Fromang et al. 2013; Bai & Stone 2013a,b; Lesur et al. 2013; Simon et al. 2013; Bai 2014). Compared to the 1+1.5D model used in this paper, the shearing box approximation has a few advantages. Due to its 3D nature, the shearing box approximation is able to model turbulence and other time-dependent properties such as disc evolution and chemical mixing much more

thoroughly than our 1+1.5D method. However, when it comes to radial properties and outflow rates, the shearing box approximation is severely limited by its boundary conditions (see Turner et al. 2014). Hence, while both types of models have unique advantages, quasi-global 2.5 or 3D time-dependent models such as Gressel et al. (2015), with higher resolution are needed to make progress.

Comparing our results to the quasi-global model of Gressel et al. (2015), we find quite different results between the two. Their model is time-dependent, includes ambipolar and Ohm diffusivities, and is initialized with a weak magnetic field ($\beta_0 = 10^{\sim 5-7}$), while our model is steady-state, includes Hall diffusion as well as ambipolar and Ohm, and maintains a much stronger magnetic field ($\beta_0 = 10^{\sim 0-1}$).

The weak magnetic field configuration of Gressel et al. (2015) leads to a laminar region about the disc midplane, with minimal accretion and field-line bending . This is in stark contrast to our model, which displays much higher inner-disc accretion rates and field-line bending. Given that the study by Moll (2012) employs magnetic field strengths much closer to ours, resulting in a similar field configuration, we expect that the morphological difference between our model and that of Gressel et al. (2015) is related to the magnetic field strength threading the disc (see also the weakly coupled models of Wardle 1997).

With regard to the wind-launching region, Gressel et al. (2015) find winds launched continuously along all radii within their simulation domain (0.5 - 5.5 au), while the winds produced by our models are limited to a narrow range, often marked with radial gaps where no wind is launched. This could again be related to the magnetic field strength within the disc, therefore, it would be beneficial for future global studies to focus on the intermediate plasma beta range ($\beta_0 = 10^{\sim 1-4}$), to observe how the field configuration, and accretion and outflow rates change between the weak regime, which is optimal for MRI growth, and the strong regime, which is optimal for centrifugal wind launching.

2.7.3. Implications

The significant results from this study are that disc winds tend to be radially localized, meaning that the majority of the wind output is centralized around a particular radius, and the discovery of a new class of disc winds containing an ineffective launching configuration at intermediate radii. The localization of wind output reinforces the applicability of deriving the launch radius of protostellar jets based on their poloidal velocities (e.g. Ferreira et al. 2006; Agra-Amboage

et al. 2011; White et al. 2014), while an ineffective or unstable launching region at intermediate radii could contribute to the knots we see in protostellar jets (e.g. Frank et al. 2014)

Variation of key disc parameters could represent the changing structure of the disc with time. For example, $\dot{M}_{\rm in}$ could change as a result of fluctuations during quiescent intervals, or steadily decline following an outburst event (Audard et al. 2014). In the case of a declining accretion rate, we expect the wind-launching region to shift to larger radii and the $\dot{M}_{\rm out}/\dot{M}_{\rm in}$ to increase, or in the case of a split wind, to decrease (see Fig. 2.6). Similarly, we expect Σ_0 to decrease over time due to mass accretion onto the central protostar (Williams & Cieza 2011; Armitage 2015), or vary on local scales as a result of accretion outbursts (Audard et al. 2014). From the results in Section 2.6.3, the disc wind would move inward as the disc mass is depleted, and $\dot{M}_{\rm out}/\dot{M}_{\rm in}$ would change accordingly.

2.7.4. Model limitations

We find that the radial extents and ejection/accretion ratios of the models presented in this paper are in good agreement with observations for our choice of disc parameters. The range of $\dot{M}_{\rm in}$ found to launch viable disc winds is relatively high compared with those observed in Classical (Class II) T-Tauri discs ($\sim 10^{-8}\ M_\odot\ {\rm yr}^{-1}$, Shariff 2009). These accretion rates overlap those inferred for FU Orionis objects (FUors, 10^{-6}–$10^{-3}\ M_\odot\ {\rm yr}^{-1}$) and EX Lupi objects (EXors, 10^{-8}–$10^{-6}\ M_\odot\ {\rm yr}^{-1}$), classes of pre-main-sequence stars which exhibit episodic accretion over time-scales of several decades, or years, respectively (Aspin et al. 2010; Audard et al. 2014). Hence our models may be representative of discs in an accretion outburst phase. However, it is also likely that the assumption of constant field-matter coupling Λ with height, or equipartition magnetic fields ($a_0 \lesssim 1$), are a major contributor to the large accretion rates in our models. Discs with variable Λ and weaker coupling exhibit a markedly different structure, with lower accretion rates due to an inner magnetically dead zone (see Wardle 1997). If the constant-Λ condition is relaxed, Λ is expected to initially increase with height above the disc midplane as the column density (which shields the disc from ionizing radiation) diminishes, leading to larger ionization fractions. However, above a certain height this effect is countered by a rapid decrease in density, leading to a reduction in the field-matter coupling (see figure 7.5 of Königl & Salmeron 2011). This change in Λ with height can potentially lead to conditions at the surface of the disc which differ from the models presented in this study, and hence different wind properties. This is therefore the next logical step in our study, and is addressed in Chapter 3.

In addition to the constant-Λ approximation, all results contained in this paper assume that the magnetic field parameter a_0 (the ratio of the Alfvén speed to the sound speed at the disc midplane) does not change with radius. Assuming that the Alfvén speed scales as the Keplerian velocity, BP82 showed that a_0 is constant with radius for an ideal MHD self-similar disc. Therefore, this may be considered as an intuitive first approximation. We expect however, that in a realistic disc, a_0 would vary with radius. This could in theory be constrained by systematically conserving the vertically integrated angular momentum flux, in a similar approach to our treatment of the mass flux (see Section 2.4), however we have neglected this approach for the time being due to the added complexity.

We also neglect the radial drift of poloidal magnetic field lines (i.e. we assume that $\epsilon_B = 0$) in each of the 1.5D solutions that make up the 1+1.5D models. Employing a similar radially-localized model to the one used here, but specialized to the ambipolar diffusion limit, WK93 derived solutions for positive and negative values of ϵ_B and found that solutions with the same value of $(\epsilon - \epsilon_B)$ are qualitatively similar. We use this result to justify the selection of $\epsilon_B = 0$ in our models, as this should not significantly impact the generality of the results. For a full discussion of the $\epsilon_B = 0$ approximation, see Appendix A of KSW10.

The disc is also assumed to be vertically isothermal, and follows a radial profile as given by the MMSN model. The temperature may actually increase towards the surface, as a result of thermal decoupling of dust and gas, due to the low density. This would affect the conditions at the sonic point, and mass flux.

Finally, we assume that the charged species are exclusively ions and electrons. This is a reasonably valid approximation at late times in the discs' evolution when dust grains have settled to the midplane, and hence grains may be neglected when considering the disc structure at larger z (e.g. Dullemond & Dominik 2004, KSW10). Other accretion mechanisms, such as turbulence generated by the MRI, could in principle stir up the dust component to larger heights above the midplane, however, in the radial locations of the disc we explore in this paper ($\sim$ 0.2–2.4 au) the MRI is thought to have little to no influence due to turbulent quenching via the Hall effect (Turner et al. 2014). This being said, due to the flexibility of the conductivity tensor formulation in each of our models, we could in principle extend our results to include the influence of dust grains on disc wind morphology (Wardle & Ng 1999).

2.8. Summary and conclusions

In this paper we investigated the properties of disc winds and how they vary with the characteristics of the underlying disc. Using the first 1+1.5D steady-state disc wind model incorporating all three diffusion mechanisms (Ohm, Hall, and ambipolar) and the effects of X-rays, cosmic rays, and radioactive decay, we determined how the radial extent and ejection/accretion ratio ($\dot{M}_{\rm out}/\dot{M}_{\rm in}$) of the wind-launching region varies with accretion rate $\dot{M}_{\rm in}$, magnetic field strength (parametrized by $a_0 \equiv v_{\rm A0}/c_{\rm s}$), and surface density profile given by $\Sigma(r) = \Sigma_0(r/{\rm au})^{-p}$. Each of these parameters has a significant effect on the radial position and extent of the wind-launching region, and the ejection/accretion ratio $\dot{M}_{\rm out}/\dot{M}_{\rm in}$, while still confining them to within observational and theoretical estimates. In summary, we found that:

- All 1+1.5D wind solutions are radially localized (i.e. the wind mass flux peaks at a particular radius, and rapidly drops off on either side). At smaller radii, the wind attenuates as a result of decreased field-matter coupling, while at larger radii, magnetic compression of the disc combined with a higher disc surface results in a lower density wind and decreasing outflow rate.

- Many 1+1.5D wind solutions are split into two parts by an ineffective launching configuration at intermediate radii, where no wind is expected to exist due to excessive mass loading of the field lines. This inactive region has a substantial impact on the ejection/accretion ratio, leading to a lower $\dot{M}_{\rm out}/\dot{M}_{\rm in}$. More detailed simulations are required to determine the behaviour of the disc and wind in this region.

- Decreasing $\dot{M}_{\rm in}$ expands the radial extent of the wind-launching region while moving it to larger radii, and increases $\dot{M}_{\rm out}/\dot{M}_{\rm in}$ (ignoring the effects of the inactive region). This is a result of less magnetic field bending in the radial and azimuthal directions, and hence reduced magnetic compression of the disc.

- Similarly, lower values of a_0 lead to an expanded disc due to less magnetic pressure, extending the wind-launching region in both directions, and increasing $\dot{M}_{\rm out}/\dot{M}_{\rm in}$.

- Decreasing the surface density power-law constant Σ_0 has the opposite effect. At lower Σ_0 (representative of a lower mass disc), the disc wind is launched closer to the protostar and has a reduced radial extent as a result of the modification of the field-matter coupling profile. This reduction in the radial extent leads to lower values for $\dot{M}_{\rm out}/\dot{M}_{\rm in}$.

- Decreasing the surface density power-law index p has the effect of radially stretching the launching region, as the region of optimal field-neutral coupling in the disc widens. It also decreases $\dot{M}_{\rm out}/\dot{M}_{\rm in}$ in the process.

In conclusion, we find that changes in the physical properties of protostellar discs have an important impact on the position of the launching region and the power of disc winds. We do stress though, that real protostellar discs have a much more complex morphology, including stratified diffusion regimes, regions of magnetohydrodynamic turbulence, and dust grain populations which we have not taken into account. Thus, our study provides a first look at the 1+1.5D structure of disc winds, while more detailed investigations are required to make future progress.

Acknowledgements

We thank the anonymous referee for their thorough and constructive report, which improved the paper significantly. We also thank Mark Wardle for useful discussions. CAN acknowledges support by an Australian Postgraduate Award. CF gratefully acknowledges funding by the Australian Research Council's Discovery Projects (grant DP150104329 and DP170100603). CF thanks for high performance computing resources provided by the Leibniz Rechenzentrum and the Gauss Centre for Supercomputing (grants pr32lo, pr48pi and GCS Large-scale project 10391), the Partnership for Advanced Computing in Europe (PRACE grant pr89mu), the Australian National Computational Infrastructure (grant ek9), and the Pawsey Supercomputing Centre with funding from the Australian Government and the Government of Western Australia, in the framework of the National Computational Merit Allocation Scheme and the ANU Allocation Scheme. This research was supported by ARC grant No. DP120101792.

CHAPTER 3

Centrifugally driven winds from protostellar accretion discs - II. The effects of magnetic diffusion

This chapter has been submitted to The Monthly Notices of the Royal Astronomical Society as ***Nolan, C. A., Federrath, C., & Salmeron, R. 2019, MNRAS, submitted****, referenced as Nolan et al. (2019), and is currently under review. This chapter is not modified from the submitted version, except in the following respects:*

- *Section, figure, footnote, and table numbering, and general formatting, have been modified for consistency with the remainder of the thesis;*
- *Additional material has been added in accordance with the Examiners' constructive feedback;*
- *References to Nolan et al. (2017) have been changed to point to Chapter 2 of this thesis;*

The 1.5D vertical disc-wind model used in this chapter was provided in its original form by Dr Raquel Salmeron. This model was adapted into a 1+1.5D configuration by the candidate, including extensive additions to the structure and complexity of the 1.5D model itself. All subsequent simulations employing the 1.5D and 1+1.5D models were performed by the candidate.

Abstract

Magnetic fields play a key role in determining the structure of accretion discs and the discs' ability to launch outflows. Here we determine the impact of non-ideal magnetohydrodynamical (MHD) effects (Ohm, Hall, and ambipolar diffusion) on disc structure and the launching of disc winds. We employ numerical simulations that capture the magnetic coupling coefficients by computing the ionization fractions self-consistently (in the limit where grains have grown and/or settled). Comparing to previous, more simplified models with a similar midplane non-ideal MHD structure, we find that a self-consistent treatment of the non-ideal MHD effects greatly increases the field-matter coupling above the disc midplane. This results in increased magnetic field bending and compression of the disc, with non-ideal MHD dominating below one scaleheight and potentially at large elevations due to the drop in ion density. We find radial localization of disc winds as in previous models, however the increased field-matter coupling away from the midplane shifts the wind-launching region to smaller radii. We also recover a radially symmetric wind mass-loss profile, and a reduction in overall wind output by an order of magnitude compared to previous models. Our model agrees quantitatively with the broad component of forbidden line emission recently observed in protostellar systems. We conclude that non-ideal MHD plays a crucial role in regulating the structure of accretion discs and in the launching of disc winds.

3.1. Introduction

Protostellar discs are weakly ionized over much of their extent due to radiation shielding, rapid recombination processes (particularly in the presence of grains), cosmic ray shielding, and low temperatures (resulting in ineffective thermal ionization), and hence non-ideal MHD effects (e.g. magnetic diffusion) become significant (Gammie 1996). Accurate treatment of these effects are especially important for modelling protostellar disc winds, as the magnetic diffusion influences the configuration of the magnetic field lines within the disc, which has implications for the existence, structure, and mass outflow rate of the wind. It is therefore necessary to account for the complex ionization and recombination processes when calculating the diffusivity structure of the disc-wind system.

Non-ideal MHD effects can be classified into three general categories, depending on the neutral

density and magnetic field strength within the disc. *Ambipolar diffusion* dominates at relatively low densities and strong magnetic fields: near the surface of the disc at radii of < 10 au, and throughout the vertical column farther out (Königl et al. 2010). In this regime the magnetic field is well coupled to the ionized component, and effectively drifts with it through the neutrals. At higher densities (close to the disc midplane at 'intermediate' radii, 1–10 au, e.g. Li 1996; Wardle 1999; Sano & Stone 2002; Salmeron & Wardle 2005), the disc is dominated by the *Hall regime*. The magnetic field is still well coupled to the electrons, but increased collisions result in decoupling from the ions. At even higher densities (in the most shielded inner radii of discs, 0.1–1 au) all charged species are uncoupled from the magnetic field (Wardle 2007). This is known as the *Ohm regime*.

In the last decade, these three non-ideal MHD effects have become increasingly important in the modelling of disc winds (see Turner et al. 2014, for a recent review). Due to the complex nature of non-ideal MHD, initial simulations employed self-similar (e.g. Li 1995; Ferreira & Pelletier 1995; Li 1996; Ferreira 1997) or radially-localized, semi-analytic (e.g. Wardle & Königl 1993; Königl et al. 2010; Salmeron et al. 2011) approximations. More recent simulations, utilizing the shearing box approximation (e.g. Suzuki & Inutsuka 2009; Suzuki et al. 2010; Bai & Stone 2013a,b; Fromang et al. 2013; Lesur et al. 2013; Simon et al. 2013; Bai 2014; Lesur et al. 2014; Bai 2015), have allowed for the investigation of alternatives to disc winds in the removal of angular momentum (i.e. the magneto-rotational instability, MRI; Balbus & Hawley 1991; Balbus & Hawley 1998).

The aforementioned simulations have revealed many interesting details regarding the vertical structure of protostellar discs. However, few studies to date have combined non-ideal MHD with a more extended domain to study both the vertical and radial structure of discs and disc winds. Dzyurkevich et al. (2010) was the first to achieve this using a time-independent Ohmic diffusivity, in the context of particle trapping via the MRI. Building upon this, Gressel et al. (2015) included ambipolar diffusion, finding that disc winds are a natural result of global disc models. More recently, Béthune et al. (2017) and Bai (2017) have incorporated the full tensor formulation with all three non-ideal MHD terms, and find that Hall diffusion has a substantial disruptive effect on the wind, depending on the direction of the initial vertical magnetic field.

While global simulations are very effective in their ability to investigate the kinematics and dynamics of outflows, local semi-analytical models of discs are still important in their own right. They are generally numerically cheaper to run, allowing for large parameter studies, and have less overall complexity while still including realistic physics. This aids in the disentangling of complex

relationships between competing forces in the disc and wind. In recent years, semi-analytical models have been used in modelling the vertical structure of outflows (e.g. Jacquemin-Ide et al. 2019), and investigating magnetic flux transport (e.g. Leung & Ogilvie 2019), hydrodynamical instabilities (Pfeil & Klahr 2019), and dust transport in outflows (Giacalone et al. 2019).

In Chapter 2, we developed a new approach for modelling the structure of protostellar disc winds, including a simplified treatment of the non-ideal MHD terms. This approach combines a series of radially-localized, vertical 1.5D solutions of the type developed by Wardle & Königl (1993), Königl et al. (2010), and Salmeron et al. (2011), in order to create a radially extended 1+1.5D model in (r, z) coordinates. These studies assume that the diffusivity terms scale as ρ/B^2, where ρ is the gas density and B is the magnetic field strength, resulting in a constant magnetic coupling parameter. We used these simulations to investigate how the radial location, extent, and mass-loss rate of disc winds vary with different parameters; specifically the mass accretion rate, the strength of the magnetic field threading the disc, and the surface density profile.

In this companion paper, we remove the simplifications to the modelling of non-ideal MHD used in Chapter 2, whilst still assuming that grains have settled to the disc midplane, and that the disc is vertically isothermal: in Chapter 2, as with earlier works (Wardle & Königl 1993; Königl et al. 2010; Salmeron et al. 2011), the conductivity components are scaled with the gas density ρ and magnetic field strength B, as ρ/B^2, in order to reduce the stiffness of the differential equations. In this study we remove this simplification, instead calculating the conductivity components self-consistently at all heights above the disc midplane. This allows the disc structure to reflect the vertical layering of non-ideal MHD regimes expected within protostellar discs (Königl & Salmeron 2011). We find that adding a more accurate magnetic diffusion profile results in increased radial magnetic field bending and compression of the disc due to stronger coupling between the field and the neutral gas in the region surrounding the midplane. This leads to a number of modifications to the structure of the wind-launching region.

We summarize our methodology in Section 3.2, followed by an analysis of the self-consistent 1+1.5D model in Section 3.3. We then compare this model with current observational and theoretical studies in Section 3.4, followed by our conclusions in Section 3.5.

3.2. Method

We describe the details of the 1+1.5D models in Sections 2.2–2.4 of Chapter 2. Here we summarize the main points and refer the reader to Chapter 2 for more information. The main difference to Chapter 2 is the new and updated modelling of the non-ideal MHD and ionization, which we describe in detail in Sections 3.2.4 and 3.2.5.

The 1+1.5D disc wind model is constructed from a series of 1.5D radially-localized, axisymmetric disc wind solutions. Each 1.5D solution is the result of integrating a set of six ordinary differential equations (ODEs) in the normalized vertical coordinate $\tilde{z} = z/h_{\rm T}$, from the disc midplane up to the sonic point $\tilde{z}_{\rm s} = z_{\rm s}/h_{\rm T}$. The disc tidal scaleheight $h_{\rm T}$ is defined by

$$h_{\rm T} \equiv c_{\rm s} r / v_{\rm K}, \tag{3.1}$$

where $c_{\rm s}$ is the vertically isothermal sound speed, r is the radius, and $v_{\rm K}$ is the Keplerian velocity. Each solution is defined by four parameters: the midplane plasma beta β_0, midplane temperature T_0, surface density Σ, and local mass accretion rate $\dot{M}_{\rm acc}$. The 1.5D solutions are connected together radially using mass conservation to form a 1+1.5D model of the wind-launching region in (r,z)-coordinates[1].

3.2.1. Physical Constraints

The radial extent of the wind-launching model is limited by four physical constraints, which are described in detail in Chapter 2. We also ignore regions of the disc where the wind mass-loss rate is negligible. The constraints are summarized as follows:

(i) *Sub-Keplerian flow*: The flow remains sub-Keplerian within the disc, which is expected as the ions lag behind the neutrals in the disc, creating azimuthal drag.

(ii) *Wind launching*: A wind is launched from the disc surface. As shown by Blandford & Payne (1982) in the ideal-MHD limit, a minimum inclination angle is required between the surface magnetic field and the rotation axis to launch a wind.

(iii) *Mass loading*: Only the upper layers of the disc are involved in launching a wind.

[1] As mentioned in Chapter 2, conservation of the vertically integrated angular momentum flux has been neglected in this study due to the added complexity.

(iv) *Energy conservation*: The rate of heating by Joule dissipation at the mid-plane does not exceed the rate of gravitational potential energy released at that location (Königl 1997).

For the numerical solutions, we also apply a criterion to identify the 'edge' of the wind-launching region. In practical terms, this requires that the normalized density $\tilde{\rho} \equiv \rho/\rho_0$ (where ρ_0 is the midplane gas density) remains above 10^{-9} at the sonic point, which is indicative of a non-negligible wind mass-loss rate[2].

3.2.2. Disc parameters

We now summarize the four disc parameters.

(i) *Magnetic field strength*: In Chapter 2 we characterize the magnetic field strength in the disc using the ratio of the Alfvén speed to the isothermal sound speed a_0 ($\equiv v_{A0}/c_s$), where the subscript 0 denotes midplane values. In this paper however, we adopt the more widely used ratio of the thermal to magnetic pressures β_0 (related to a_0 via $\beta_0 = 2/a_0^2$), in order to make our results more readily comparable to other studies. We assume that β_0 is constant for the radial extent of the wind-launching region, and consider only strong magnetic fields ($\beta_0 \sim 1$) in order to compare with the models presented in Chapter 2[3].

(ii) *Temperature*: Similar to Chapter 2, we assume a vertically isothermal disc, with a radial temperature profile corresponding to the minimum mass solar nebula (MMSN) prescription (Hayashi 1981; Hayashi et al. 1985)

$$T(r) = T_0 \left(\frac{r}{1\,\mathrm{au}}\right)^{-q}, \tag{3.2}$$

for which $T_0 = 280$ K and $q = 0.5$.

(iii) *Surface density*: We adopt a radial surface density profile of the form

$$\Sigma(r) = \Sigma_0 \left(\frac{r}{1\,\mathrm{au}}\right)^{-p}, \tag{3.3}$$

which constrains the vertical density profile for each 1.5D model, given that

$$\Sigma(r) = 2\int_0^{z_s} \rho(r,z)\,\mathrm{d}z, \tag{3.4}$$

[2]The normalized sonic point density $\tilde{\rho}_s$ is equivalent to $\rho v_z/\rho_0 c_s$, the normalized vertical mass flux in the wind, where v_z is the vertical velocity (see Salmeron et al. 2011).

[3]It is worth noting that wind solutions that satisfy $\beta_0 \sim 1$ are stable to the fastest growing linear mode of the MRI (Wardle & Königl 1993), as this mode is larger than the disc scale height.

where ρ is the gas density and z_s is the sonic point. For all models in this paper we assume $\Sigma_0 = 630$ g cm^{-2} and $p = 1$, since a purely wind-driving disc is expected to be thinner and flatter than an MMSN disc (Combet & Ferreira 2008).

(iv) *Mass accretion rate*: The 'local' mass accretion rate is defined by

$$\dot{M}_{\rm acc}(r) = -2\pi r \int_{-z_{\rm b}}^{z_{\rm b}} \rho v_{\rm r}\, {\rm d}z, \tag{3.5}$$

where $z_{\rm b}$ is the height at which the azimuthal velocity becomes super-Keplerian (the base of the wind). $\dot{M}_{\rm acc}$ is set at the innermost radius of the wind-launching region $r_{\rm in}$,

$$\dot{M}_{\rm in} = \dot{M}_{\rm acc}(r_{\rm in}), \tag{3.6}$$

while at all other radii it is derived using the law of mass conservation. This is covered in the following section.

3.2.3. Constructing the 1+1.5D disc model

The first step in calculating the 1+1.5D model is to find the innermost radius of the wind-launching region $r_{\rm in}$ that satisfies the imposed disc parameters while still remaining physically viable. Once we obtain $r_{\rm in}$ and its corresponding 1.5D solution, we calculate subsequent solutions at logarithmically increasing radii defined by

$$r_{\rm i+1} = 10^{1/k} r_{\rm i}, \tag{3.7}$$

or

$$\Delta r_{\rm i} = r_{\rm i+1} - r_{\rm i} = (10^{1/k} - 1) r_{\rm i}, \tag{3.8}$$

where k is the number of 1.5D solutions within one decade of radius. Each new 1.5D solution satisfies the prescribed β_0, $T_0(r_{\rm i+1})$, $\Sigma(r_{\rm i+1})$, and $\dot{M}_{\rm acc}(r_{\rm i+1})$, where $\dot{M}_{\rm acc}(r_{\rm i+1})$ is calculated by adding the wind flux in the interval $[r_i, r_{\rm i} + \Delta r_{\rm i}]$ to the local accretion rate at r_i,

$$\begin{aligned}
\dot{M}_{\rm acc}(r_{\rm i+1}) &= \dot{M}_{\rm acc}(r_{\rm i}) + \dot{M}_{\rm wind}(r_{\rm i}) - \dot{M}_{\rm wind}(r_{\rm i+1}) \\
&= \dot{M}_{\rm acc}(r_{\rm i}) + 4\pi \int_{r_{\rm i}}^{r_{\rm i+1}} r'\, \rho_{\rm b}(r') v_{\rm zb}(r') {\rm d}r' \\
&\simeq \dot{M}_{\rm acc}(r_{\rm i}) + 4\pi r_{\rm i} \rho_{\rm b}(r_{\rm i}) v_{\rm zb}(r_{\rm i}) \Delta r_{\rm i},
\end{aligned} \tag{3.9}$$

in order to satisfy mass conservation. The wind mass-loss rate in equation (3.9) is defined by (e.g. Kuncic & Bicknell 2004)

$$\dot{M}_{\rm wind}(r) = 4\pi \int_{r}^{\infty} r' \rho_{\rm b} v_{\rm zb} {\rm d}r', \tag{3.10}$$

where ρ_b and v_{zb} are the density and vertical velocity at the disc surface/base of the wind (z_b) respectively. We continue calculating new 1.5D solutions at greater radii until they either violate one of the four physical constraints defined in Section 3.2.1, or the normalized sonic point density $\tilde{\rho}_s$ drops below 10^{-9}, indicating a negligible wind mass-loss rate. The radius of the outermost valid solution then defines the outer radius of the wind-launching region r_{out}. Finally, we define the cumulative wind mass-loss rate over the entire wind-launching region as

$$\dot{M}_{out} = \dot{M}_{wind}(r_{in}). \tag{3.11}$$

3.2.4. Modelling of non-ideal MHD

In Chapter 2 we adopted the simplification of Königl et al. (2010) and Salmeron et al. (2011), in which the total field-matter coupling, represented by the dimensionless Elsasser number Λ_T, is fixed with height. We achieve this by scaling the Ohm, Hall, and Pedersen conductivity components (σ_O, σ_H, and σ_P, respectively) with the gas density ρ and magnetic field strength B, as ρ/B^2. This simplification greatly reduces the stiffness of the differential equations and allowed us to obtain stable numerical solutions faster. However, a constant Λ_T with height is unrealistic. As noted by Königl & Salmeron (2011), Λ_T generally scales with ρ_i/ρ and ρ_i in the Hall and ambipolar regimes respectively – where ρ_i is the ion density. Thus Λ_T is expected to increase with height above the midplane as the gas becomes progressively more ionized and the density decreases. It then peaks and subsequently drops as ρ_i decreases in the wind region.

In this study we remove the simplification of scaled conductivity components, instead calculating each conductivity term self-consistently at all heights above the disc midplane, using the ionization model described in Section 3.2.5 below. This results in more realistic field-matter coupling and diffusivity profiles. However, it also greatly increases the stiffness of the ODEs, requiring modifications to the methodology to solve the equations. In Chapter 2 we use a shooting method to solve for the vertical structure of the disc. Integrating from one end of the solution domain, we iterate on the single free variable (in this case the normalized vertical velocity at the disc midplane $\tilde{v}_{z0}$) until boundary conditions at both ends of the domain are satisfied. However, due to the increased stiffness of the ODEs resulting from calculating the conductivity components self-consistently, we require quadruple numerical precision and numerous iteration steps to span the domain and reach the sonic point. This significantly increases the computational time required for each model ($\gtrsim 250$ times compared to the models computed in Chapter 2). In order to compute models with the new methodology in a reasonable time-frame, we choose a radial

resolution of $k = 100$ (see equation 3.7). This is less than the convergent resolution calculated in Appendix A of Chapter 2 ($k = 1000$), however, according to the resolution study we expect the qualitative results to remain unchanged, and the quantitative results are converged to within ~ 15 per cent.

3.2.5. Updated ionization Model

As stated in the previous section, the 1+1.5D model described in Chapter 2 adopts a simplified prescription for the non-ideal MHD terms, in which the Elsasser number is calculated only at the disc midplane and then fixed with height by scaling the conductivity components. As a consequence, the ionization model presented in Appendix C of Chapter 2 is only applicable to the disc midplane. The updated methodology presented in this paper requires ionization rates throughout the disc vertical column, in order to calculate the conductivity components self-consistently, hence we now detail the full 2D ionization model.

In this model, we include the contributions of cosmic rays, X-rays, and the radioactivity of nuclides to determine the total ionization rate

$$\zeta = \zeta_{\rm CR} + \zeta_{\rm XR} + \zeta_{\rm R}. \tag{3.12}$$

We calculate the cosmic ray contribution according to the model outlined in Salmeron & Wardle (2005):

$$\zeta_{\rm CR}(r,z) = \frac{\zeta_{\rm CR}}{2}\left\{\exp\left[-\frac{\Sigma(r,z)}{\lambda_{\rm CR}}\right] + \exp\left[-\frac{\Sigma(r)-\Sigma(r,z)}{\lambda_{\rm CR}}\right]\right\}, \tag{3.13}$$

where $\zeta_{\rm CR} = 10^{-17}$ s^{-1} is the ionization rate due to cosmic rays in the interstellar medium and $\lambda_{\rm CR} = 96$ g cm^{-2} is the attenuation length for cosmic rays. Also, $\Sigma(r)$ is the surface density at radius r defined by equation (3.4), while

$$\Sigma(r,z) = \int_z^{z_{\rm s}} \rho(r,z){\rm d}z \tag{3.14}$$

is the column density from the point (r,z) up to the sonic point $z_{\rm s}$. The two exponentials in equation (3.13) represent the ionization rate at (r,z) due to cosmic rays coming from above and below the disc respectively.

Stellar X-rays have a much smaller attenuation length than cosmic rays, and therefore only contribute to the ionization of the disc surface layers (Igea & Glassgold 1999; Ádámkovics et al. 2011). We calculate the X-ray ionization rate using the Bai & Goodman (2009) fit to the Monte

Carlo radiative transfer simulations of Igea & Glassgold (1999), assuming a dominant X-ray photon energy of $T_X = 3$ keV,

$$\begin{aligned}\zeta_{\rm XR}(r,z) &= \frac{L_{\rm X}}{10^{29}\ {\rm erg\ s^{-1}}}\left(\frac{r}{1\ {\rm au}}\right)^{-2.2} \\ &\times\left(\zeta_1\left[\exp^{-\left(\frac{\Sigma(r,z)}{\lambda_{\rm XR1}}\right)^{\alpha}}+\exp^{-\left(\frac{\Sigma(r)-\Sigma(r,z)}{\lambda_{\rm XR1}}\right)^{\alpha}}\right]\right. \\ &\left.+\zeta_2\left[\exp^{-\left(\frac{\Sigma(r,z)}{\lambda_{\rm XR2}}\right)^{\beta}}+\exp^{-\left(\frac{\Sigma(r)-\Sigma(r,z)}{\lambda_{\rm XR2}}\right)^{\beta}}\right]\right).\end{aligned} \tag{3.15}$$

Included in this fit are contributions from direct and scattered X-rays, with intensities of $\zeta_1 = 6.0\times10^{-12}$ s^{-1} and $\zeta_2 = 1.0\times10^{-15}$ s^{-1}, and attenuation lengths of $\lambda_{\rm XR1} = 3.5\times10^{-3}$ g cm^{-2} and $\lambda_{\rm XR2} = 1.6$ g cm^{-2} respectively (Bai & Goodman 2009). The exponents are $\alpha = 0.4$ and $\beta = 0.65$, while we assume that the X-ray luminosity of the protostar is $L_{\rm X} = 1.0\times10^{29}$ erg s^{-1}.

We assume that the ionization rate associated with the decay of radioactive components within the disc is dominated by potassium (^{40}K)[4], and estimate it in terms of the fraction of heavy metal elements in the gas phase δ_2 and the abundance of dust grains relative to that of molecular clouds $f_{\rm g}$:

$$\zeta_{\rm R} = 6.9\times10^{-23}\left[\delta_2 + (1-\delta_2)f_{\rm g}\right]\ {\rm s^{-1}} \tag{3.16}$$

(Umebayashi & Nakano 1981, 1990), where $\delta_2 = 0.02$. In this study we set $f_{\rm g}$ to zero following the assumption that dust grains have settled to the disc midplane (Sano et al. 2000)[5].

Assuming that grains have settled out and that the electron (and ion) density is determined by the equilibrium ionization balance equation – in the limit where the dominant recombination mechanism is the radiative recombination of metal ions (Fromang et al. 2002; Salmeron & Wardle 2003) – the electron (and ion) density is given by

$$n_{\rm e,i} = \left(\frac{\zeta\rho}{1.4 m_{\rm H}\alpha}\right)^{\frac{1}{2}}, \tag{3.17}$$

[4]While ^{26}Al has a much higher ionizing potential compared to ^{40}K (Consolmagno & Jokipii 1978), it has a very short half-life (7×10^5 yrs), and hence is not considered in our calculations.

[5]While large grains almost certainly settle to the midplane early on, small grains may exist in the upper layers of the disc throughout all stages of disc evolution, playing a substantial role in determining the coupling of the gas to the magnetic field. They take much longer to settle than larger grains due to their strong coupling to the gas (Pinte et al. 2008), and can be stirred up via turbulence and winds (e.g. Giacalone et al. 2019). It is also expected that small grains are replenished in the disc upper layers by small fragments from shattering collisions between dust grains (Dullemond & Dominik 2005; Birnstiel et al. 2009; Zsom et al. 2011) or by continuous infall (e.g. Mizuno et al. 1988; Dominik & Dullemond 2008).

where m_H is the hydrogen nucleus mass and $\alpha = 3 \times 10^{-11} T^{-1/2}$ cm^3 s^{-1} is the radiative recombination rate for metal ions (e.g. Salmeron & Wardle 2005).

Following the definition of the electron density, we can now calculate the Ohm, Hall, and ambipolar diffusion coefficients, given by

$$\eta_O = \frac{c^2 m_e \gamma_e \rho}{4\pi e^2 n_e}, \tag{3.18}$$

$$\eta_H = \frac{cB}{4\pi e n_e}, \tag{3.19}$$

and

$$\eta_A = \frac{B^2}{4\pi m_i \gamma_i \rho n_i} \tag{3.20}$$

respectively (e.g. Wardle & Salmeron 2012). Here c is the speed of light, e is the charge of an electron, $m_i = 30 m_H$ is the ion mass, and m_e is the electron mass. Also, in equations (3.18) and (3.20),

$$\gamma_j = \frac{\langle \sigma v \rangle_j}{m_j + m}, \tag{3.21}$$

where $m = 2.33 m_H$ and $\langle \sigma v \rangle_j$ is the rate coefficient for collisional momentum transfer between charged species j and the neutrals. We use the following results of Draine et al. (1983) for the rate coefficients:

$$\langle \sigma v \rangle_i = 1.6 \times 10^{-9} \text{ cm}^3 \text{ s}^{-1} \tag{3.22}$$

and

$$\langle \sigma v \rangle_e \approx (1 \times 10^{-15} \text{ cm}^2) \left(\frac{128 k_B T}{9\pi m_e} \right)^{1/2}, \tag{3.23}$$

where k_B is Boltzmann's constant.

Finally, we compute the Elsasser numbers

$$\begin{aligned} \Lambda_0 &= \frac{1}{\tilde{\eta}_O}; \qquad \Lambda_H = \frac{1}{\tilde{\eta}_H}; \qquad \Lambda_A = \frac{1}{\tilde{\eta}_A}; \\ \Lambda_T &= \frac{1}{\sqrt{\tilde{\eta}_H^2 + (\tilde{\eta}_A + \tilde{\eta}_O)^2}}, \end{aligned} \tag{3.24}$$

which measure the amount of coupling between the magnetic field and the neutral gas, where the normalization factor for the diffusion coefficients is

$$\tilde{\eta} = \frac{\eta}{v_A^2 / \Omega_K}, \tag{3.25}$$

and Ω_K is the Keplerian angular velocity.

Table 3.1 List of models presented in this paper, including their radial extents ($r_{\rm in}$ and $r_{\rm out}$) and ejection/accretion ratio ($\dot{M}_{\rm out}/\dot{M}_{\rm in}$).

Simulation name	Methodology	$\dot{M}_{\rm in}$ [$\rm M_\odot\ yr^{-1}$]	$r_{\rm in}$ [au]	$r_{\rm out}$ [au]	$\dot{M}_{\rm out}/\dot{M}_{\rm in}$
VCD	Vertically-Constant Diffusivity Model	1.6×10^{-5}	0.56	0.93	3.5×10^{-2}
SCD	Self-Consistent Diffusivity Model	1.6×10^{-5}	0.22	0.60	2.8×10^{-3}

3.3. Results

In Section 2.5, we examined two wind-launching disc models in detail, one with a 'weak' wind ($\dot{M}_{\rm out}/\dot{M}_{\rm in} = 1.3\times10^{-2}$) and the other with a 'strong' wind ($\dot{M}_{\rm out}/\dot{M}_{\rm in} = 3.5\times10^{-2}$). In this paper, we recalculate the 'strong-wind' model using the updated method outlined in Section 3.2. We then compare it with the original model from Chapter 2 and examine the differences in structure. We designate the original model by VCD (vertically-constant diffusivity), and the updated model by SCD (self-consistent diffusivity) for the remainder of the paper. Both models are characterized by a midplane plasma beta $\beta_0 = 2$, a surface density profile $\Sigma(r) = 630\,(r/\rm au)^{-1}\,g\,cm^{-2}$, and a mass accretion rate of $\dot{M}_{\rm in} = 1.6\times10^{-5}\,\rm M_\odot\,yr^{-1}$. Key outputs for both models are shown in Table 3.1.

3.3.1. Vertical structure

Fig. 3.1 displays poloidal maps of the density and field-matter coupling for the VCD and SCD models. The top row shows the density, velocity, and magnetic field morphology of the two models: both models show evidence of the layered wind structure described by Königl & Salmeron (2011). In the region surrounding the disc midplane ($|z| < z_{\rm h}$, where $z_{\rm h}$ is the magnetically reduced density scaleheight) gas pressure dominates magnetic pressure, with the majority of accretion and field bending occurring here. Higher up ($z_{\rm h} < |z| < z_{\rm b}$), the disc becomes magnetically dominated and the accretion flow transitions to a centrifugally-driven wind. Above the disc surface ($z > z_{\rm b}$), the wind becomes super-Keplerian ($v_\phi > v_{\rm K}$) and continues to accelerate up to the sonic surface $z_{\rm s}$, where the model terminates.

The strength of the magnetic-to-gas coupling in the VCD and SCD models, in terms of the total ($\Lambda_{\rm T}$), Ohmic (Λ_0), Hall ($\Lambda_{\rm H}$), and ambipolar ($\Lambda_{\rm A}$) Elsasser numbers are shown in rows two

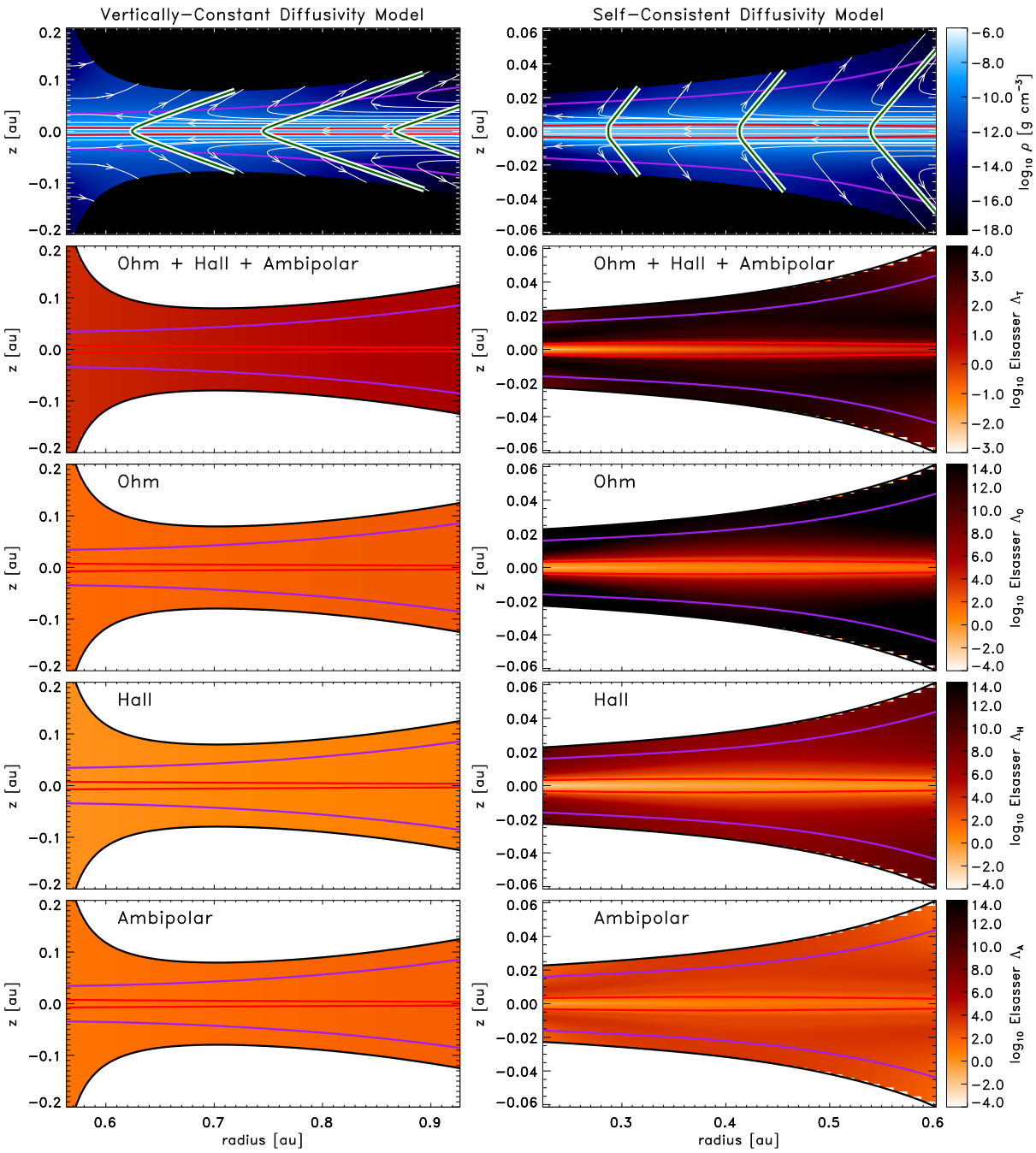

Figure 3.1 2D slices of the gas density (top panels), and the total, Ohm, Hall, and ambipolar Elsasser numbers (Λ_T, Λ_0, Λ_H, and Λ_A respectively) in the r-z plane, for the vertically-constant (left-hand panels) and self-consistent (right-hand panels) diffusivity models. The density contour plot is overlaid with white streamlines representing the velocity field, while the green lines with white outline show the magnetic field structure. The red lines represent the magnetically reduced density scaleheight z_h, and the purple lines signify the surface of the disc z_b, defined as the height at which the azimuthal velocity of the gas transitions from sub-Keplerian ($z < z_b$) to super-Keplerian ($z > z_b$). Black lines indicate the sonic surface z_s. Note: the horizontal and vertical scales of the VCD and SCD models are different; see Fig. 3.4 for a spatial comparison between the two models.

to five of Fig. 3.1 respectively (expressions for these parameters can be found in Section 3.2.5). As expected, the VCD model in the left-hand column of Fig. 3.1 preserves the field-matter coupling calculated at the midplane all the way up to the sonic point z_s, due to the adopted scaling of the conductivity terms with height (see Section 3.2.4). This is equivalent to the vertical perpetuation of the midplane diffusivity regime: in the VCD model the entire radial extent of the disc midplane is contained within the Hall diffusivity regime, and hence the whole vertical domain is dominated by Hall diffusion, resulting in a misalignment between the velocity and magnetic field vectors in the wind-launching region above the disc.

As shown in the SCD model in the right-hand column of Fig. 3.1, the field-matter coupling in a more realistic scenario is expected to increase rapidly with height due to the stronger irradiation of the outer layers by penetration of cosmic rays, X-rays, and generally higher temperatures (e.g. Königl & Salmeron 2011)[6]. As a consequence, the diffusivity regime transitions from Hall dominated at the midplane, through the ambipolar regime, and into the ideal MHD regime higher up, which we see in closer detail in Fig. 3.2. The Hall regime dominates the disc in the SCD model up to $\sim 2\,z_h$[7]. Above this point the disc transitions to the ambipolar regime, however since $\Lambda_T > 10$ for $|z| > z_h$, the disc is predominantly governed by ideal MHD. The combined field-neutral coupling Λ_T increases away from the disc midplane, peaking in the layer where ambipolar-diffusion becomes the dominant non-ideal MHD term.

The rapid increase in field-matter coupling away from the disc midplane in the SCD model also leads to another important effect. As shown by Wardle & Königl (1993) for the ambipolar diffusion limit, in the hydrostatic (negligible vertical velocity) approximation, the radial and azimuthal field bending near the midplane can be described by

$$\frac{\mathrm{d}b_r}{\mathrm{d}\tilde{z}} \approx \frac{\epsilon\beta_0\Lambda_{A0}}{2}; \qquad \frac{\mathrm{d}b_\phi}{\mathrm{d}\tilde{z}} \approx -\frac{\epsilon\beta_0}{4}, \tag{3.26}$$

where b_r and b_ϕ are the normalized radial and azimuthal magnetic field strengths ($b_i = B_i/B_z$), respectively, and $\epsilon = -v_r/c_s$ is the normalized inward radial velocity, i.e., the radial Mach number. Using the equations in Königl et al. (2010), it is straightforward to show that equation (3.26) also holds in the Hall diffusion limit. Similarly, Königl et al. (2010) showed that in the Hall limit,

[6] However, the drop in density with height may cause the coupling to decrease again near the disc surface (see Fig. 3.2 in this study, and fig. 4 of Salmeron & Wardle 2005). Also, while temperature effects are not included in the present formulation, penetration of ionizing radiation should still rapidly increase the field-matter coupling.

[7] Given that the Elsasser numbers are proportional to the inverse of their corresponding diffusion coefficient, the lowest Elsasser number defines the dominant diffusion regime in that region.

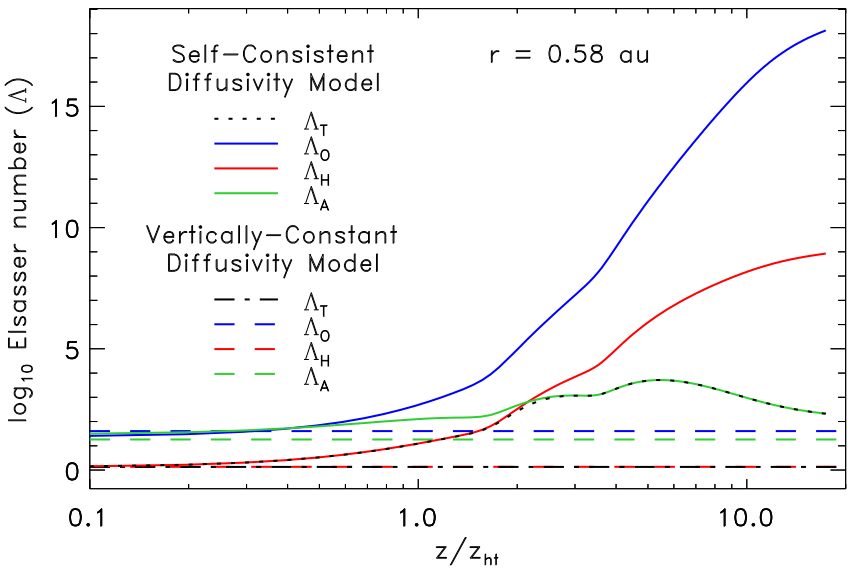

Figure 3.2 Total (Λ_T) and regime specific (Λ_0, Λ_H, Λ_A) Elsasser numbers as a function of height above the disc midplane, normalized by the density scaleheight z_h, for the vertically-constant (dash/dash-dot) and self-consistent (solid/dot) diffusivity models, at a radius of 0.58 au – the central radius in the overlap region of the two models.

for $\Lambda_H > 1/2$, the ratio of the density scaleheight to the tidal scaleheight (a good indicator of magnetic compression) is:

$$\frac{z_h}{h_T} \approx \frac{1}{\epsilon \beta_0^{1/2}} \left(\frac{1}{\Lambda_{A0}} + \frac{1}{\Lambda_{O0}} \right), \tag{3.27}$$

while the ratio of the height of the disc surface to the density scaleheight (a good indicator of the relative density at the disc surface) is:

$$\frac{z_b}{z_h} \approx \frac{\epsilon^2}{3\sqrt{2}} \left(\frac{1}{\Lambda_{A0}} + \frac{1}{\Lambda_{O0}} \right)^{-2}. \tag{3.28}$$

From these equations, we expect that for similar ϵ and β_0, and stronger field-matter coupling near the midplane, the radial field bending will be enhanced while the azimuthal bending will remain approximately the same (equation 3.26). Similarly, magnetic compression of the disc will increase (equation 3.27), and the wind will be more tenuous (equation 3.28). These predictions are shown to hold when comparing the density and magnetic field structure of the VCD and SCD models in Fig. 3.3, with z_b/z_h (equation 3.28) taking on values of 4.9 and 12.5 for the VCD and SCD models respectively.

3.3.2. Radial structure

Fig. 3.4 illustrates the 2D spatial extents and overlap of the VCD and SCD models. The 1+1.5D solution space is bounded by the sonic surfaces (z_s) in the vertical direction, and by negligible

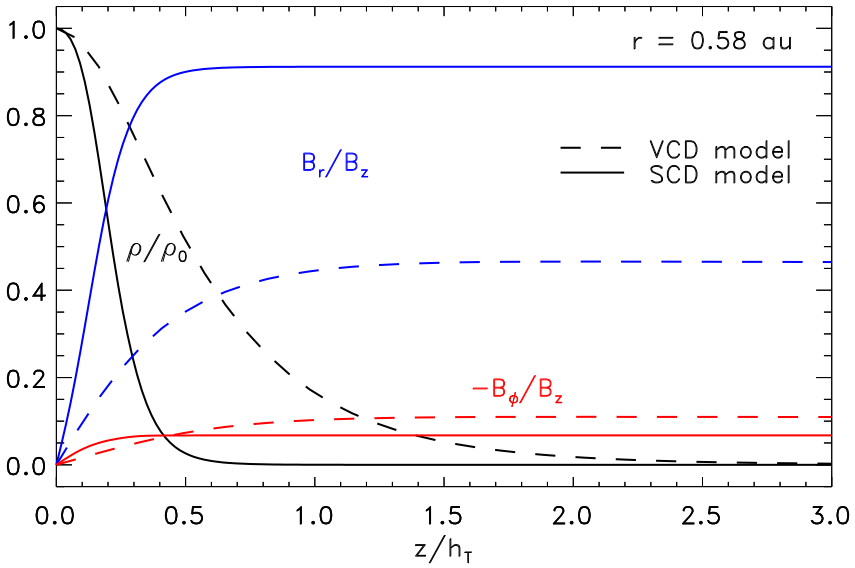

Figure 3.3 Normalized density $\tilde{\rho}$ (black) and magnetic field components b_r (blue) and b_ϕ (red) as a function of height above the disc midplane, normalized by the tidal scaleheight h_T, for the vertically-constant (dashed) and self-consistent (solid) diffusivity models, at a radius of 0.58 au – the central radius in the overlap region of the two models.

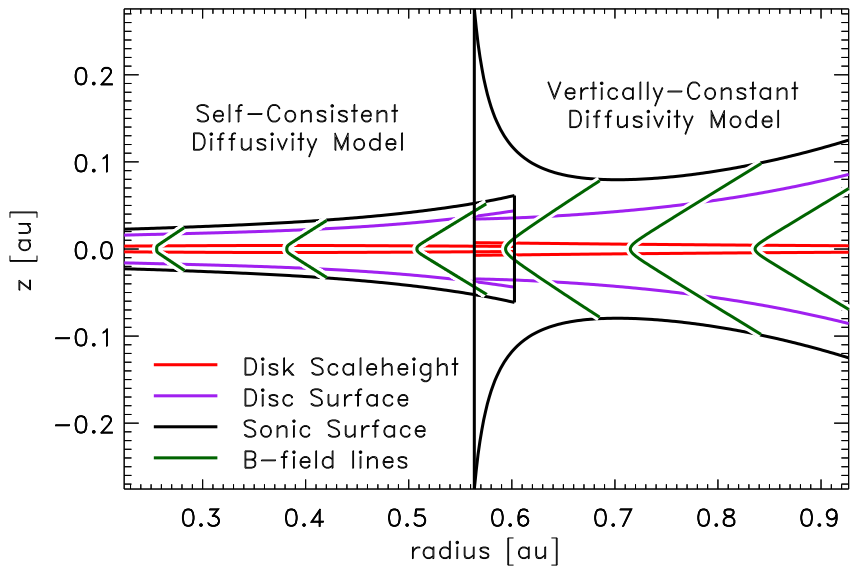

Figure 3.4 Two-dimensional spatial extent of the vertically-constant diffusivity (VCD) model and the self-consistent diffusivity (SCD) model. Red lines represent the disc scaleheight z_h, while purple lines represent the surface of the disc z_b, defined as the height at which the azimuthal velocity of the gas becomes super-Keplerian. The black lines indicate the sonic surface z_s, and hence the vertical extent of the 1+1.5D models.

wind mass-loss rates at the inner and outer radius for both the VCD and SCD models, as a result of $\tilde{\rho}_s$ dropping below 10^{-9} (see Section 3.2.1). The wind-launching region for the VCD model extends from ~ 0.56 to 0.93 au, while being shifted to smaller radii (~ 0.22 to 0.60 au) in the SCD model. The sonic surface is also modified, with the flaring of the sonic surface near the inner edge of the VCD model no longer present in the SCD model. We discuss these features in detail in the following paragraphs.

The radial extent of the wind-launching region is determined by a number of factors, including the magnetic field strength and the amount of coupling between the magnetic field and the gas. In Section 2.5.3, we outlined two mechanisms that localize the wind mass-loss rate in the radial direction, one working at smaller radii and one at larger radii. At smaller radii, decreased field-matter coupling at the midplane leads to less field bending away from the rotation axis and hence less centrifugal torque on the disc material (equation 3.26). This results in attenuation of the mass-loss rate until $\tilde{\rho}_s < 10^{-9}$, where the model is discontinued (see Section 3.2.1). At larger radii the field-matter coupling is stronger, leading to greater field bending (equation 3.26), increased magnetic compression of the disc (equation 3.27), and a lower gas density at the disc surface (equation 3.28). This, combined with a rising disc surface, causes the disc wind density to decrease rapidly and the mass-loss rate to become negligible (which again leads to $\tilde{\rho}_s$ dropping below 10^{-9}). These two mechanisms still apply in the updated SCD model, however the disc structure changes significantly when the diffusivities are calculated self-consistently, shifting the radii where they operate (see Fig. 3.4).

As shown in Section 3.3.1, a self-consistent diffusivity leads to stronger magnetic field-neutral coupling in the region above the disc midplane. This leads to enhanced radial field bending at any single radius via equation (3.26). Similarly, field-matter coupling increases with radius as the column density of the disc declines, and therefore so does B_r/B_z via equation (3.26). These two results combined with the assumption that the wind ceases below a similar magnetic field opening angle $\theta_s = \tan^{-1}(B_{rs}/B_{zs})$ for both models, where B_{rs} and B_{zs} are the radial and azimuthal components of the magnetic field at the sonic point respectively, indicates that the inner edge of the wind-launching region should move radially inwards. Given that the outer edge of the wind-launching region also depends upon B_r/B_z through disc compression, an overall increase in field-neutral coupling above the disc midplane causes the wind-launching region to move to smaller radii, as shown in Fig. 3.4.

As briefly described by Chapter 2, the flaring of the sonic surface in the VCD model is a direct

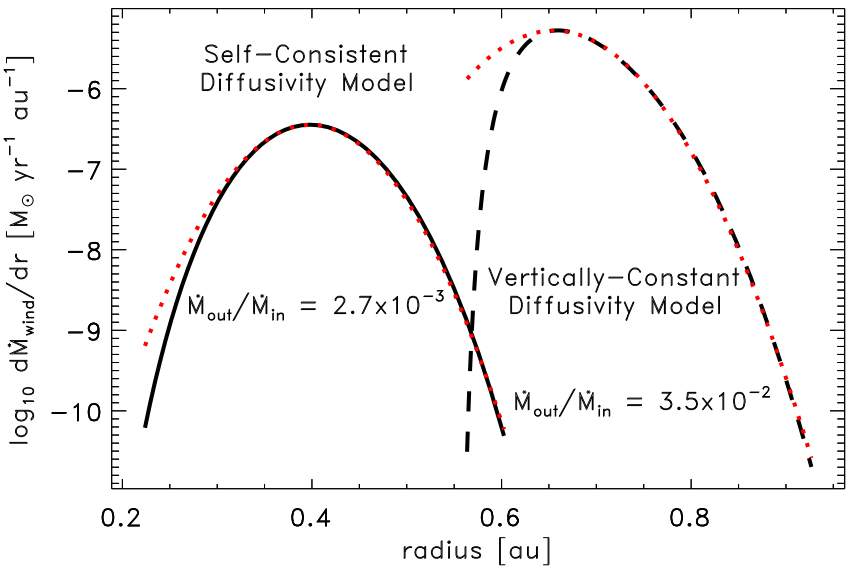

Figure 3.5 Wind mass-loss rate per unit radius $\mathrm{d}\dot{M}_{\rm wind}/\mathrm{d}r$ as a function of radius for the VCD (dashed line) and SCD (solid line) models. Gaussian fits to both profiles are shown by red dotted lines, with the fit for the VCD model only fitted to data points with radii greater than the peak position.

result of the simplified treatment of the non-ideal MHD terms. In the VCD model, the field-matter coupling at all heights above the disc is assigned the same value as that of the disc midplane. Given that $\Lambda_{\rm T}$ at the midplane is expected to decrease towards smaller r due to additional radiation shielding, the value of $\Lambda_{\rm T}$ at the sonic point will correspondingly decrease nearer to the star. Weaker field-matter coupling results in a smaller vertical Lorentz force accelerating the wind above the disc surface, and a correspondingly higher sonic point. The SCD model, with its superior treatment of the non-ideal MHD terms does not have this limitation and so does not exhibit flaring of the sonic surface at inner radii.

3.3.3. Accretion structure

Taking the radial derivative of equation (3.10), we arrive at the wind mass-loss rate per unit radius:

$$\frac{\mathrm{d}}{\mathrm{d}r}\dot{M}_{\rm wind} = 4\pi r \rho_{\rm b} v_{\rm zb}. \tag{3.29}$$

Fig. 3.5 displays $\mathrm{d}\dot{M}_{\rm wind}/\mathrm{d}r$ as a function of radius for the VCD and SCD models. While the mass accretion rate through the inner boundary of both models is set to $\dot{M}_{\rm in} = 1.6 \times 10^{-5}\,\mathrm{M}_\odot\,\mathrm{yr}^{-1}$, the resulting radial wind mass-loss profiles differ substantially. The VCD model has a total bipolar-wind mass-loss rate of $\dot{M}_{\rm out} = 5.6 \times 10^{-7}\,\mathrm{M}_\odot\,\mathrm{yr}^{-1}$, resulting in an ejection/accretion ratio $\dot{M}_{\rm out}/\dot{M}_{\rm in} = 3.5\times10^{-2}$. The updated SCD model has a mass-loss rate of $\dot{M}_{\rm out} = 4.4\times10^{-8}\,\mathrm{M}_\odot\,\mathrm{yr}^{-1}$,

corresponding to an ejection/accretion ratio of $\dot{M}_{\rm out}/\dot{M}_{\rm in} = 2.7 \times 10^{-3}$: an order of magnitude smaller. As with the radial shift explained in Section 3.3.2, the order of magnitude drop in ejection/accretion ratio between the two models can be attributed to the differences in field-matter coupling above the disc midplane. Increased field-matter coupling leads to a more compressed disc (equation 3.27) and lower gas density at the disc surface (equation 3.28). Hence, while increased field-matter coupling around the disc midplane shifts the wind-launching region to smaller radii, it also reduces the mass-loss rate of the wind by lowering the wind density.

It is also worth noting that the radial profile of $\mathrm{d}\dot{M}_{\rm wind}/\mathrm{d}r$ for the SCD model is more radially symmetric than in the VCD model, having a Gaussian-like shape centred at ~ 0.4 au, with a standard deviation of ~ 0.05 au. In contrast, the VCD profile is only Gaussian at radii exterior to the peak in mass-loss rate (see Fig. 3.5). As explained in Section 3.3.2, the inner region of the VCD model is modified by the reduced field-matter coupling in the entire disc section at smaller radii, which may contribute to explaining the abrupt drop in wind activity at small radii in these types of models (see Fig. 3.5). Hence, at least for grain-free winds in the strong-field regime (represented by the SCD model), we should expect a Gaussian-like radial wind profile.

3.4. Discussion

Lubow et al. (1994) and Cao & Spruit (2002) have suggested that winds of the type represented by our 1+1.5D model could be inherently unstable. They attributed this instability to the sensitive dependence of the wind mass flux on the inclination of the magnetic field at the disc surface (θ_s, where $\tan\theta_s = B_{r,s}/B_z$) according to the following feedback loop:

$$
\begin{aligned}
\text{increased } |v_r| \quad &\rightarrow \quad \text{increased } \tan\theta_s \\
&\rightarrow \quad \text{decreased sonic point } z_{\rm s} \\
&\rightarrow \quad \text{higher mass loading and } \dot{M}_{\rm wind} \\
&\rightarrow \quad \text{larger angular momentum removal} \\
&\rightarrow \quad |v_r| \text{ increases further ...}
\end{aligned}
$$

However, this process is based on an approximation to the disc vertical equilibrium. As pointed out by Ferreira (2007), what actually occurs is as $\tan\theta_s$ increases, the magnetic field produces a strong vertical compression of the disc, so that less material is ejected instead of more (see also Königl 2004). Salmeron et al. (2011) showed that as $|v_r|$ increases, the disc surface and $z_{\rm s}$ increase while $z_{\rm h}$ decreases due to magnetic compression of the disc. This situation is also observed in

our models: when moving outwards in radius, $\tan\theta_s$ increases as a result of greater field-matter coupling via equation (3.26). This leads to increased magnetic compression of the disc as we move outwards (equation 3.27), which combined with a growing disc surface and z_s results in a rapid attenuation of mass loading in the wind. These are key processes resulting from the physics of non-ideal MHD.

3.4.1. Split winds in forbidden lines

Early studies of large samples of T-Tauri stars, conducted by Hamann (1994), Hartigan et al. (1995), and Hirth et al. (1997) established that forbidden lines in protostars are characterized by two distinct components: a high-velocity component (HVC) and a low velocity component (LVC). The HVC is associated with shock-excited collimated jets, while the LVC is connected to a more extended disc wind. More recently, the studies of Rigliaco et al. (2013) and Simon et al. (2016) have deconvolved the LVC into a broad component (LVC-BC) and a narrow component (LVC-NC). The BC is associated with the inner regions of the disc (~0.05–0.5 au), while the NC appears to originate farther out (0.5–5 au). Additionally, Fang et al. (2018) was able to measure the wind loss rates for both components, discovering that the mass-loss rate from the BC is at least 5 times larger than the NC, and is likely at least as large as the HVC, if not much larger. This picture is compatible with our findings of a radially localized region for the launching of a centrifugally-driven disc wind, represented by the LVC-BC, at least in the production of winds with moderate to large mass-loss rates. The shifting of the wind-launching region to smaller radii with the introduction of self-consistent magnetic diffusivity calculations in this paper also moves our models into the radial footprint for the BC (i.e. ~0.05–0.5 au). However, quantitative comparisons need to be treated carefully, as future upgrades to our models could refine the radial extent (e.g. realistic vertical temperature profile and inclusion of dust grains, see Section 3.4.4).

The NC observed in forbidden lines is thought to be associated with another region of magneto-centrifugal wind launching at larger radii than the BC. Recent work by Banzatti et al. (2019) has discovered a tight kinematic connection between the BC and NC, indicating a common origin. If the NC represents a second region of magneto-centrifugal wind launching, the split wind configurations found in Chapter 2 for a range of parameter combinations could potentially explain this. These wind models are divided into two separate launching regions containing an intermediate region where wind launching is ineffective as a steady state solution, due to

excessive mass loading of the field lines[8]. This 'inactive region' occurs at the point where the local wind mass-loss rate would be the highest, which, if the wind mass-loss profile is symmetrical according to our findings in this paper (see Fig. 3.5), indicates that the integrated mass-loss rates from inner (BC) and outer (NC) active wind regions should be similar. However, given the significant changes to the shape of the wind mass-loss profile found by upgrading the calculation of the diffusivities in this paper, we expect that including dust grains, etc. would similarly modify the radial wind mass-loss rate profile. Hence further investigation into the launching regions of magnetic winds is required in order to understand the combined origin of the BC and NC.

3.4.2. Radially localized versus extended winds

While forbidden line emission observations may tentatively match the split wind configurations found in a number of our models, recent ALMA observations have added considerable detail to our understanding of the structure of outflows. High-resolution maps of molecular outflows in the millimetre and sub-millimetre range have revealed rotation (Aso et al. 2015; Bjerkeli et al. 2016; Hirota et al. 2017; Tabone et al. 2017; Louvet et al. 2018; Zhang et al. 2018), inferring extraction of a considerable amount of angular momentum from the underlying discs. Most important to our study, these observations infer wind launching across a large range of radii (0.5–25 au, e.g. Bjerkeli et al. 2016; Hirota et al. 2017; Lee et al. 2018; Louvet et al. 2018; Zhang et al. 2018). These revisions to our understanding of disc winds also match recent global simulations including non-ideal MHD effects, which manifest extended winds out to 10–20 au (e.g. Gressel et al. 2015; Béthune et al. 2017; Bai 2017).

Extended winds observed by ALMA and global simulations call into question the relatively narrow localized winds we calculate in this paper, however this is most likely due to a fundamental difference in disc parameters. The models presented in this paper employ midplane disc magnetizations near equipartition ($\beta_0 \simeq 1$) as is historically used for wind-driving simulations, while the simulations of Gressel et al. (2015), Béthune et al. (2017), and Bai (2017) use much lower magnetic field strength configurations ($\beta_0 \gg 1$). Historically, strong magnetic field strengths are required in order to launch magneto-centrifugal winds from discs, however recent studies (e.g. Bai 2017) have shown that winds can still launch from the disc, provided the disc magnetization is near equipartition at the disc surface. This allows for much weaker magnetizations at the disc

[8]While steady-state solutions are ineffective in this region, unstable launching configurations such as episodic outbursts cannot be ruled out.

midplane ($\beta_0 \approx 10^4$).

The difference in β_0 could potentially explain the differences in radial wind distribution seen between our 1+1.5D models and global models, given that the operation of the wind-launching mechanism is highly dependent on the magnetic field-neutral coupling. In a subsequent study, we will investigate these differences by modelling discs with $\beta_0 \gg 1$. Further work is required on both the observational and theoretical fronts to determine a more consistent picture of disc winds.

3.4.3. Implications for the planet-forming region

One of the fundamental implications of our model is that magneto-centrifugal winds are confined to a specific range of disc radii, depending on the conditions of the disc itself. If this is correct, and the wind is confined to the inner disc only ($\sim$ 0.2–3 au), it potentially leaves much of the planet forming region ($\sim$ 3–30 au) without a strong mechanism for the removal of angular momentum. Turbulence via the MRI was long believed to provide the required viscosity to mediate angular momentum removal and accretion. However, recent studies including non-ideal MHD effects have found that MRI-driven turbulence can be either reduced significantly (Simon et al. 2015) or quenched altogether (e.g. Bai & Stone 2013b; Lesur et al. 2014).

One possible answer to the problem of angular momentum transport outside the wind launching region is hydrodynamical turbulence (see Fromang & Lesur 2019, for a review). Discs are now thought to have very low magnetizations at the midplane ($\beta_0 \approx 10^4$), resulting in very little magnetic influence. This can give rise to a number of hydrodynamic instabilities, such as the vertical shear instability (Urpin 2003; Nelson et al. 2013; Lin & Youdin 2015), convective overstability (Klahr & Hubbard 2014), the 'zombie vortex' instability (Marcus et al. 2015; Lesur & Latter 2016), as well as turbulence driven by planets (Bae et al. 2016; Fung & Chiang 2017). These instabilities can in principle produce the required levels of viscosity for angular momentum transport in the inner disc. However, as is mentioned previously in this section, the disc parameters (specifically β_0 and $\dot{M}_{\rm acc}$) used in this paper differ substantially from that now expected for standard T Tauri discs, hence further studies must be performed at much higher beta ($\beta_0 \approx 10^4$) before any concrete claims can be made about the launching region and its implications for the outer planet-forming region.

It is worth noting here that we still see substantial accretion rates for low-wind 1D solutions at the inner and outer radial extents of the SCD model. This implies that significant vertical angular

momentum transport and accretion could still occur even for very weak winds, given the right conditions in the disc. Hence weak winds could potentially support accretion throughout the remainder of the planet-forming region. This possibility will be explored in subsequent studies.

3.4.4. Future improvements of the model

The upgrades to the 1+1.5D model presented in this paper successfully remove the most glaring of simplifications to the models of Königl et al. (2010), Salmeron et al. (2011), and Chapter 2, that of vertically isotropic field-neutral coupling. Removing this approximation shifts the wind-launching region to lower radii, while decreasing the total wind mass-loss rate and making the radial distribution of mass loss more symmetrical. It also removes the flaring of the sonic point near the inner edge of the wind-launching region, a direct consequence of the simplified treatment of the non-ideal MHD terms.

Including a self-consistent vertical diffusivity profile enables us to model discs more accurately with much lower magnetic field strengths ($\beta_0 \gg 1$), which was not possible with the simplified formulation. High-β_0 discs are dominated by a laminar region surrounding the disc midplane with minimal accretion and field line bending. At the height at which β reaches equipartition, the magnetic fields see significant bending and it is here that the mass accretion occurs (see Königl & Salmeron 2011, Fig. 7, and also Gressel et al. 2015). In a future study we will model discs with a range of β_0, allowing us to look at how the wind morphology changes between regimes.

Subsequent improvements for the model will include upgrades to the vertical temperature profile and the inclusion of dust grains. Currently, the 1.5D solutions are vertically isothermal, however protoplanetary disc gas is heated by a number of sources, including X-rays, cosmic rays, stellar irradiation, and magnetic heating, while cooling occurs by radiative diffusion in the disc interior and according to its emissivity in the atmosphere. Heat is also exchanged between the gas and dust through collisions. Future models will include this complex structure, potentially giving us the ability to model both magneto-centrifugally driven and photo-evaporative winds.

We currently assume that dust grains have settled to the disc midplane, which is an acceptable zeroth-order assumption (see footnote 5 in Section 3.2.5). However, the inclusion of grains is important for understanding the impact of disc winds on planet formation. The presence of grains substantially increases the magnetic diffusion within the disc by soaking up electrons and ions from the gas phase, reducing the magnetic conductivity of the gas by many orders of magnitude (Wardle 2007). This in turn leads to poor coupling between the magnetic field and

the neutrals, and limits magnetic activity. In a future study we will incorporate grain physics into the calculations of the diffusion coefficients, using the latest estimates of protoplanetary dust populations, and see how this effects the wind structure at different stages of disc evolution.

3.5. Conclusions

In this paper we build on the results of Chapter 2, updating their simplified 1+1.5D magneto-centrifugally driven disc-wind model. We replace their assumption of vertically constant magnetic diffusivity terms with a self-consistent vertical diffusion profile, calculating the non-ideal MHD terms at each point by incorporating the effects of cosmic rays, X-rays, radioactive decay, and radiative recombination based on the local column density. We compare the upgraded model to that of Chapter 2, and examine the effects of non-ideal MHD on the vertical and radial structure of the wind launching region. In summary, we find that:

(**i**) The magnetic field-matter coupling above the disc midplane in the updated model is orders of magnitude larger than that of the original model, resulting in enhanced magnetic field bending, stronger magnetic compression of the disc, and a more tenuous wind.

(**ii**) The increased field-matter coupling also results in non-ideal MHD (namely Hall diffusion) dominating below one scaleheight and potentially at large elevations above the disc due to the drop in ion density, while ideal MHD governs the structure of the disc and wind nearer to and above the disc surface.

(**iii**) The solutions computed with the upgraded 1+1.5D model are also radially localized, as the ones observed in Chapter 2, however the self-consistent diffusivities lead to a shifting of the wind region to smaller radii. This occurs because the attenuation mechanisms controlling the radial localization of the wind are highly dependent on the field bending and field-matter coupling; at smaller radii the attenuation of the wind mass-loss rate is caused by less field bending due to decreased coupling, while at larger radii increased coupling leads to strong field bending, enhanced magnetic compression of the disc and negligible material available at the disc surface for the wind.

(**iv**) The radial profile of the wind mass-loss rate is much more symmetrical in the updated model, displaying an almost Gaussian shape. The total mass-loss rate across the wind-launching region, quantified by the ejection/accretion ratio, drops by roughly an order of

magnitude. This is due to the disc compression, which concentrates more material near the midplane and less near the disc surface where the wind is launched.

In conclusion, we find that a self-consistent treatment of the magnetic diffusion coefficients is crucial. We observe that the vertical and radial structure of the wind-launching region is highly influenced by internal and external ionization sources, and that detailed treatment of these factors is important for accurate modelling of disc-wind systems.

Acknowledgements

The authors would like to thank Mark Wardle for his in-depth and useful discussions. CAN acknowledges support by an Australian Postgraduate Award. C. F. acknowledges funding provided by the Australian Research Council (Discovery Projects DP170100603 and Future Fellowship FT180100495), and the Australia-Germany Joint Research Cooperation Scheme (UA-DAAD). We further acknowledge high-performance computing resources provided by the Leibniz Rechenzentrum and the Gauss Centre for Supercomputing (grants pr32lo, pr48pi and GCS Large-scale project 10391), the Partnership for Advanced Computing in Europe (PRACE grant pr89mu), the Australian National Computational Infrastructure (grant ek9), and the Pawsey Supercomputing Centre with funding from the Australian Government and the Government of Western Australia, in the framework of the National Computational Merit Allocation Scheme and the ANU Allocation Scheme.

CHAPTER 4

The density variance – Mach number relation in isothermal and non-isothermal adiabatic turbulence

This chapter has been published as ***Nolan, C. A., Federrath, C., & Sutherland, R. S. 2015, MNRAS, 451, 1380****, referenced as Nolan et al. (2015). This chapter is not modified from the published version, except in the following respects:*

- *Section, figure, footnote, and table numbering, and general formatting, have been modified for consistency with the remainder of the thesis;*

The original paper is available at `https://academic.oup.com/mnras/article/451/2/1380/987087`.

The Fyris Alpha shock-capturing code Sutherland (2010) used in this chapter was constructed by Dr Ralph Sutherland. The simulations performed using this code were conducted by the candidate.

The theoretical model included in this chapter was derived by Dr Christoph Federrath, and the section of the discussion that refers to this model was also written by Dr Federrath. The remainder of the paper was written by the candidate.

Abstract

The density variance–Mach number relation of the turbulent interstellar medium is relevant for theoretical models of the star formation rate, efficiency, and the initial mass function of stars. Here we use high-resolution hydrodynamical simulations with grid resolutions of up to 1024^3 cells to model compressible turbulence in a regime similar to the observed interstellar medium. We use Fyris Alpha, a shock-capturing code employing a high-order Godunov scheme to track large density variations induced by shocks. We investigate the robustness of the standard relation between the logarithmic density variance (σ_s^2) and the sonic Mach number ($\mathcal{M}$) of isothermal interstellar turbulence, in the non-isothermal regime. Specifically, we test ideal gases with diatomic molecular ($\gamma = 7/5$) and monatomic ($\gamma = 5/3$) adiabatic indices. A periodic cube of gas is stirred with purely solenoidal forcing at low wavenumbers, leading to a fully developed turbulent medium. We find that as the gas heats in adiabatic compressions, it evolves along the relationship in the density variance–Mach number plane, but deviates significantly from the standard expression for isothermal gases. Our main result is a new density variance–Mach number relation that takes the adiabatic index into account: $\sigma_s^2 = \ln\left(1 + b^2\mathcal{M}^{(5\gamma+1)/3}\right)$ and provides good fits for $b\mathcal{M} \lesssim 1$. A theoretical model based on the Rankine-Hugoniot shock jump conditions is derived, $\sigma_s^2 = \ln\{1 + (\gamma+1)b^2\mathcal{M}^2/[(\gamma-1)b^2\mathcal{M}^2 + 2]\}$, and provides good fits also for $b\mathcal{M} > 1$. We conclude that this new relation for adiabatic turbulence may introduce important corrections to the standard relation, if the gas is not isothermal ($\gamma \neq 1$).

4.1. Introduction

The interstellar medium (ISM) is a complex, turbulent, multi-phase gaseous medium, which permeates the space between stars in the galactic plane (Ferrière 2001). It is an essential part of the evolutionary cycle in stars, recycling the products of nucleosynthesis from dying stars and creating the stellar nurseries for a new generation of star formation (Elmegreen & Scalo 2004; Mac Low & Klessen 2004; McKee & Ostriker 2007; Krumholz 2014; Padoan et al. 2014). The ISM interacts with supernova explosions, protostellar jets, winds, and outflows, which shape its structure and drive the turbulence we observe via atomic and molecular line observations of the ISM.

In many simulations that include an ISM (e.g., Fischera & Dopita 2005; Bland-Hawthorn et al.

2007; Cooper et al. 2009; Wagner & Bicknell 2011), a statistical construction with isotropic properties related to turbulent statistics have been used, as a proxy for the turbulent ISM. Causal models of the turbulent ISM will drastically increase the accuracy of these models, but this first involves an in-depth study of the statistics and evolution of fully developed turbulence.

In purely isothermal gas, the probability density function (PDF) of the gas densities may be approximated by a lognormal distribution (Vázquez-Semadeni 1994), which in log-space has the form

$$p_{\mathrm{LN}}(s) = \frac{1}{\sqrt{2\pi\sigma_s^2}} \exp\left[-\frac{1}{2}\frac{(s-\bar{s})^2}{\sigma_s^2}\right], \tag{4.1}$$

where $s = \ln(\rho/\bar{\rho})$, and $\bar{s}$ and σ_s^2 are the mean and variance of the logarithm of the density ρ, scaled by the mean density, $\bar{\rho}$, respectively. The logarithmic density variance is a function of the root-mean-squared (rms) sonic Mach number ($\mathcal{M}$), and is given by

$$\sigma_s^2 = \ln\left(1 + b^2\mathcal{M}^2\right). \tag{4.2}$$

The coefficient b is known as the turbulence driving parameter and depends on the mode mixture induced by the turbulent forcing mechanism (Federrath et al. 2008b). Purely solenoidal (divergence-free) driving leads to $b = 1/3$, while purely compressive (curl-free) driving corresponds to $b = 1$.

Equation (4.2) has been studied extensively for isothermal gases (Padoan et al. 1997; Passot & Vázquez-Semadeni 1998; Kritsuk et al. 2007; Beetz et al. 2008; Federrath et al. 2008b; Price et al. 2011; Burkhart & Lazarian 2012; Konstandin et al. 2012; Seon 2012), with investigation into different simulation techniques (Price & Federrath 2010) and stirring methods (Federrath et al. 2008b, 2010). It has also been studied by employing a heating and cooling curve (Wada & Norman 2001; Kritsuk & Norman 2002; Audit & Hennebelle 2005; Hennebelle & Audit 2007; Audit & Hennebelle 2010; Seifried et al. 2011; Gazol & Kim 2013). Recently an investigation has been done in the magnetohydrodynamic (MHD) regime (Molina et al. 2012), and on polytropic gases (Federrath & Banerjee 2015).

In our work, we investigate the robustness of this well-established density variance–Mach number relation, equation (4.2), in the non-isothermal regime, specifically in ideal gases with diatomic molecular ($\gamma = 7/5$) and monatomic ($\gamma = 5/3$) adiabatic indices.

This is relevant because theoretical models of the star formation rate (Krumholz & McKee 2005; Hennebelle & Chabrier 2011; Padoan & Nordlund 2011; Federrath & Klessen 2012), the star formation law (Federrath 2013b), the star formation efficiency (Elmegreen 2008), and the initial

mass function of stars (Hennebelle & Chabrier 2008; Hopkins 2013a; Chabrier et al. 2014) heavily rely on equation (4.2).

Section 4.2 summarizes our simulation and analysis methods. Section 4.3 first presents results for the isothermal case, in order to make contact with previous studies and to verify our analysis techniques. Then we present a numerical resolution study to determine the minimum resolution required in order to measure the density variance – Mach number relation in simulations with $\gamma > 1$ and present our main results for adiabatic indices $\gamma = 7/5$ and $5/3$. We provide a theoretical model for the $\sigma_s^2(\mathcal{M})$ relation in Section 4.4 and discuss the discrepancies that we find compared to the standard equation (4.2). Section 4.5 summarizes our conclusions.

4.2. Simulation and analysis methods

To simulate the turbulent ISM we use the high-resolution, shock-capturing code Fyris Alpha (Sutherland 2010) to solve the equations of compressible hydrodynamics across a three-dimensional, periodic domain with side length $L = 1$, initial uniform density $\bar{\rho} = 1$, pressure of $1/2$ ($c_s^2 = \gamma/2$), and zero initial velocities. Unlike previous studies, the goal here is to test the density and velocity statistics of purely adiabatic turbulence with an ideal gas equation of state (EOS), rather than a purely isothermal or polytropic EOS, and simpler than employing a cooling curve or running chemohydrodynamical simulations (Glover et al. 2010). Ultimately, simulations with multiple species including all relevant chemical reactions, as well as radiative heating and cooling would be the most realistic, but their complexity might not allow us to reduce the results to some simple rules of thumb that can be used in practical applications. We thus simplify the problem significantly by studying the turbulence in purely adiabatic, ideal gases with the aim of extracting results that might be applicable to a wider range of cases, including terrestrial experiments and atmospheric turbulence, in addition to the ISM. Table 4.1 lists the key parameters of all our adiabatic turbulence simulations.

4.2.1. Ideal gas equation of state

The ideal gas EOS relates the pressure P, density ρ, and temperature T, and is given by

$$\frac{PV}{T} = Nk_\mathrm{B} \quad \text{or} \quad \frac{P}{\rho} = \frac{N}{m}k_\mathrm{B}T \quad \text{or} \quad P = nk_\mathrm{B}T, \tag{4.3}$$

Table 4.1 Simulation parameters. Column (1): simulation name; column (2): grid resolution; column (3): adiabatic exponent γ in equation (4.5); column (4): dimensionless driving amplitude of the turbulence; column (5): resulting time-averaged velocity dispersion in code units in the regime of fully developed turbulence; column (6): turbulent box crossing time: $t_{\rm cross} = L/\sigma_v$ in code units.

Simulation name	$N_{\rm res}^3$	γ	A	σ_v	$t_{\rm cross}$
(1)	(2)	(3)	(4)	(5)	(6)
(01) AD-TURB-256-A200-G1	256^3	1.0001	200	2.19 ± 0.14	0.46 ± 0.03
(02) AD-TURB-256-A400-G1	256^3	1.0001	400	3.38 ± 0.13	0.30 ± 0.01
(03) AD-TURB-256-A800-G1	256^3	1.0001	800	5.45 ± 0.29	0.18 ± 0.01
(04) AD-TURB-256-A1600-G1	256^3	1.0001	1600	8.62 ± 0.61	0.12 ± 0.01
(05) AD-TURB-256-A100-G7/5	256^3	7/5	100	1.53 ± 0.04	0.65 ± 0.02
(06) AD-TURB-256-A200-G7/5	256^3	7/5	200	2.47 ± 0.12	0.40 ± 0.02
(07) AD-TURB-256-A400-G7/5	256^3	7/5	400	4.00 ± 0.17	0.25 ± 0.01
(08) AD-TURB-1024-A200-G5/3	1024^3	5/3	200	2.51 ± 0.14	0.40 ± 0.02
(09) AD-TURB-512-A200-G5/3	512^3	5/3	200	2.50 ± 0.13	0.40 ± 0.02
(10) AD-TURB-256-A100-G5/3	256^3	5/3	100	1.55 ± 0.05	0.65 ± 0.02
(11) AD-TURB-256-A200-G5/3	256^3	5/3	200	2.55 ± 0.14	0.39 ± 0.02
(12) AD-TURB-256-A400-G5/3	256^3	5/3	400	4.07 ± 0.24	0.25 ± 0.01
(13) AD-TURB-128-A200-G5/3	128^3	5/3	200	2.47 ± 0.13	0.40 ± 0.02
(14) AD-TURB-64-A200-G5/3	64^3	5/3	200	2.45 ± 0.14	0.41 ± 0.02

with the volume V, the Boltzmann constant $k_{\rm B}$, the particle mass m, the total number of particles N, and the particle number density $n = N/V$. The ratio of the specific heat capacities at constant pressure and constant volume defines the adiabatic index:

$$\gamma = \frac{c_P}{c_V} = 1 + \frac{2}{f}, \tag{4.4}$$

where f denotes the number of degrees of freedom. For monatomic gas, $f = 3$ and $\gamma = 5/3$, while for diatomic molecular gas, $f = 5$ and $\gamma = 7/5$, because diatomic molecules have two rotational degrees of freedom in addition to the three translational degrees of freedom. Note that at typical molecular cloud temperatures (about 10–100 K), oscillatory degrees of freedom cannot

be excited by collisions, which is why–although theoretically present–they do not contribute to increase f in such cases. The specific internal energy of an ideal gas, $u = \frac{f}{2}\frac{N}{m}k_{\rm B}T$, is only determined by its temperature. Inserting this equation into equations (4.3) and (4.4), leads to

$$P(\rho, T) = (\gamma - 1)\rho u(T) \tag{4.5}$$

expressed via the adiabatic index γ, which serves as the EOS. In order to determine the statistics of turbulence in this adiabatic regime, we use isothermal, diatomic molecular, and monatomic equations of state ($\gamma \to 1, \gamma = 7/5$, and $5/3$, respectively).

Note that in order to model isothermal gases, γ is often set close to unity (e.g., $\gamma = 1.0001$), as if the gas had an extremely large number of degrees of freedom $f \to \infty$. This trick produces a gas that approximately stays at constant temperature, because any excess heat from dissipation (e.g., by shocks) is absorbed in such a big internal energy reservoir that the temperature of the gas does not notably change.

4.2.2. Driving of turbulence, time evolution, and definition of the Mach number

The driving of turbulence in the gas is performed by stirring with random purely solenoidal (divergence-free) forcing at low wavenumbers for the duration of the simulation. All wavenumbers k in the range $1 \leq k/(2\pi/L) \leq 3$ were driven. The driving pattern is evolved with an Ornstein-Uhlenbeck process similar to the methods explained in Eswaran & Pope (1988), Schmidt et al. (2009), and Federrath et al. (2010).

From the work done by Federrath et al. (2008b) and Federrath et al. (2010), we expect a proportionality constant of $b \sim 1/3$ in equation (4.2) for solenoidally driven isothermal gas and we will test that in both isothermal and adiabatic gases. The rms Mach number of the gas is modified by varying the stirring amplitude A of the driving force, allowing each γ to be tested at a range of Mach numbers.

All simulations are run for several turbulent box crossing times to test the density variance – Mach number relation in the regimes of transient as well as fully developed turbulence. The turbulent crossing time is defined as $t_{\rm cross} \equiv L/\sigma_v$, where σ_v is the asymptotic velocity dispersion. The velocity dispersion and hence the crossing time depend on the driving amplitude A. We show an example of this dependence in Fig. 4.1. We assume that the turbulence becomes fully developed after one crossing time in each simulation, indicated by the dashed vertical lines in Fig. 4.1. At this point the gas properties no longer vary drastically but change smoothly,

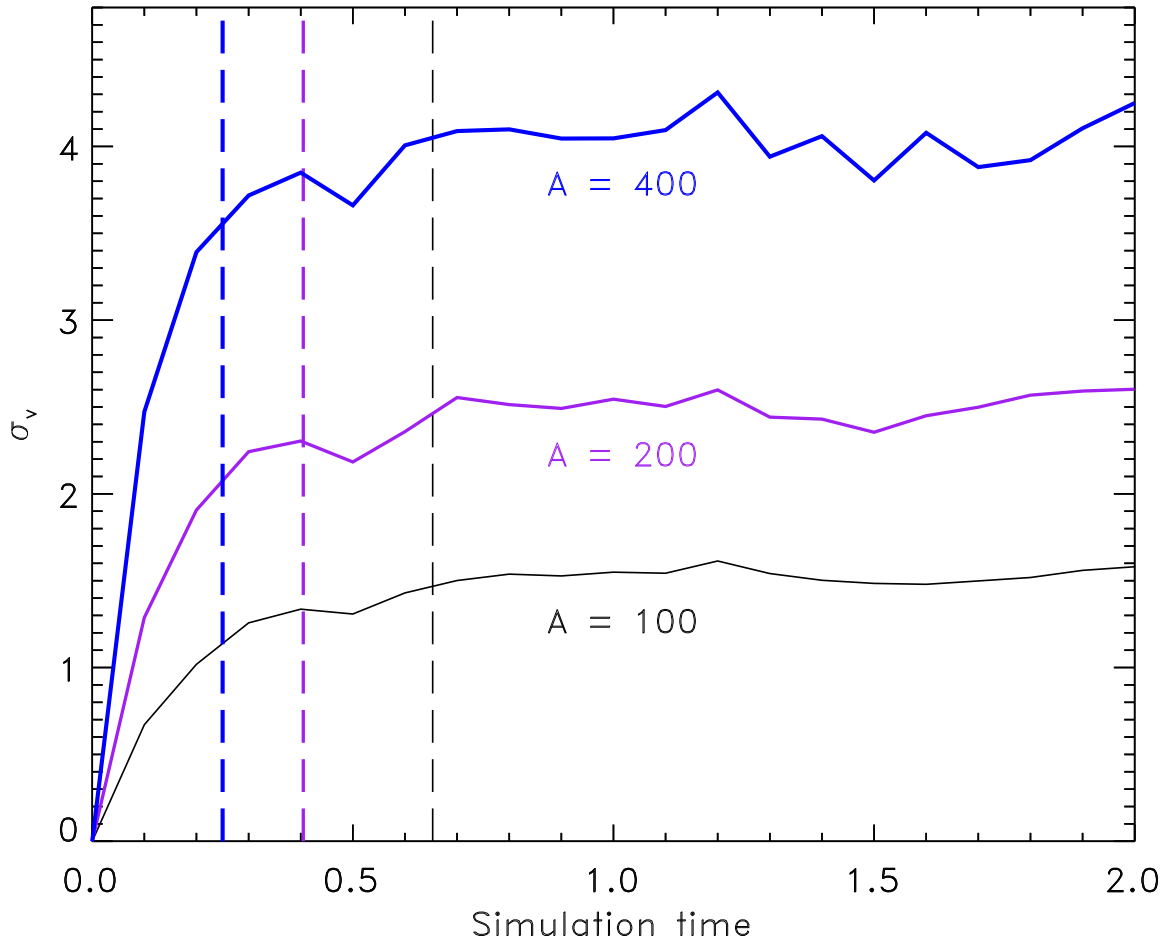

Figure 4.1 The velocity dispersion σ_v, as a function of simulation time for driving amplitudes $A = 100$, 200, and 400, and for fixed adiabatic $\gamma = 7/5$. The times for the onset of turbulence in each case are shown as vertical dashed lines and are approximated with the box crossing time $t_{\rm cross} = L/\sigma_v$, where L is the linear size of the computational domain. The box crossing time for each simulation is listed in Table 4.1.

indicating a statistically stable configuration. This allows us to distinguish regimes of transient ($t < t_{\rm cross}$) and fully developed ($t > t_{\rm cross}$) turbulence.

Given the velocity dispersion and sound speed $c_{\rm s} = (\partial P/\partial \rho)^{1/2}$, we have different Mach numbers $\mathcal{M} = \sigma_v/c_{\rm s}$, depending on the driving amplitude A and depending on the value of adiabatic γ. This is because the sound speed depends on the derivative of the EOS, equation (4.5). It furthermore depends on the simulation time, because the internal energy and thus the mean temperature of the gas keeps increasing during the course of the adiabatic simulations with $\gamma = 7/5$ and $\gamma = 5/3$. This is in stark contrast to the isothermal and polytropic simulations performed in previous studies (Padoan et al. 1997; Passot & Vázquez-Semadeni 1998; Federrath et al. 2008b; Price et al. 2011; Konstandin et al. 2012; Federrath & Banerjee 2015), where the sound

speed did not change systematically, after the turbulence was fully developed. Here, however, the total energy is conserved, which means that all dissipated energy is conservatively added to the internal energy. Thus, the injected energy from the driving is converted into internal energy and heats the gas continuously, leading to an ever increasing average sound speed and to a continuously decreasing rms Mach number. We thus use instantaneous measurements of $\mathcal{M}$ and σ_s in the following to determine the density variance–Mach number relation in adiabatic gases.

4.2.3. Measuring the density variance

The density variance of the gas is calculated using method 4 in section 2.3 of Price et al. (2011), but instead of fitting a lognormal distribution, we fit the more appropriate Hopkins (2013b) distribution. The advantage of the Hopkins fit is that it takes turbulent intermittency effects into account and provides excellent fits to the density PDFs over a wide range of physical parameters, including different Mach numbers, driving amplitudes, and mixtures (Federrath 2013a), as well as magnetic field strengths and variations in the polytropic exponent for simulations that employ a polytropic EOS (Federrath & Banerjee 2015). The Hopkins (2013b) density PDF is defined as

$$p_{\rm HK}(s) = I_1\left(2\sqrt{\lambda\,\omega(s)}\right)\exp\left[-\left(\lambda+\omega(s)\right)\right]\sqrt{\frac{\lambda}{\theta^2\,\omega(s)}}\,,$$
$$\lambda \equiv \sigma_s^2/(2\theta^2), \quad \omega(s) \equiv \lambda/(1+\theta) - s/\theta \;\; (\omega \geq 0), \tag{4.6}$$

where $I_1(x)$ is the modified Bessel function of the first kind. Equation (4.6) is motivated and explained in detail in Hopkins (2013b). It contains two parameters: (1) the volume-weighted standard deviation of logarithmic density fluctuations σ_s, and (2) the intermittency parameter θ. In the zero-intermittency limit ($\theta \to 0$), equation (4.6) becomes the lognormal distribution from equation (4.1), $p_{\rm HK} \to p_{\rm LN}$.

In order to measure the density variance σ_s^2, we fit our simulation density PDFs in a restricted range around the mean (from $\bar{s} - 3\sigma_{s,\rm mom}$ to $\bar{s} + 3\sigma_{s,\rm mom}$, where $\sigma_{s,\rm mom}$ is the second moment of the density distribution, directly computed by summation over all simulation data points) with equation (4.6) and determine the best-fitting parameter σ_s. In agreement with the conclusions drawn in Price et al. (2011) and Hopkins (2013b), we find that the fitted σ_s is the same within a few percent as $\sigma_{s,\rm mom}$ (computed by summation over all simulation grid cells).

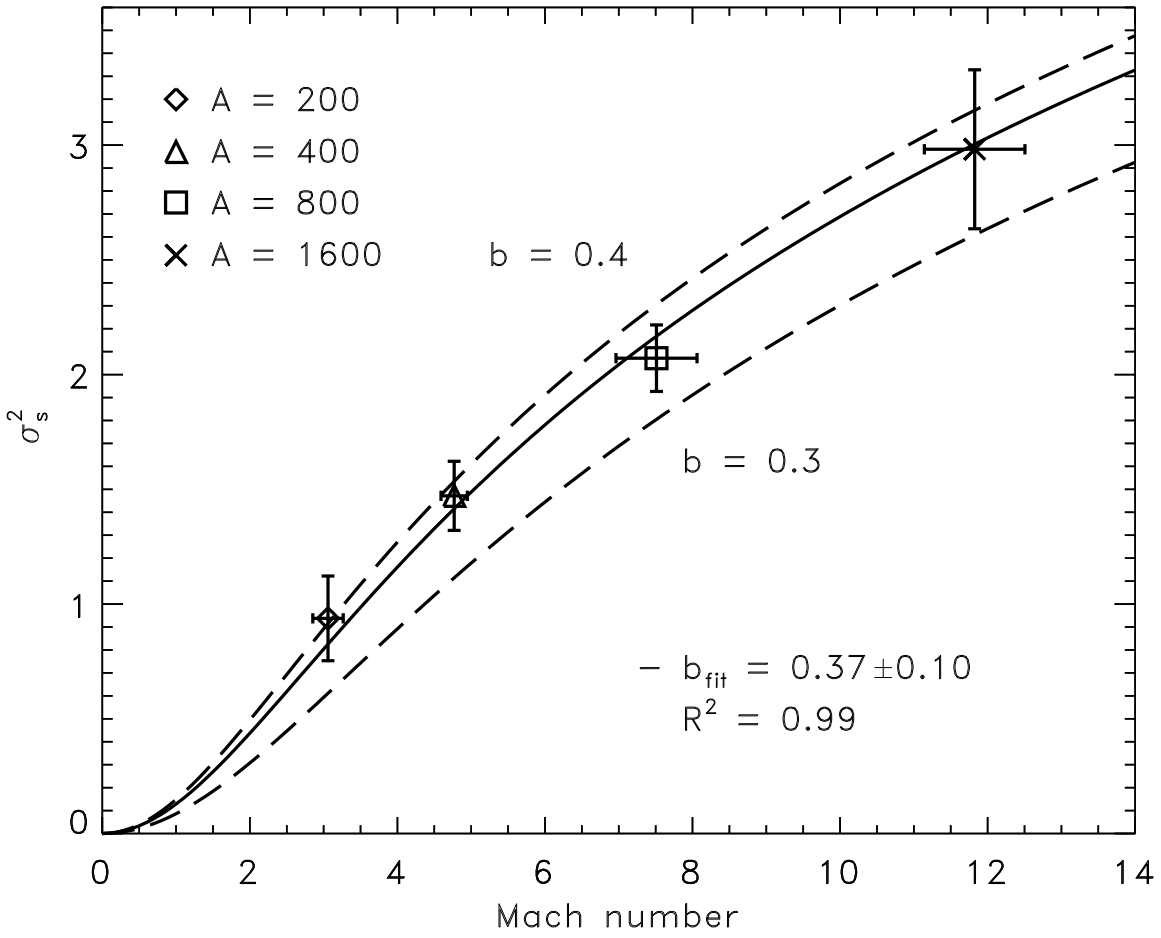

Figure 4.2 The density variance–Mach number relation for isothermal turbulence (approximated by setting $\gamma = 1.0001$). In order to reach a wide range of Mach numbers to test the relation, we use stirring amplitudes between $A = 200$ and 1600 (models 1–4 in Table 4.1), leading to Mach numbers between 3 and 12. We fit equation (4.2) to the four points and find the proportionality constant $b = 0.37 \pm 0.10$ with a goodness of fit of $R^2 = 0.99$. The fit is shown as a solid line, while cases with $b = 0.3$ and 0.4 are shown as dashed lines for comparison. Our best fit is consistent with the expectation value $b \sim 1/3$ for purely solenoidal driving (Federrath et al. 2008b, 2010).

4.3. Results

4.3.1. Isothermal comparison

The isothermal gas relation has been studied extensively and is therefore a good comparison test for our hydrodynamics code, set-up, and post-processing methods to determine σ_s (see Section 4.2). For purely solenoidal forcing of the turbulence, we expect a proportionality value of $b \sim 1/3$ in equation (4.2) (Federrath et al. 2008b, 2010). Four simulations were performed at a grid resolution of 256^3 with $\gamma = 1.0001$ to prevent non-isothermal effects brought on by high

stirring amplitudes. The four time-averaged points lie between $b = 0.3$ and 0.4, with a fit of $b = 0.37 \pm 0.10$ and goodness-of-fit parameter $R^2 = 0.99$ (Fig. 4.2). Our measurement of b spans the expected value, thus our methods produce reasonable results for isothermal turbulence. Now that we have established that our simulation and analysis techniques reproduce previous results for isothermal turbulence, we can now move on to study non-isothermal turbulence in the adiabatic regime.

4.3.2. Resolution study

We now test the resolution requirements of density variance and Mach number measurements by performing a series of identical simulations at increasing resolutions of 64^3, 128^3, 256^3, 512^3, and 1024^3 grid cells for $\gamma = 5/3$. Fig. 4.3 shows the density variance–Mach number relation for each simulation and simulation time. We see that first, the density variance and Mach number increase and reach a maximum after about $t_{\rm cross}$ (the lower part of the correlation). In this first part of the evolution, the kinetic energy of the gas increases due to the driving until the kinetic energy power spectrum is established (Schmidt et al. 2009). After the kinetic energy and rms velocity have reached a saturated state (see Fig. 4.1), only the sound speed keeps increasing monotonically, because the dissipated energy heats the gas. This leads to a continuously decreasing Mach number and density variance in the regime of fully developed turbulence (the upper part of the correlation).

The higher the numerical grid resolution, the greater the maximum of σ_s^2 for $N_{\rm res} < 256$, which is seen to converge for $N_{\rm res} \gtrsim 256$. A zoom within the focus area of the density variance–Mach number relation is shown in the bottom panel of Fig. 4.3. These points are independent of the initial jump, but are still seen to converge at increased resolution. For resolutions equal to and above 256^3, the values are almost identical. Therefore the statistics of density variance and rms Mach number may be approximated well by numerical resolutions $\geq 256^3$ cells. This is consistent with the resolution requirements established in Kitsionas et al. (2009), Federrath et al. (2010), Kritsuk et al. (2011b), and Federrath (2013a).

Looking closely at Fig. 4.3, we see that the gas evolves along a curve in the density variance – Mach number plane. This is due to the continuous heating of the gas via the turbulent driving, which lowers the Mach number continuously. The evolution of this curve seems to correlate somewhat with equation (4.2), but is steeper than the theoretical prediction for isothermal turbulence. The behaviour of this curve is quantified in detail in the following subsections,

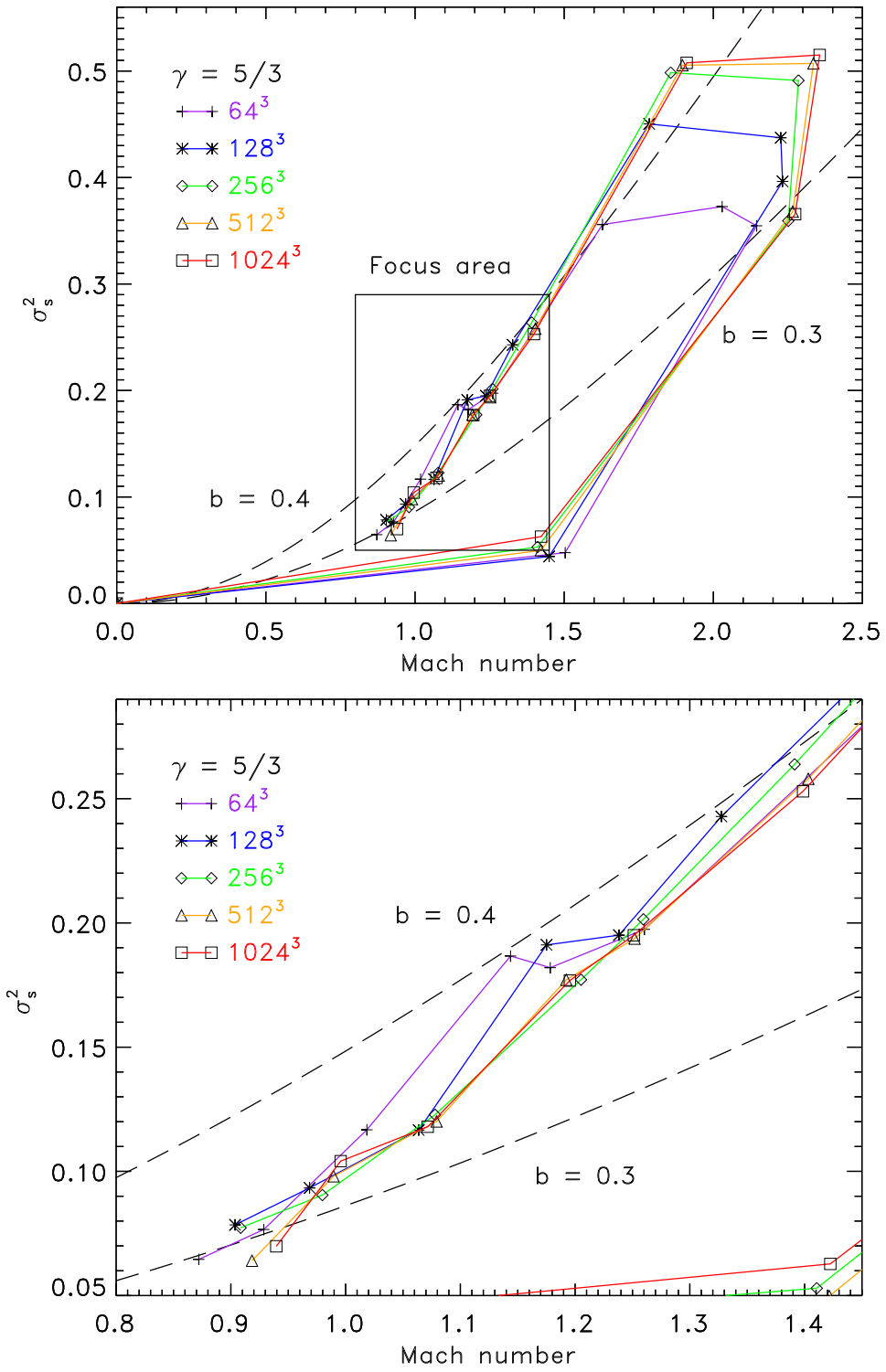

Figure 4.3 Top panel: evolution of simulations with increasing resolution in density variance – rms Mach number space. The dashed lines represent functions of equation (4.2) with $b = 0.3$ and 0.4, for comparison. Initially the rms Mach number increases substantially, then decreases smoothly once the turbulence becomes fully developed (at about $t_{\rm cross}$), as a result of the continuously increasing internal energy, temperature, and sound speed for our ideal gas EOS, equation (4.5). Bottom panel: a magnified region of the top panel, displaying the convergence of statistics. Simulations with $\geq 256^3$ grid cells are representative of the converged system.

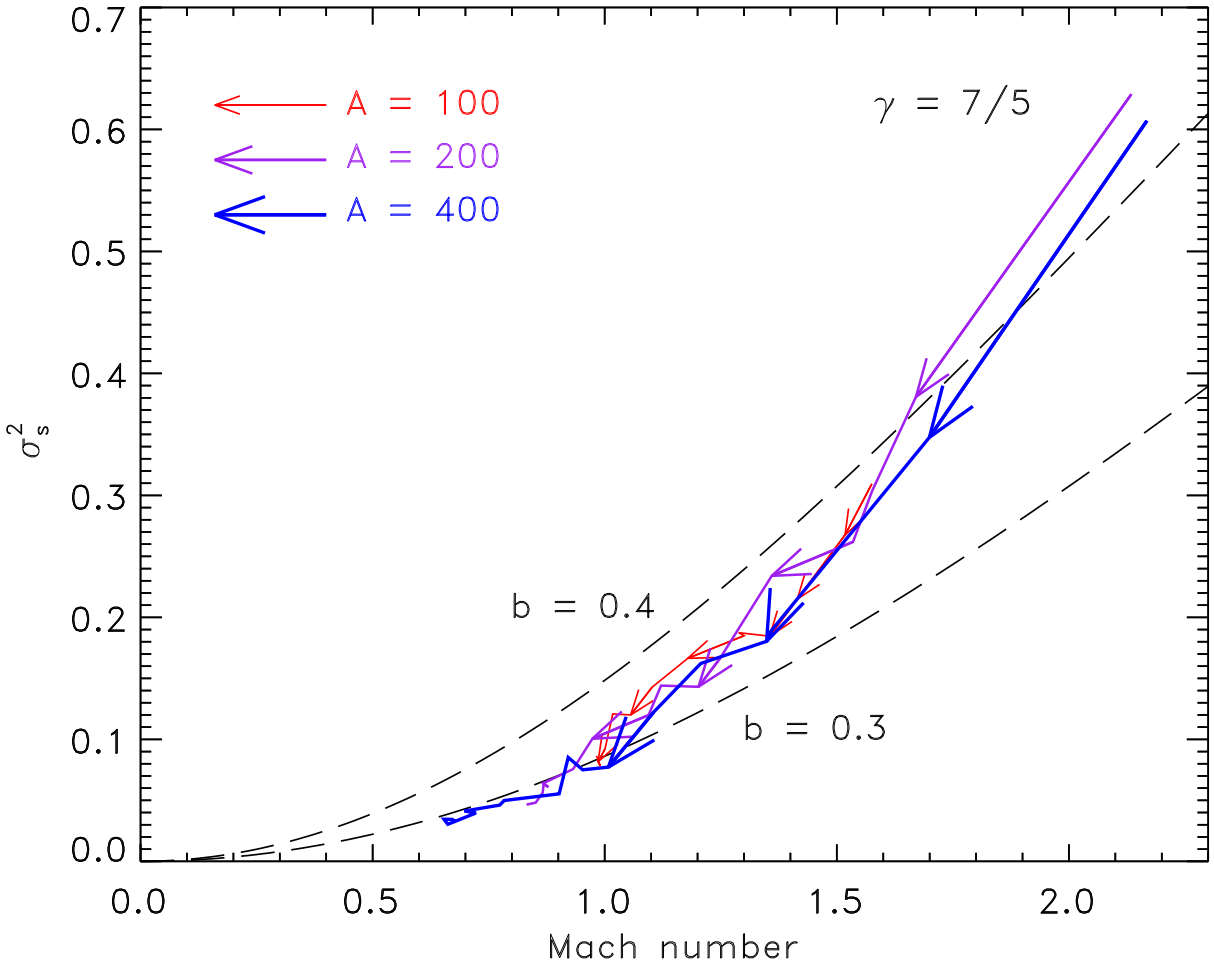

Figure 4.4 Evolution of simulations with $\gamma = 7/5$ and $A = 100$ (red, small arrows), 200 (purple, normal arrows), and 400 (blue, large arrows). The arrows indicate the direction of time evolution.

Sections 4.3.3 and 4.3.4 for $\gamma = 7/5$ and 5/3, respectively.

4.3.3. Diatomic molecular gas: $\gamma = 7/5$

In the first case we look at a diatomic EOS, i.e., $\gamma = 7/5$. We perform three separate simulations with different stirring amplitudes A, and plot their evolutionary curves in Fig. 4.4. The best fit to equation (4.2) from the combined points of all three simulations is $b = 0.37 \pm 0.02$ with a goodness of fit parameter of $R^2 = 0.90$. Note that the increase in sound speed due to gas heating is slow compared to the time it takes to establish a statistically steady state, which is shown in Fig. 4.1, where we see that the velocity dispersion is fully developed after one crossing time. However, the continuous heating in the fully developed regime of turbulence leads to a continuously increasing sound speed, the consequences of which are discussed in more detail in

Table 4.2 Statistical fit parameters for different functions $\sigma_s^2(\mathcal{M})$, for $\gamma = 7/5$.

Fit function	$\sigma_s^2 = \ln(1 + b^2\mathcal{M}^2)$		$\sigma_s^2 = \ln(1 + b'^2\mathcal{M}^\alpha)$		
parameter	b	R^2	b'	α	R^2
$A = 100$	0.35 ± 0.02	0.90	0.32 ± 0.05	2.7 ± 0.8	0.96
$A = 200$	0.38 ± 0.04	0.90	0.31 ± 0.07	2.9 ± 0.8	0.99
$A = 400$	0.37 ± 0.04	0.92	0.30 ± 0.07	2.8 ± 0.8	1.0
All data	0.37 ± 0.02	0.90	0.31 ± 0.04	2.8 ± 0.4	0.99

Notes. R^2 denotes the goodness-of-fit parameter. A value of $R^2 = 1$ indicates a perfect fit to the given data.

Section 4.4.

As in Fig. 4.3, we see in Fig. 4.4 that simulations with $\gamma > 1$ produce a somewhat steeper $\sigma_s^2(\mathcal{M})$ relation compared to the isothermal relation (cf. Fig. 4.2) as time progresses and both σ_s^2 and $\mathcal{M}$ decrease due to the continuous heating of the gas. The different times of each simulation are connected by a line with arrows in Fig. 4.4, indicating increasing time. Therefore a new functional fit might be more appropriate to describe the behaviour in our non-isothermal, adiabatic turbulence simulations.

The simplest modification to the existing model function, equation (4.2), is to allow for variations in the exponent on the Mach number. Our data in Fig. 4.4 indicate that the exponent is somewhat higher than the standard $\mathcal{M}^2$ dependence from equation (4.2). Thus we use the following new fit function to determine the exponent α:

$$\sigma_s^2 = \ln(1 + b'^2\mathcal{M}^\alpha). \tag{4.7}$$

We do not necessarily expect that the coefficient b' in this new relation is the same as b in equation (4.2), but we will test that below. The new function is fitted to the data from each of the three simulations with different driving amplitude and to the combined set of data points. We determine the goodness of fit parameter R^2 for the fits to equations (4.2) and (4.7) and compare them. The results are summarized in Table 4.2.

Table 4.2 shows that for the individual simulations as well as for the combined data set, the modified power-law function from equation (4.7) provides the better fit to the data as quantified by the goodness of fit R^2. The coefficient value $b' = 0.31 \pm 0.04$ is smaller than $b = 0.37 \pm 0.02$, but they are formally consistent with representing the same value, and consistent with the b-value

obtained in our isothermal calculations in Section 4.3.1. In fact, our new fit gives a value that is in agreement with the theoretical expectation for the turbulent driving, namely $b \sim 1/3$ for purely solenoidal driving as applied here.

The exponent α, which is fixed to $\alpha = 2$ in equation (4.2), but allowed to vary in our new fit function, equation (4.7), clearly shows that an almost cubic dependence on $\mathcal{M}$ provides a better fit to the data. We find a best-fitting value of $\alpha = 2.8 \pm 0.4$ in our simulations with $\gamma = 7/5$, leading to a new form of the density variance–Mach number relation for $\gamma = 7/5$ gas,

$$\sigma_s^2 = \ln\left[1 + (0.31 \pm 0.04)^2 \mathcal{M}^{(2.8\pm0.4)}\right]. \tag{4.8}$$

This result presents an interesting question: is the density variance – rms Mach number relation of non-isothermal adiabatic turbulence no longer a quadratic relation, compared to the well-studied isothermal case? We will now explore whether the same/similar holds for $\gamma = 5/3$ and then address this questions in the discussion of Section 4.4, by comparing to a theoretical model of the $\sigma_s^2(\mathcal{M})$ relation.

4.3.4. Monatomic gas: $\gamma = 5/3$

In the second case we look at a monatomic EOS, equation (4.5) with $\gamma = 5/3$. As in the diatomic case we performed three separate simulations with different driving amplitude A, and plot their evolutionary curves in Fig. 4.5 (again with arrows indicating the continuous time evolution to smaller and smaller σ_s^2 and $\mathcal{M}$). A fit with the standard relation, equation (4.2), to the combined data set gives $b = 0.36 \pm 0.02$ with a goodness of fit $R^2 = 0.90$.

Given the same effect occurs as for $\gamma = 7/5$, we fit our new power-law function, equation (4.7), to data from each of the three simulations and to the combined set of data points, and compare the goodness of fit values with those from the fit to equation (4.2). The results are summarized in Table 4.3.

Once again we see a significantly better fit to the power law with exponent $\alpha > 2$. We find that the driving coefficient $b' \sim b$, as for the $\gamma = 7/5$ case, indicating that the physics of the driving is indeed contained in the value of the b parameter, while the fact that we deal with non-isothermal turbulence is reflected in a steeper power-law exponent $\alpha > 2$, compared to the isothermal case. All three simulations fit exponents very close to cubic ($\alpha \sim 3$), with the combined data for $\gamma = 5/3$ fitting a power law of the form

$$\sigma_s^2 = \ln\left[1 + (0.32 \pm 0.03)^2 \mathcal{M}^{(3.0\pm0.5)}\right]. \tag{4.9}$$

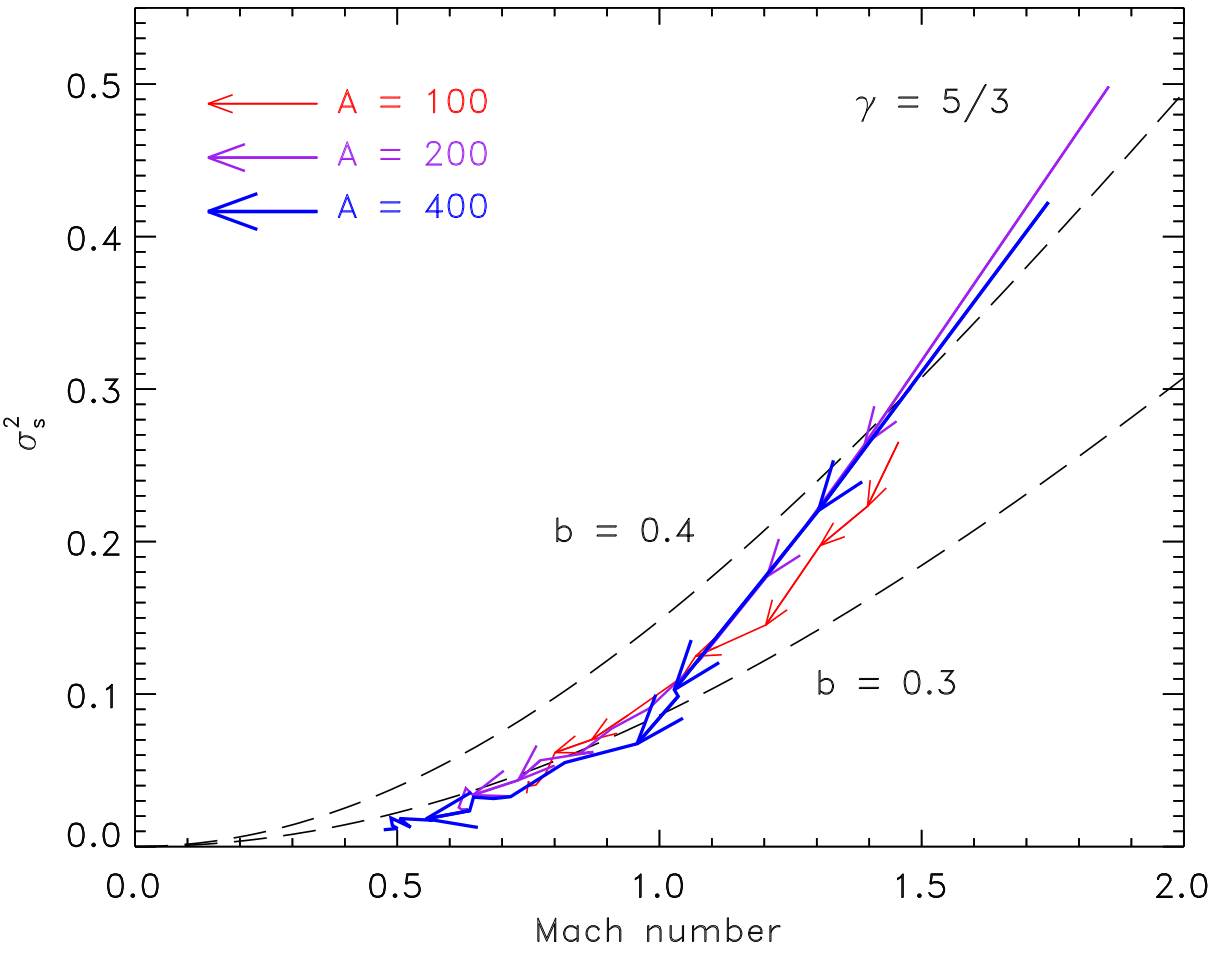

Figure 4.5 Evolution of simulations with $\gamma = 5/3$ and $A = 100$ (red, small arrows), 200 (purple, normal arrows), and 400 (blue, large arrows). The arrows indicate the direction of time evolution.

Table 4.3 Statistical fit parameters for different functions $\sigma_s^2(\mathcal{M})$, for $\gamma = 5/3$.

Fit function	$\sigma_s^2 = \ln(1 + b^2\mathcal{M}^2)$		$\sigma_s^2 = \ln(1 + b'^2\mathcal{M}^\alpha)$		
Parameter	b	R^2	b'	α	R^2
$A = 100$	0.34 ± 0.03	0.92	0.32 ± 0.05	2.8 ± 0.9	0.99
$A = 200$	0.38 ± 0.04	0.91	0.33 ± 0.06	2.9 ± 0.8	1.0
$A = 400$	0.36 ± 0.04	0.89	0.32 ± 0.06	3.0 ± 0.9	1.0
All data	0.36 ± 0.02	0.90	0.32 ± 0.03	3.0 ± 0.5	0.99

Notes. R^2 denotes the goodness-of-fit parameter. A value of $R^2 = 1$ indicates a perfect fit to the given data.

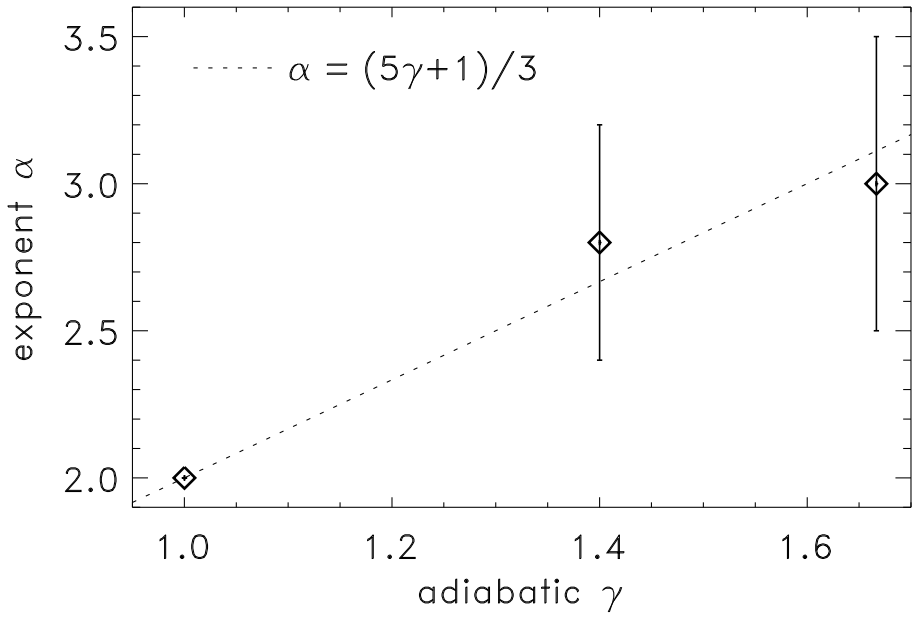

Figure 4.6 Exponent α in the density variance–Mach number relation for different values of the adiabatic index γ. The data points show our simulation measurements and the dotted line is a linear fit with $\alpha = (5\gamma + 1)/3$.

4.3.5. Summary of the results

In summary, both the $\gamma = 7/5$ and $\gamma = 5/3$ cases yield turbulent driving coefficients $b \sim 1/3$ that are all consistent with the theoretical expectation for purely solenoidal driving of the turbulence, and consistent with the b-values found for isothermal turbulence ($\gamma \to 1$).

The exponent α of the $\sigma_s^2(\mathcal{M})$ relation, however, is significantly steeper with $\alpha \sim 2.8 \pm 0.4$ for $\gamma = 7/5$ and $\alpha = 3.0 \pm 0.5$ for $\gamma = 5/3$, compared to the isothermal case, where $\alpha = 2$ provides the best fit to the data. Thus, we see that the exponent α in the density variance–Mach number relation is γ dependent.

In order to provide a heuristic relation that describes the behaviour of $\sigma_s^2(\mathcal{M})$ in adiabatic gases, we fit a linear function to the dependence of α on γ in Fig. 4.6. It is reasonable that α will continuously increase with γ. Thus, we chose the simplest function to approximate our data from $\gamma = 1$ to $\gamma = 5/3$, i.e., a linear interpolation. The result is $\alpha = (5\gamma + 1)/3$. The actual dependence might be somewhat different, but to determine a better fit would require us to measure α for a range of γ values, in much smaller steps $\Delta\gamma$. This is beyond the scope of the paper, but we can already provide a new improved functional form of the density variance–Mach number relation that takes the adiabatic index γ into account. The best-fit function is given by

$$\sigma_s^2 = \ln\left[1 + b^2\mathcal{M}^{(5\gamma+1)/3}\right], \tag{4.10}$$

which is the central result of the paper. Equation (4.10) naturally simplifies to the well-studied isothermal case ($\gamma \to 1$) given by equation (4.2), but also approximately covers cases with $\gamma > 1$, up to $\gamma = 5/3$.

4.4. Discussion

In Sections 4.3.3–4.3.5, we found that the density variance–Mach number relation for adiabatic gases with $\gamma = 7/5$ and $5/3$, respectively, deviates significantly from the isothermal case, equation (4.2). We quantified the discrepancy by fitting an alternative function, equation (4.7), to the data, with the power-law exponent α as a free fit parameter. We find that the power law provides excellent fits, with power-law exponents increasing with γ from $\alpha = 2$ for the isothermal case ($\gamma \to 1$) to $\alpha \sim 3$ for $\gamma = 5/3$. A heuristic function was obtained to provide a new $\sigma_s^2(\mathcal{M})$ relation that takes the dependence on γ into account, given by equation (4.10).

We now compare this results to a recent theoretical model for the density variance–Mach number relation, in order to explain the differences of our adiabatic case to the isothermal and polytropic cases. The detailed derivation of the relation can be found in Molina et al. (2012) and Federrath & Banerjee (2015), where this relation has been explored for magnetized isothermal and polytropic gases, respectively, with the latter representing a special case, where the pressure and temperature of the gas are both uniquely related to the density via

$$P(\rho) \sim \rho^{\Gamma}, \quad T(\rho) \sim \rho^{\Gamma-1}. \tag{4.11}$$

We emphasize that this is different from the adiabatic EOS, equation (4.5), used here, in that the pressure depends on both density and temperature, $P(\rho, T)$. Thus, for any given value of density, the pressure can vary depending on the temperature, while a polytropic EOS will give only a single value of P for a given input ρ.

The basic idea of the theoretical model is to relate the density jump in a single shock to the ensemble of shocks/compressions in a turbulent medium. For that purpose, Padoan & Nordlund (2011) and Molina et al. (2012) applied the equations of mass, momentum, and energy conservation across a shock,

$$\rho_0 v_0 = \rho v, \tag{4.12}$$

$$\rho_0 v_0^2 + P_0 = \rho v^2 + P, \tag{4.13}$$

$$\frac{1}{2}v_0^2 + u_0 + \frac{P_0}{\rho_0} = \frac{1}{2}v^2 + u + \frac{P}{\rho}, \tag{4.14}$$

to derive the density contrast ρ/ρ_0 between the pre-shock gas (denoted with index 0 and on the left-hand side of the equations) and the post-shock gas (no index; right-hand side of the shock jump equations). The EOS, equation (4.5), enters through the pressure P and specific internal energy u in these expressions. Combining these equations leads to the well-known Rankine–Hugoniot shock jump conditions as the solution for the density jump across the shock (Rankine 1870; Hugoniot 1887; Shull & Draine 1987):

$$\frac{\rho}{\rho_0} = \frac{v_0}{v} = \frac{(\gamma+1)b^2\mathcal{M}^2}{(\gamma-1)b^2\mathcal{M}^2+2}. \tag{4.15}$$

Note that we have already introduced the geometrical b parameter, because these shock jump conditions only apply to the plane-parallel component of the shock, parametrized by the parallel component of the sonic Mach number $v_0/c_{s,0} = b\mathcal{M}$ (Molina et al. 2012; Federrath & Banerjee 2015). Following the detailed derivation in Molina et al. (2012), equation (4.15) just needs to be inserted into the general expression for the ensemble of such shocks,

$$\sigma_s^2 = \ln\left(1+\frac{\rho}{\rho_0}\right), \tag{4.16}$$

which leads to the density variance–Mach number relation,

$$\sigma_s^2 = \ln\left(1+\frac{(\gamma+1)b^2\mathcal{M}^2}{(\gamma-1)b^2\mathcal{M}^2+2}\right). \tag{4.17}$$

We immediately see that this new γ-dependent density variance–Mach number relation reduces to the isothermal case, equation (4.2), if we set $\gamma = 1$. In the adiabatic case, however, $\gamma > 1$, which leads to our theoretical prediction as a function of γ, given by equation (4.17).

Fig. 4.7 shows the theoretical prediction given by equation (4.17) for different values of γ together with the isothermal solution and together with our simulation data for $\gamma = 7/5$ and $5/3$. We see that the new relation qualitatively follows the trend of a slightly steeper rise with increasing γ for low Mach number. It also predicts that at high Mach number, the density variance saturates at lower σ_s^2 for increasing γ. This is reasonable, because the density jump across shocks reduces significantly with increasing γ as derived in equation (4.15). This regime needs to be tested in follow-up simulations that reach higher Mach numbers. However, the problem is that the adiabatic heating increases with increasing Mach, such that it quickly counteracts the effect of an increased driving amplitude.

Despite these reasonable qualitative trends produced by our new theoretical relation, equation (4.17), we see that the actual simulation data with $\gamma > 1$ still follow a somewhat steeper

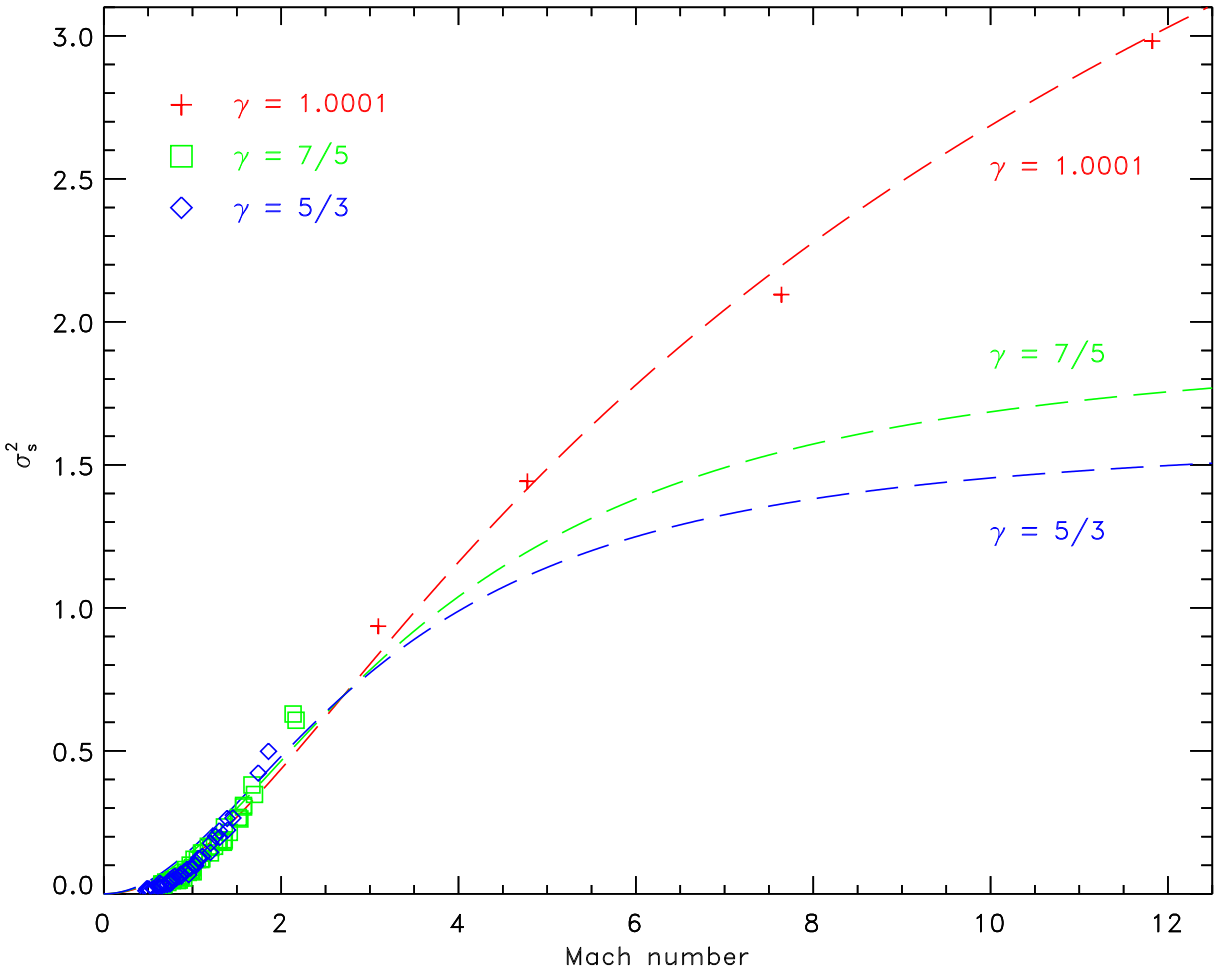

Figure 4.7 Combined density variance–Mach number relation plot, showing all our simulation data with $\gamma = 1.0001$ (red crosses), $\gamma = 7/5$ (green boxes), and $\gamma = 5/3$ (blue diamonds). The dashed lines are our theoretical prediction given by equation (4.17) with the respective values of γ (in the same colour as the simulation data and labelled on each curve).

curve at low Mach number, $b\mathcal{M} \lesssim 1$ in the σ_s^2–$\mathcal{M}$ plane. We speculate that this discrepancy arises, because the theoretical model does not contain any information about the temporal evolution of the gas, in particular about its temperature changes along the evolutionary curve.

However, we can qualitatively argue that any shock will immediately experience the temperature and pressure increase associated with the adiabatic compression. This will reduce the density jump significantly, such that the density variance will be smaller with increasing γ almost immediately when these shocks are about to form (e.g., the theoretical limit for $\gamma = 5/3$ is $\rho/\rho_0 = 4$). Thus, shocks in high-γ gas will be significantly reduced and so will be the statistical variance of density fluctuations, σ_s^2. The important point here is that this process almost instantaneously reduces the density variance.

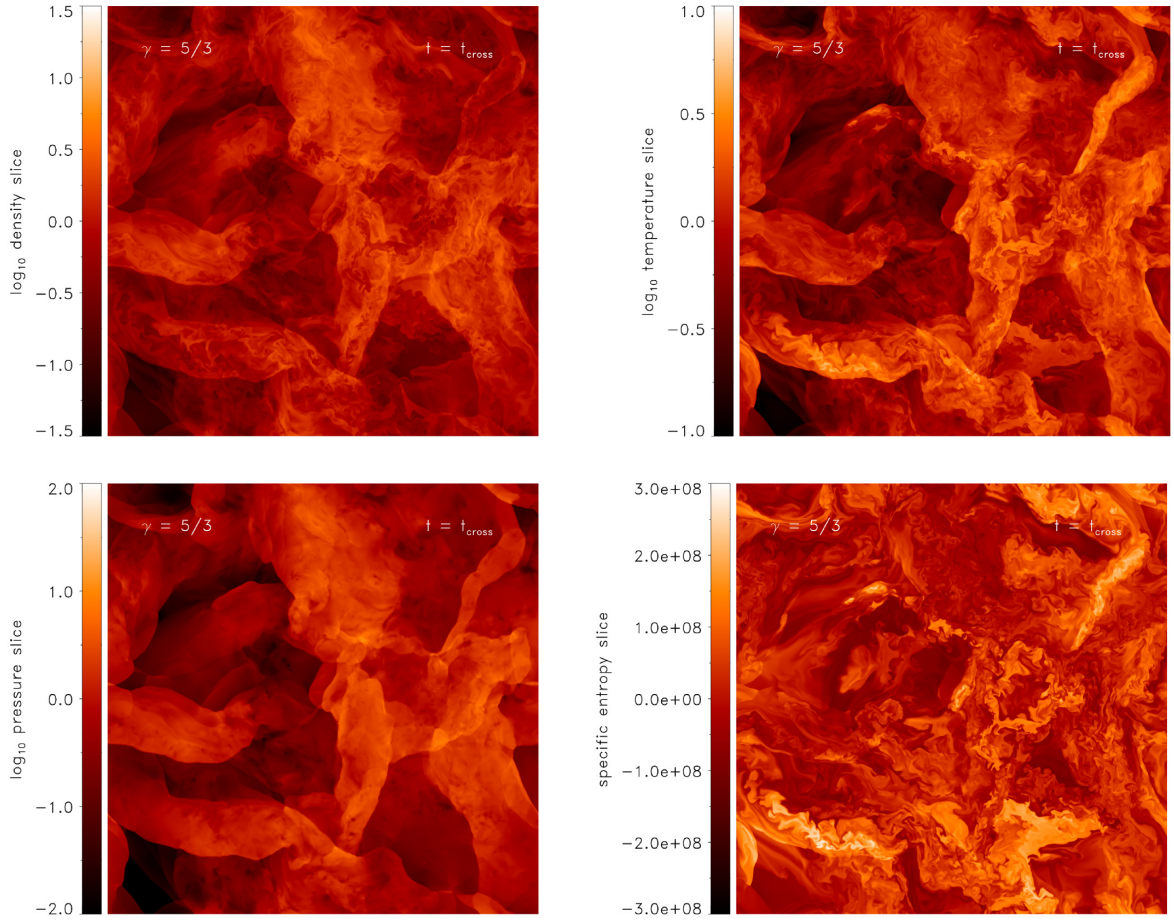

Figure 4.8 Slices of the normalized density (top left), temperature (top right), pressure (bottom left), and specific entropy (bottom right) at $t = t_{\rm cross}$ for $\gamma = 5/3$, $A = 200$, and a numerical resolution of 1024^3. It is evident that gas at a given density can have a wide range of temperatures and pressures, unlike a polytropic EOS where T and P are unique functions of the density only.

At the same time, each shock dissipates energy, locally increasing the temperature and internal energy of the ideal adiabatic gas. This increases the sound speed, but at first only locally in the shocks, which leads to a decreasing pre-shock sonic Mach number over time, resulting in the time evolution (shown as arrows) in Figs. 4.4 and 4.5. We can thus qualitatively understand the time dependence and resulting $\sigma_s^2(\mathcal{M})$ relations for $\gamma > 1$. The $\sigma_s^2(\mathcal{M})$ relation is steeper, because σ_s^2 responds almost instantaneously to the local pressure and temperature increase in shocks, while the Mach number reduction is delayed, because the sound speed increases only in the post-shock gas, while our theoretical equation (4.17) is based on the large-scale, volume-weighted pre-shock Mach number.

In order to substantiate our findings, we show density, temperature, pressure, and entropy slices

of our highest resolution simulation with 1024^3 grid cells and adiabatic $\gamma = 5/3$ in Fig. 4.8. We see two important points. First, the pressure and temperature are not unique functions of the density, but for a given density, the gas can have a range of temperatures and pressures, as implied by equation (4.5). This is substantiated by the entropy slice shown in the bottom right-hand panel of Fig. 4.8, which is not uniform, demonstrating that the gas is not barotropic, but that the pressure depends on density *and* temperature. There is clearly viscous heating, which is primarily due to shocks in the $b\mathcal{M} > 1$ regime, while turbulent dissipation (eddy viscosity) becomes a more important heating mechanism when $b\mathcal{M} < 1$. Quantifying both contributions is beyond the scope of this paper. Second, the adiabatic heating primarily occurs in the post-shock gas. The rise of the internal energy does not immediately reduce the global post-shock Mach number, but slowly diffuses to large scales, before it affects $\mathcal{M}$, leading to the steeper-than-isothermal $\sigma_s^2(\mathcal{M})$ relations we found for $\gamma > 1$.

Finally, Fig. 4.9 shows density–temperature correlation PDFs. It is evident that for any given density, there is a wide range of temperatures and that the heating indeed primarily occurs in the densest gas, i.e., in the post-shock regions. Also note the continuous increase in the overall temperature of the gas between $t = t_{\rm cross}$ (top panel) and $t = 2\,t_{\rm cross}$ (bottom panel), which leads to the slowly decreasing $\mathcal{M}$ over time.

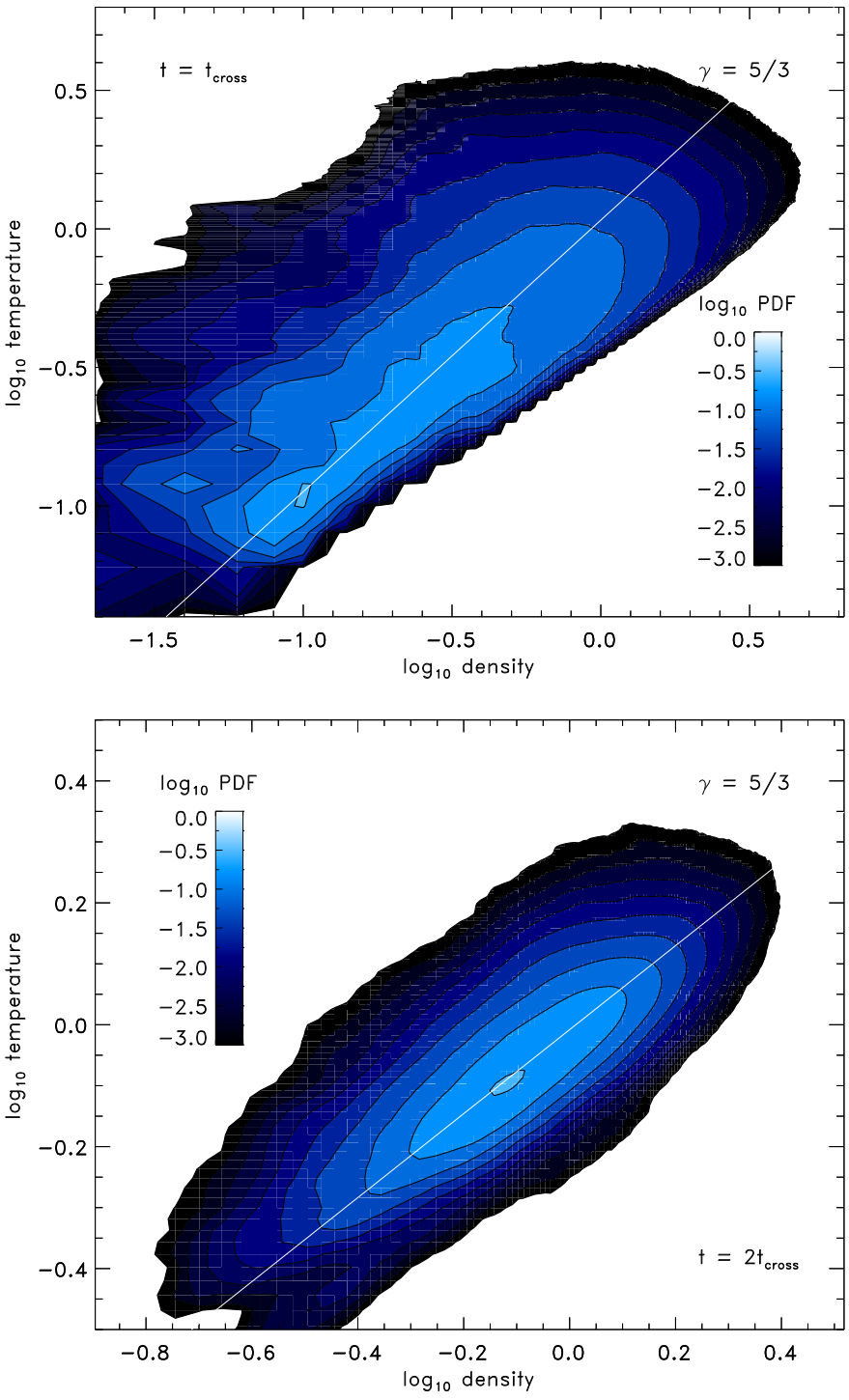

Figure 4.9 Density–temperature correlation PDFs for our adiabatic turbulence simulations with $\gamma = 5/3$, $A = 200$, and $N_{\rm res} = 1024$. The top panel shows the results at $t = t_{\rm cross}$, while the bottom panel is for $t = 2t_{\rm cross}$. The distributions are spread by more than an order of magnitude for typical gas densities, around the average correlations (shown as white lines) with $T \sim \rho^{\gamma-1}$. The continuous heating of the gas indicated by the overall rise in temperature at $t = 2\,t_{\rm cross}$ compared to $t = t_{\rm cross}$ primarily occurs in the post-shock gas, while the Mach number entering equation (4.17) only applies to the pre-shock gas. This produces the steeper dependence of σ_s^2 on $\mathcal{M}$ that we find in our central result, equation (4.10).

4.5. Summary and conclusion

We performed hydrodynamical simulations of supersonic and subsonic turbulence, employing an ideal EOS with adiabatic indices $\gamma = 1.0001$ (nearly isothermal), $\gamma = 7/5$ (diatomic molecular gas), and $\gamma = 5/3$ (monatomic gas). Section 4.3 provided a detailed analysis of the density variance–Mach number relation, $\sigma_s^2(\mathcal{M})$, which is a key ingredient for theoretical models of the star formation rate and the initial mass function. Unlike previous studies of purely isothermal and polytropic turbulence, we find that an ideal gas EOS leads to a steeper dependence of the density variance σ_s^2 on the rms sonic Mach number $\mathcal{M}$. We find a new combined approximate relation of the form given by equation (4.10) for low Mach numbers, $b\mathcal{M} \lesssim 1$, which reduces to the well-known isothermal solution for the special case $\gamma \to 1$, but also covers cases $\gamma > 1$. We argue that the steeper-than-isothermal dependence for $b\mathcal{M} \lesssim 1$ is a result of the local heating of the gas in post-shock regions, with the global sonic pre-shock Mach number in the relation being affected later in the evolution. This is because the turbulent driving keeps increasing the internal energy reservoir, leading to an ever increasing global sound speed in adiabatic gases. This is in stark contrast to isothermal and polytropic gases, where the sonic Mach number reaches a statistical steady state rather than continuously decreasing.

We derived a theoretical model, equation (4.17), for the $\sigma_s^2(\mathcal{M})$ relation in Section 4.4, which is based on the Rankine–Hugoniot shock jump conditions and provides reasonable fits to all our data. It furthermore predicts a saturation of σ_s^2 for $b\mathcal{M} \gg 1$, which is not yet in reach by numerical simulations. Such a saturation is reasonable for $\gamma > 1$, given the fact that adiabatic shocks always have a finite jump in density, while isothermal shocks can theoretically have an infinitely large jump in density across the shock. Both equation (4.10) for $b\mathcal{M} \lesssim 1$ and equation (4.17) for $b\mathcal{M} > 1$ naturally simplify to the standard isothermal relation, equation (4.2) for $\gamma = 1$.

We conclude that changes in the adiabatic exponent γ can introduce important modifications in the density variance–Mach number relation and we provide an approximation of that behaviour in equation (4.10). However, we emphasize that the real ISM is a mixture of atomic and molecular phases and that the effective EOS is determined by a complex balance of heating and cooling processes, which in turn depend on the chemical evolution and exposure to interstellar and local radiation fields (e.g., from massive stars). Thus, our systematic study sheds some light on the dependence of turbulent density fluctuations on the thermodynamics and composition of interstellar gas and more detailed studies including realistic heating and cooling are required to

make further progress.

We hope that this work provides a more general understanding of the density variance–Mach number relation in the ISM. This is especially true for the warm, atomic part of the ISM, where the gas is clearly not isothermal and may be approximated with an adiabatic EOS with $\gamma > 1$, which was not covered by previous density variance–Mach number relations in the literature. Our new relations in this paper attempt to cover this regime and do seem to approximately do so, as tested with the set of simulations presented here. We hope that the new relations will provide useful generalizations of the previous (purely isothermal) relations, which are key ingredients for theoretical models of star formation (see e.g., the review by Padoan et al. 2014).

Acknowledgements

We thank the referee, Sam Falle, for his timely and constructive report, which improved the paper significantly. CF acknowledges funding provided by the Australian Research Council's Discovery Projects (grants DP130102078 and DP150104329). We gratefully acknowledge the Jülich Supercomputing Centre (grant hhd20), the Leibniz Rechenzentrum and the Gauss Centre for Supercomputing (grant pr32lo), the Partnership for Advanced Computing in Europe (PRACE grant pr89mu), and the National Computational Infrastructure (grants n72 and ek9), supported by the Australian Government. This work was further supported by resources provided by the Pawsey Supercomputing Centre with funding from the Australian Government and the Government of Western Australia.

CHAPTER 5

Conclusions

> Poets say science takes away from the beauty of the stars – mere globs of gas atoms. Nothing is "mere." I too can see the stars on a desert night, and feel them. But do I see less or more? The vastness of the heavens stretches my imagination – stuck on this carousel my little eye can catch one-million-year-old light. A vast pattern – of which I am a part. …What is the pattern, or the meaning, or the "why?" It does not do harm to the mystery to know a little about it. For far more marvellous is the truth than any artists of the past imagined it. Why do the poets of the present not speak of it? What men are poets who can speak of Jupiter if he were a man, but if he is an immense spinning sphere of methane and ammonia must be silent?
>
> – Richard P. Feynman[1]

Protostellar jets are an integral part of the star formation process. They are responsible for the removal of excess angular momentum critical to the growth of protostars, while feeding that angular momentum back into molecular clouds to regulate the formation of stellar cores and gravitational collapse. While many of the features of these jets are still unresolved, numerical models allow us to predict the structure of the launching region, while also providing a virtual

[1] *The Feynman Lectures on Physics.* 1963, Vol. 1, 3-6, footnote. (Feynman 1963).

laboratory to investigate the effects of jets on their surrounding environment at time scales much longer than the duration of all human observations.

In this thesis, we have conducted a detailed investigation into both the origin and influence of protostellar jets, with the aim of shedding light on the importance of jet feedback in the star formation process. These studies have been theoretical in nature: each study involved the creation of a numerical model and selection of relevant parameters, followed by extensive computations and detailed analysis. Here we summarize critical points from these studies.

One of the most important parts of this thesis is our work in shedding light on the physical mechanisms that influence the radial localization of disc winds, the prominent candidate for the origin of protostellar jets; we find that winds exist in a narrow region of protostellar discs, where the magnetic configuration satisfies physical constraints on the existence of these types of winds. Our work also confirms that the constraints invoked are the ones that control launching, as the wind exists in the region where the constraints are indeed met. In our models the radial localization is due – on the inward side – to insufficient field-matter coupling, leading to inadequate bending of the magnetic field lines to launch winds. On the outward side we have the opposite problem: the field-matter coupling becomes so great that there is substantial field bending and magnetic disc compression, which leads to negligible wind density at the disc surface and an insignificant local mass-loss rate. Both processes combine to give a Gaussian-like profile for $\mathrm{d}\dot{M}_{\rm wind}/\mathrm{d}r$.

We find that the radial location and mass-loss rate of disc winds are highly sensitive to the magnetic field structure and composition of the disc. Higher accretion rates are mediated by winds at smaller radii with lower ejection/accretion ratios ($\dot{M}_{\rm out}/\dot{M}_{\rm in}$). Stronger magnetic fields lead to winds at smaller radii with lower $\dot{M}_{\rm out}/\dot{M}_{\rm in}$, while increasing the surface density has the opposite effect. Flattening the surface density profile substantially widens the launching region and increases $\dot{M}_{\rm out}/\dot{M}_{\rm in}$. Increasing the field-matter coupling away from the disc midplane leads to greater field bending and disc compression, moving the launching region closer to the star while reducing $\dot{M}_{\rm out}/\dot{M}_{\rm in}$. Therefore, disc winds can account for a wide range of measured footprint radii and $\dot{M}_{\rm out}/\dot{M}_{\rm in}$ throughout the accretion/jet launching phase.

Under the assumption that only a small amount of disc material should participate in the outflow (e.g. Königl & Pudritz 2000), we find that our disc wind models are naturally bounded by $\dot{M}_{\rm out}/\dot{M}_{\rm in} \lesssim 0.1$. As a consequence, some disc winds exhibit a split configuration, with two radially localized regions separated by an intermediate region where wind launching is

ineffective as a steady-state solution, due to excessive mass loading of the field lines[2]. Split wind configurations have been observed for a number of protostellar objects, relating to the kinematic splitting of the LVC into broad and narrow components (e.g. Banzatti et al. 2019).

At the other end of the scale, we investigate the statistical properties of non-isothermal, turbulent interstellar gas – that which is driven by protostellar jets and other energetic processes. We find that simulated driven adiabatic turbulence is inherently different to the extensively studied case of isothermal turbulence. Energy injection via turbulent driving gradually increases the internal energy reservoir through local heating in post-shock regions. This steepens the density variance–Mach number relation because of the steady increase in the global sound speed, opposite to the isothermal case, where a statistical steady state forms once the turbulence saturates. We provide empirical and theoretical relations to the density variance–Mach number for low and high Mach numbers, which naturally simplifies to the standard isothermal case for an adiabatic index of $\gamma = 1$.

The work contained in this thesis provides new insights into the launching and large-scale effects of protostellar jets in a star formation context. A complete picture of the life cycle of jets is still quite far off, and these contributions only examine processes at the beginning and end of jet evolution. However, these studies also have a potential impact on our understanding of planet formation (through modification of protostellar discs by winds), and theoretical models of the star formation rate (through modelling of the turbulent density distribution). They provide us with a deeper perspective on the interconnectedness and complexity of the processes that formed our solar system and home planet, Earth.

5.1. Future work

There are many outstanding questions regarding the origin and influence of outflows on the surrounding medium. While we have made progress with the models developed in this thesis, such as the exploration of radial localization of the wind-launching region, there are a number of obvious extensions to our models that will provide additional insight into the processes surrounding protostellar jets. Below, we briefly mention some possibilities for interesting follow-up work to that presented in this thesis.

[2]While steady-state solutions are ineffective in this intermediate region, unstable launching configurations such as episodic outbursts cannot be ruled out.

Low β_0 solutions The current understanding of protostellar disc structure is that of a disc with weak magnetization ($\beta_0 \sim 10^4$), and magnetic diffusion varying with height (Turner et al. 2014). These discs are dominated by a laminar region surrounding the midplane, with accretion and field line bending occurring where β reaches equipartition. Previous authors were successful in modelling weakly ionized disc winds using the 1.5D radially localized methodology (Wardle 1997), including the contribution of MRI-induced turbulence (Salmeron et al. 2007). With the addition of a self-consistent vertical diffusivity profile (see Chapter 3), we are now in a position to model this scenario in greater detail. A systematic study of disc winds with a wide range of β_0 will enable us to examine how the wind morphology changes between strong ($\beta_0 \gtrsim 1$) and weak ($\beta_0 \gg 1$) regimes.

Variation of β_0 with radius Given that the radial extent and mass outflow of disc winds are highly dependent on the magnetic field strength and bending, it is important to characterize how the launching region behaves for configurations other than our constant-β_0 scenario. This will be addressed in future work.

Non-zero radial drift of poloidal magnetic field lines Recent work by Bai & Stone (2017) has shown that the Hall effect plays an important role in radial drift of poloidal magnetic field lines in discs, causing inward or outward drift depending on whether the field is aligned/anti-aligned with rotation, respectively. While our 1+1.5D models are steady state, this does not prevent us from modelling steady radial field drift, even if parametrized. Wardle & Königl (1993) investigated radial drift in the 1.5D case using a simplified diffusivity, finding that solutions with the same value of (ϵ - ϵ_B), where ϵ is the normalized inward radial speed and ϵ_B is the normalized azimuthal component of the electric field E (which measures the radial drift speed of the poloidal magnetic field lines), produced qualitatively similar results. With the self-consistent diffusivity models of Chapter 3, we will be able to examine the effects of radial drift on the properties of the wind in more detail.

Inverted magnetic fields Numerous recent studies have shown the importance of the magnetic field orientation in dictating disc structure through the Hall diffusivity (e.g. Salmeron et al. 2011; Bai 2015; Béthune et al. 2017; Bai & Stone 2017; Wurster et al. 2018), hence a natural extension of our work is to see how the launching region and wind strength change with magnetic fields anti-aligned to rotation.

Vertical temperature profile Protoplanetary gas is heated by X-rays, cosmic rays, stellar irradiation, and magnetic heating (which may be calculated self-consistently). It cools by radiative diffusion (in the disc interior) and according to its emissivity (in the atmosphere). These effects are currently being incorporated into the 1.5D models (Salmeron et al., in prep) which, in combination with the 1+1.5D model framework and grain chemistry (see point below), could be used to predict the vertical emitted spectra of our disc models to assess the extent to which these features are formed in the disc atmosphere. The features to be modelled are the CO first-overtone bands at 2.3 μm and permitted emission lines of Mg I (1.5 μm), Na I (2.2 μm), and the Ca II infrared triplet lines (0.85 μm).

Inclusion of dust grains and chemistry The inclusion of grains is important for understanding the impact of disc winds on planet formation. The presence of grains substantially increases the magnetic diffusion within the disc by absorbing electrons and ions from the gas phase, thereby reducing the magnetic conductivity of the gas by many orders of magnitude (Wardle 2007); we showed in Chapter 3 that this would modify the wind structure substantially. In a future study, we shall incorporate dust grain physics and a steady-state chemical network into the calculations of the diffusion coefficients, in order to examine the position and outflow rate of disc winds. We shall also include grain processing (e.g. Salmeron & Ireland 2012) in a subsequent study to show how grains may grow and experience heating as they accelerate in a disc wind.

Magnetic fields and adiabatic effects While studies of the density variance–Mach number relation have been performed in the limits of isothermal–magnetized (Molina et al. 2012) and adiabatic–hydrodynamic turbulence (Chapter 4), no study has as of yet examined how adiabatic turbulence would behave with the addition of magnetic fields. For a more complete understanding of supersonic turbulence, an investigation into the properties of magnetized-adiabatic turbulence is a natural extension to the work presented in this thesis.

Further statistical analysis As shown in Chapter 4, driven adiabatic turbulence is inherently different to its isothermal counterpart, as its properties change (e.g. sound speed) in response to energy injection from external sources. To understand this behaviour in greater depth requires a detailed study examining the turbulent response to both solenoidal and compressive driving (e.g. Federrath et al. 2008b), and intermittency, fractal dimension, and time dependence (e.g. Federrath et al. 2009, 2010).

APPENDIX A

Resolution study

This Appendix was originally presented as Appendix A to Nolan et al. (2017).

Here we present the results of a resolution study undertaken to determine the convergent resolution for the 1+1.5D models. We perform a series of identical simulations, using the outer region of the weak-wind model in Section 2.5.1, at increasing resolutions until the ejection/accretion ratio and radial range of the wind-launching region converge. These models are characterized by $a_0 = 1, \dot{M}_{\rm in} = 10^{-5} M_\odot\ {\rm yr}^{-1}$, and a surface density profile of $\Sigma(r) = 630(r/{\rm au})^{-1}\ {\rm g\ cm}^{-2}$. The results of the study are shown in Table A.1. From the table we see that the simulations are converged for $k \gtrsim 1000$, where k is the number of 1.5D solutions per decade of radius (see equation 2.28). Hence we use a resolution of $k = 1000$ for all 1+1.5D models presented in this paper.

Table A.1 Selected properties of a representative 1+1.5D model (the outer region of the weak-wind model in Section 2.5.1), characterized by $a_0 = 1$, $\dot{M}_{\rm in} = 10^{-5} M_\odot$ yr^{-1}, and $\Sigma(r) = 630(r/{\rm au})^{-1}$ g cm^{-2}, at increasing resolutions. From left to right, these properties are the resolution per decade of radius, the number of solutions spanning the wind-launching region, the ejection/accretion ratio, and the radial range of the wind. Models with $k \gtrsim 1000$ are representative of the converged system.

k	$\mathrm{N_{solutions}}$	$\dot{M}_{\rm out}/\dot{M}_{\rm in}$	$\mathrm{r_{range}}$ (au)
20	2	2.140×10^{-3}	0.1220
50	4	5.145×10^{-3}	0.1415
100	9	7.391×10^{-3}	0.1888
200	19	8.528×10^{-3}	0.2124
500	49	9.042×10^{-3}	0.2267
1000	97	8.698×10^{-3}	0.2267
2000	194	8.795×10^{-3}	0.2277
4000	388	8.818×10^{-3}	0.2282

APPENDIX B

Div B study

This Appendix was originally presented as Appendix B to Nolan et al. (2017).

We can prove that the 1+1.5D models satisfy the $\nabla \cdot \mathbf{B} = 0$ constraint by comparing the estimated local scale length L for B_z (derived using B_r and $\nabla \cdot \mathbf{B} = 0$; see equation 2.32), with the disc scale height z_h. The method for calculating L is outlined in Section 2.4.3. Fig. B.1 displays the local ratio of L/z_h in the (r, z)-plane for the strong wind model described in Section 2.5.1. From the figure we see that within the disc, the minimum value for this ratio is 25, and increases with radius and to infinity at the disc midplane. Hence we can confirm beyond doubt that the $\nabla \cdot \mathbf{B} = 0$ condition is satisfied to within error in our 1+1.5D models.

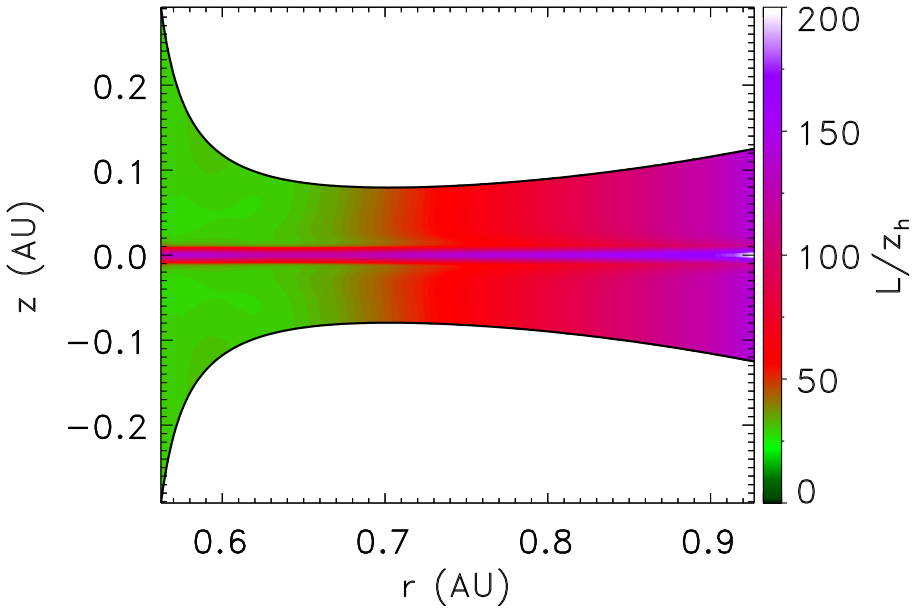

Figure B.1 The local ratio of L/z_h in the (r, z)-plane, for the strong-wind model described in Section 2.5.1, where L is the vertical scale length of B_z, derived using B_r and $\nabla \cdot \mathbf{B} = 0$ (see equation 2.32), and z_h is the disc scale height.

APPENDIX C

Midplane ionization model

This Appendix was originally presented as Appendix C to Nolan et al. (2017).

In order to calculate the three diffusivity components (equations 2.1 - 2.3) and close the system of non-ideal equations, we use the following model to calculate the electron density at the midplane. We adopt the simplification of KSW10, i.e. that the ratios of the diffusivities are constant with z. These ratios are calculated at the midplane and then applied to the vertical structure of the disc. We assume that grains have settled out and that the electron (and ion) density is determined by the equilibrium ionization balance equation (e.g. Salmeron & Wardle 2005, equation 35), in the limit where the dominant recombination mechanism is the radiative recombination of metal ions (Fromang et al. 2002; Salmeron & Wardle 2003). The electron density is then given by

$$n_{\mathrm{e}}(r) = \left(\frac{\zeta n_{\mathrm{H}}}{\alpha}\right)^{\frac{1}{2}}, \tag{C.1}$$

where $\alpha = 3\times10^{-11}T^{-1/2}$ cm^3 s^{-1} is the radiative recombination rate for the metal ions (Salmeron & Wardle 2005) and $n_{\mathrm{H}} = \rho/1.4m_{\mathrm{H}}$. The ionization rate ζ is made up of contributions from mechanisms which may be active at the disc midplane, namely cosmic rays (ζ_{CR}), X-rays (ζ_{XR}), and radioactivity of nuclides within the disc (ζ_{R}), therefore $\zeta = \zeta_{\mathrm{CR}}+\zeta_{\mathrm{XR}}+\zeta_{\mathrm{R}}$. Thermal ionization is not considered in our models, as it is most relevant for temperatures > 1000 K, or for $r \lesssim 0.1$ au assuming the minimum mass solar nebula (MMSN) radial temperature profile of Hayashi (1981) (see equation 2.17). We do not incorporate a vertical temperature profile and also ignore the high-temperature atmosphere likely to be present above the midplane (see Glassgold et al. 2004).

We also exclude ultraviolet photons, as they have penetration depths < 0.1 g cm^{-2} (Perez-Becker & Chiang 2011) and are relevant in the surface layers only.

We calculate the ionization rate contributed by cosmic rays according to the model outlined in Salmeron & Wardle (2005), as it applies to the disc midplane

$$\zeta_{\rm CR} = 10^{-17} \exp(-\Sigma/2\lambda_{\rm CR}) \ {\rm s}^{-1}, \tag{C.2}$$

where Σ is the disc surface density and $\lambda_{\rm CR} = 96$ g cm^{-2} is the attenuation length for cosmic ray penetration (Umebayashi & Nakano 1981).

Stellar X-rays can penetrate a column density $\sim$10 g cm^{-2} (Igea & Glassgold 1999), and can therefore contribute to the ionization balance at the disc midplane only at large radii and low surface densities. We estimate the ionization rate contributed by this agent by using the following fit by Bai & Goodman (2009) to the Monte Carlo radiative transfer results of Igea & Glassgold (1999), assuming a dominant X-ray photon energy of $T_{\rm X} = 3$ keV,

$$\begin{aligned} \zeta_{\rm XR} \ = \ & \frac{L_{\rm X}}{10^{29} \ {\rm erg \ s^{-1}}} \left(\frac{r}{1 \ {\rm au}} \right)^{-2.2} \\ & \times (2\zeta_1 \exp^{-(N_{\rm H}/N_1)^{0.4}} \\ & + 2\zeta_2 \exp^{-(N_{\rm H}/N_2)^{0.65}}) \ {\rm s}^{-1}. \end{aligned} \tag{C.3}$$

In this fit, the intensity of direct X-rays is $\zeta_1 = 6 \times 10^{-12}$ s^{-1} and that of scattered X-rays is $\zeta_2 = 10^{-15}$ s^{-1}, with respective penetration columns of $N_1 = 1.5 \times 10^{21}$ cm^{-2} and $N_2 = 7 \times 10^{23}$ cm^{-2} (Bai & Goodman 2009). The column density of hydrogen nuclei at the midplane $N_{\rm H}$ is related to the disc surface density via $N_{\rm H} = (\Sigma/2)/(1.4 m_{\rm H})$ and we assume the X-ray luminosity of the protostar to be $L_{\rm X} = 10^{29}$ erg s^{-1}.

Finally, we estimate the ionization rate associated with the decay of radioactive elements present in the disc (mainly ^{40}K) in terms of the fraction of heavy metal elements in the gas phase δ_2, and the abundance of grains relative to that of molecular clouds $f_{\rm g}$:

$$\zeta_{\rm R} = 6.9 \times 10^{-23} \left[\delta_2 + (1 - \delta_2) f_{\rm g} \right] \ {\rm s}^{-1} \tag{C.4}$$

(Umebayashi & Nakano 1981, 1990), where $\delta_2 = 0.02$. The parameter $f_{\rm g}$ is set to zero (Sano et al. 2000) in accordance with the assumption that dust grains have settled to the disc midplane.

The contributions of each of the three ionization mechanisms to the total ionization rate at the disc midplane are shown in Fig. C.1 for comparative purposes.

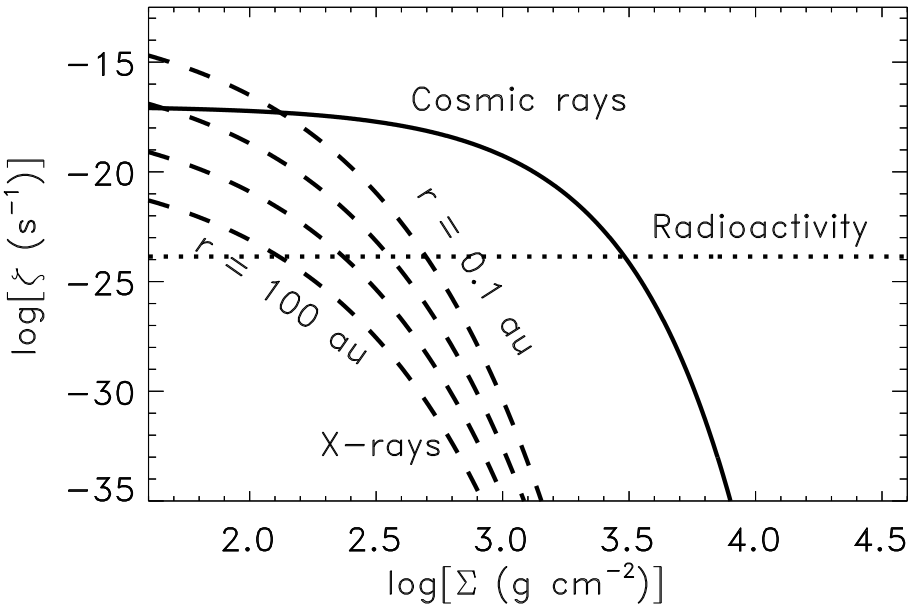

Figure C.1 Ionization rates [s^{-1}] at the disc midplane contributed by cosmic rays (solid line, equation C.2), X-rays (dashed lines, equation C.3), and radioactive decay (dotted line, equation C.4), as a function of the surface density. The X-ray ionization rates are displayed for r = 0.1, 1, 10, and 100 au.

APPENDIX D

Disc wind model methodology

In this thesis we develop a new approach to modelling protostellar disc winds in the non-ideal MHD regime. We achieve this by linking together a set of radially localized, vertical 1.5D solutions of the type designed by Wardle & Königl (1993), Königl et al. (2010) and Salmeron et al. (2011), in order to create a radially extended, 1+1.5D model of the wind-launching region in axisymmetrical coordinates (r, z). In this appendix we provide a detailed overview of the 1.5D solutions that make up our model, which is only included in part in Chapters 2 and 3. This includes the equations of non-ideal MHD, the derived dimensionless system of non-ideal ODEs, the boundary conditions that help to fully define this system, and the methodology employed to solve it. We refer the reader to Section 2.4 for an overview of the methodology used to subsequently connect these 1.5D models in radius, in order to form the radially extended 1+1.5D disc wind model.

D.1. The equations of non-ideal MHD

The equations of non-ideal MHD describe the evolution of the gas density ρ, velocity $\mathbf{v}$, and the magnetic field strength $\mathbf{B}$ in terms of the gas pressure P, gravitational potential Φ, current density $\mathbf{J}$ and electric field in either the inertial reference frame ($\mathbf{E}$) or in the neutral gas reference frame ($\mathbf{E}'$). They include the conservation of mass

$$\frac{\partial \rho}{\partial t} + \nabla \cdot (\rho \mathbf{v}) = 0, \tag{D.1}$$

the conservation of momentum for the neutral gas

$$\rho\frac{\partial \mathbf{v}}{\partial t} + \rho(\mathbf{v}\cdot\nabla)\mathbf{v} + \nabla P + \rho\nabla\Phi - \frac{\mathbf{J}\times\mathbf{B}}{c} = 0, \tag{D.2}$$

and the induction equation

$$\frac{\partial \mathbf{B}}{\partial t} = -c\nabla\times\mathbf{E} = \nabla\times(\mathbf{v}\times\mathbf{B}) - c\nabla\times\mathbf{E}', \tag{D.3}$$

where c is the speed of light. In our models, we use the isothermal equation of state in equation (D.2)

$$P = \rho c_{\rm s}^2 = \frac{\rho k_{\rm B} T}{\mu m_{\rm H}}, \tag{D.4}$$

where $c_{\rm s}$ is the isothermal sound speed, T is the gas temperature, $\mu \equiv m/m_{\rm H} = 2.33$ is the mean molecular weight, m is the mean mass of the neutral particles, and $m_{\rm H}$ is the mass of a hydrogen atom. This prescription assumes a neutral gas composed of molecular hydrogen and helium in the ratio $n_{\rm He}/n_{\rm H_2} = 0.2$ (Hayashi 1981). Additionally, the gravitational potential of the central object (equation D.2) is defined in cylindrical coordinates (r, ϕ, z) by

$$\Phi = -\frac{GM_\star}{(r^2+z^2)^{\frac{1}{2}}}, \tag{D.5}$$

where G is the gravitational constant and $M_\star$ is the mass of the protostar. For all models in Chapters 2 and 3 we assume that $M_\star/M_\odot = 1$.

Ampère's law relates the current density $\mathbf{J}$ to the magnetic field strength $\mathbf{B}$ via the expression

$$\mathbf{J} = \frac{c}{4\pi}\nabla\times\mathbf{B}, \tag{D.6}$$

(ignoring the displacement current) and the magnetic field satisfies the solenoidal condition

$$\nabla\cdot\mathbf{B} = 0. \tag{D.7}$$

D.1.1. Derivation of non-ideal MHD terms

In Chapters 2 and 3 we assume that the evolutionary time-scale of the flow is long compared with the time-scale of the charge-neutral collisions, so that the inertia of the charges may be ignored. As a result of the weak ionization of the disc we may also assume that the thermal pressure is negligible compared to the force exerted by a large-scale, ordered magnetic field. Therefore, the charged particles drift in accordance with the instantaneous Lorentz force and the drag force associated with neutral collisions. These assumptions enable the effects of the

charged species on the neutrals to be incorporated using the conductivity tensor formulation (e.g. Wardle 1999), allowing the three basic field-matter diffusion mechanisms (ambipolar, Hall and Ohm) to be included without the need for separate equations for each fluid component (Königl et al. 2010). This greatly simplifies the calculations, particularly when dust grains are incorporated into the models.

To derive the components of the conductivity tensor, we first describe the Hall parameter β_j: the ratio of species j's gyrofrequency to its collision frequency with the neutrals. This is a measure of the degree of coupling between a given charged species and the magnetic field, with $\beta_j \gg 1$ indicating strong coupling and $\beta_j \ll 1$ denoting weak coupling. The Hall parameter of species j is defined in terms of its mass m_j, electric charge $Z_j e$, and $\gamma_j = \langle\sigma v\rangle_j/(m_j + m)$, where $\langle\sigma v\rangle_j$ is the rate coefficient for collisional momentum transfer between charged particles of mass m_j and neutrals:

$$\beta_j = \frac{|Z_j|eB}{m_j c}\frac{1}{\gamma_j \rho}. \tag{D.8}$$

In equation (D.8),

$$B \equiv |\mathbf{B}| sgn\{B_z\} \tag{D.9}$$

is the signed magnetic field amplitude, with the sign included to keep the dependence of the Hall conductivity on the magnetic field polarity (see equation D.14).

We make the following assumptions concerning the gas composition, which simplify the analysis. In addition to the neutral gas composition of $n_{He}/n_{H_2} = 0.2$, we assume a fluid with only two charged species, positively charged ions (denoted i, with $Z_i > 0$) and negatively charged electrons (denoted e, with $Z_e < 0$), where the mean ion mass is $m_i = 30 m_H$, representative of the heavy ion component of dense molecular clouds (Draine et al. 1983). Ions and electrons could dominate the charged species during the late phases of disc evolution, after the dust grains have settled to the midplane or when the temperature is high enough that the grains are destroyed (e.g. in the disc atmosphere or the dense inner regions of the disc) (see Nakagawa et al. 1981; Dullemond & Dominik 2004; D'Alessio et al. 2006). The ion and electron Hall parameters are related by $\beta_i = q\beta_e$, where

$$q = \frac{m_e}{m_i}\frac{m_i + m}{m_e + m}\frac{\langle\sigma v\rangle_e}{\langle\sigma v\rangle_i}. \tag{D.10}$$

In the case of an ion-electron plasma we use the ion and electron rate coefficients of Draine et al. (1983):

$$\langle\sigma v\rangle_i = 1.6 \times 10^{-9}\ \mathrm{cm^3\ s^{-1}}, \tag{D.11}$$

and

$$\langle \sigma v \rangle_{\rm e} = 1.0 \times 10^{-15} \left(\frac{128 k_{\rm B} T}{9\pi m_{\rm e}} \right)^{\frac{1}{2}} \ {\rm cm}^3 \ {\rm s}^{-1}. \tag{D.12}$$

Substituting these coefficients into equation (D.10), we find that $q \approx 1.3 \times 10^{-4} \sqrt{T}$.

With the groundwork laid, we now define the components of the conductivity tensor $\boldsymbol{\sigma}$ for an ion-electron plasma (Salmeron & Wardle 2003). These are the Ohm, Hall and Pedersen terms, given by

$$\sigma_{\rm O} = \frac{ec}{B} \sum_{\rm j} n_{\rm j} |Z_{\rm j}| \beta_{\rm j}, \tag{D.13}$$

$$\sigma_{\rm H} = \frac{ec}{B} \sum_{\rm j} \frac{n_{\rm j} Z_{\rm j}}{1 + \beta_{\rm j}^2}, \tag{D.14}$$

and

$$\sigma_{\rm P} = \frac{ec}{B} \sum_{\rm j} \frac{n_{\rm j} |Z_{\rm j}| \beta_{\rm j}}{1 + \beta_{\rm j}^2} \tag{D.15}$$

respectively, where $n_{\rm j}$ is the number density of charged species j. We also employ

$$\sigma_{\perp} = \sqrt{\sigma_{\rm H}^2 + \sigma_{\rm P}^2}; \tag{D.16}$$

the total conductivity perpendicular to the magnetic field. Assuming an ion-electron plasma and charge neutrality via

$$\sum_{\rm j} n_{\rm j} Z_{\rm j} = 0, \tag{D.17}$$

equations (D.13) - (D.16) become

$$\sigma_{\rm O} = \frac{ec n_{\rm e} |Z_{\rm e}|}{B} (\beta_e + \beta_i), \tag{D.18}$$

$$\sigma_{\rm H} = \frac{ec n_{\rm e} |Z_{\rm e}|}{B} \frac{(\beta_e + \beta_i)(\beta_e - \beta_i)}{(1 + \beta_e^2)(1 + \beta_i^2)}, \tag{D.19}$$

$$\sigma_{\rm P} = \frac{ec n_{\rm e} |Z_{\rm e}|}{B} \frac{(1 + \beta_e \beta_i)(\beta_e + \beta_i)}{(1 + \beta_e^2)(1 + \beta_i^2)}, \tag{D.20}$$

and

$$\sigma_{\perp} = \frac{ec n_{\rm e} |Z_{\rm e}|}{B} \frac{(\beta_e + \beta_i)}{\sqrt{(1 + \beta_e^2)(1 + \beta_i^2)}}. \tag{D.21}$$

The conductivity tensor $\boldsymbol{\sigma}$ establishes the link between the current density $\mathbf{J}$ and the electric field in the neutral reference frame $\mathbf{E}'$, via Ohm's Law:

$$\mathbf{J} = \boldsymbol{\sigma} \cdot \mathbf{E}' = \sigma_{\rm O} \mathbf{E}'_{\parallel} + \sigma_{\rm H} \hat{\mathbf{B}} \times \mathbf{E}'_{\perp} + \sigma_{\rm P} \mathbf{E}'_{\perp}, \tag{D.22}$$

where $\hat{\mathbf{B}}$ is the unit vector in the direction of the magnetic field and the subscript $\perp$ denotes the direction perpendicular to $\hat{\mathbf{B}}$.

We now introduce the Ohm, Hall and ambipolar diffusivity terms, given by

$$\eta_{\rm O} = \frac{c^2}{4\pi\sigma_{\rm O}}, \tag{D.23}$$

$$\eta_{\rm H} = \frac{c^2}{4\pi\sigma_\perp}\frac{\sigma_{\rm H}}{\sigma_\perp}, \tag{D.24}$$

and

$$\eta_{\rm A} = \frac{c^2}{4\pi\sigma_\perp}\frac{\sigma_{\rm P}}{\sigma_\perp} - \eta_{\rm O}. \tag{D.25}$$

Substituting the conductivity equations (D.18) - (D.21) into equations (D.23) - (D.25), and assuming $q \ll 1$ gives the diffusion terms for an ion-electron plasma,

$$\eta_{\rm O} = \frac{c^2 m_{\rm e}\gamma_{\rm e}\rho}{4\pi e^2 n_{\rm e}}, \tag{D.26}$$

$$\eta_{\rm H} = \frac{cB}{4\pi e n_{\rm e}}, \tag{D.27}$$

and

$$\eta_{\rm A} = \frac{B^2}{4\pi m_{\rm i}\gamma_{\rm i}\rho n_{\rm e}}. \tag{D.28}$$

Finally, combining Ampére's Law (equation D.6) and Ohm's Law (equation D.22), and substituting the resulting expression for $\mathbf{E}'$ into equation (D.3), leads to the final form of the induction equation

$$\frac{\partial \mathbf{B}}{\partial t} = \nabla\times(\mathbf{v}\times\mathbf{B}) - \nabla\times[\eta_{\rm O}\nabla\times\mathbf{B} + \eta_{\rm H}(\nabla\times\mathbf{B})\times\hat{\mathbf{B}} + \eta_{\rm A}(\nabla\times\mathbf{B})_\perp]. \tag{D.29}$$

D.1.2. Ionization model

In order to close the system of non-ideal MHD equations, we use an ionization model to calculate the electron density n_e (see equations D.26 – D.28). We assume that grains have settled out and that the electron (and ion) density is determined by the equilibrium ionization balance equation (e.g. Salmeron & Wardle 2005, equation 35), in the limit where the dominant recombination mechanism is the radiative recombination of metal ions (Fromang et al. 2002; Salmeron & Wardle 2003). The electron density is then given by

$$n_{\rm e}(r) = \left(\frac{\zeta n_{\rm H}}{\alpha}\right)^{\frac{1}{2}}, \tag{D.30}$$

where $\alpha = 3\times10^{-11}T^{-1/2}$ cm^3 s^{-1} is the radiative recombination rate for the metal ions (Salmeron & Wardle 2005) and $n_{\rm H} = \rho/1.4m_{\rm H}$. The ionization rate ζ is made up of contributions from mechanisms which may be active at the disc midplane, namely cosmic rays ($\zeta_{\rm CR}$), X-rays ($\zeta_{\rm XR}$) and radioactivity of nuclides within the disc ($\zeta_{\rm R}$), therefore giving

$$\zeta = \zeta_{\rm CR} + \zeta_{\rm XR} + \zeta_{\rm R}. \tag{D.31}$$

In Chapter 2 we adopt the simplification of Königl et al. (2010), i.e. that the ratios of the diffusivities are constant with z. These ratios are calculated at the midplane using the midplane ionization model found in Appendix C, and then applied to the vertical structure of the disc. In Chapter 3, we remove this simplification and calculate the diffusivities at all z. The ionization model for this more general approach is found in Section 3.2.5.

D.2. Dimensionless system of equations in z

Assuming a steady state, axisymmetric, geometrically thin, vertically isothermal, nearly Keplerian disc, which is dynamic equilibrium within the gravitational potential of the central protostar, we can simplify the equations of non-ideal MHD in Section D.1 into a system of ordinary differential equations (ODEs) in the vertical coordinate z, joined by a set of algebraic relations. The derivation of this system of ODEs is outlined in detail in Wardle & Königl (1993) and Königl et al. (2010), and hence we do not reproduce it here. We also present the system of equations in terms of the three diffusivities (η_O, η_H, and η_A), as opposed to the three conductivities (σ_O, σ_H, and σ_P), as they are more intuitively connected to the three diffusivity regimes, and adopt the more widely used midplane plasma beta $\beta_0(\equiv 8\pi P/B_0)$, instead of the ratio of the midplane Alfvén speed to the isothermal sound speed $a_0(\equiv v_{A0}/c_s)$. These two parameters are related via $\beta_0 = 2/a_0^2$.

In order to solve the system of simplefied non-ideal ODEs, we convert them to dimensionless form using the following normalizations:

$$\tilde{z} \equiv \frac{z}{h_T}, \qquad \tilde{\rho} \equiv \frac{\rho}{\rho_0}, \tag{D.32}$$

$$\boldsymbol{w} \equiv \frac{\mathbf{v} - v_K\hat{\boldsymbol{\phi}}}{c_s}, \qquad \boldsymbol{w}_E \equiv \frac{c\mathbf{E}/B_0 + v_K\hat{\mathbf{r}}}{c_s}, \qquad \boldsymbol{e}' \equiv \frac{c\mathbf{E}'}{c_s B_0}, \tag{D.33}$$

$$\boldsymbol{j} \equiv \frac{4\pi h_T \mathbf{J}}{cB_0}, \qquad \tilde{\boldsymbol{\eta}} = \frac{\beta_0\boldsymbol{\eta}}{2c_s h_T}, \qquad \boldsymbol{b} \equiv \frac{B}{B_0}, \tag{D.34}$$

where $h_T = c_s r/v_K$ is the tidal scaleheight of the disc, v_K is the Keplerian velocity, c is the speed of light, and the subscript '0' denotes midplane values. The disc is assumed to be threaded by

open magnetic field lines with an 'even' symmetry, so that the midplane values of the radial and azimuthal field components vanish and $B_z(r,-z) = B_z(r,z)$. All other variables exhibit reflection symmetry about $z = 0$. It is worth noting that, under the adopted field symmetry, $B_0 = B_z$ and hence $b_z = 1$.

With these normalizations in place, the dimensionless system of equations is obtained:

$$\frac{\mathrm{d}w_r}{\mathrm{d}\tilde{z}} = \frac{1}{w_z}\left[\frac{2}{\beta_0}\frac{j_\phi}{\tilde{\rho}} + 2w_\phi\right], \tag{D.35}$$

$$\frac{\mathrm{d}w_\phi}{\mathrm{d}\tilde{z}} = -\frac{1}{w_z}\left[\frac{2}{\beta_0}\frac{j_r}{\tilde{\rho}} + \frac{w_r}{2}\right], \tag{D.36}$$

$$\frac{\mathrm{d}\ln\tilde{\rho}}{\mathrm{d}\tilde{z}} = \frac{1}{1-w_z^2}\left[\frac{2}{\beta_0}\frac{\left(j_r b_\phi - j_\phi b_r\right)}{\tilde{\rho}} - \tilde{z}\right], \tag{D.37}$$

$$\frac{\mathrm{d}w_{Er}}{\mathrm{d}\tilde{z}} = -\frac{3}{2}b_r, \tag{D.38}$$

$$\frac{\mathrm{d}b_r}{\mathrm{d}\tilde{z}} = j_\phi, \tag{D.39}$$

$$\frac{\mathrm{d}b_\phi}{\mathrm{d}\tilde{z}} = -j_r, \tag{D.40}$$

$$e'_r = w_{Er} + w_\phi - w_z b_\phi, \tag{D.41}$$

$$e'_\phi = -\epsilon_B + w_z b_r - w_r, \tag{D.42}$$

$$j_r = \frac{\beta_0}{2}\left(\frac{\tilde{y}(\tilde{\eta}_A\tilde{\eta}_P + \tilde{\eta}_H^2)b_r b + (e'_z b_\phi - e'_\phi)\tilde{\eta}_O\tilde{\eta}_H + e'_r b\tilde{\eta}_O\tilde{\eta}_P}{b\tilde{\eta}_O(\tilde{\eta}_P^2 + \tilde{\eta}_H^2)}\right), \tag{D.43}$$

$$j_\phi = \frac{\beta_0}{2}\left(\frac{\tilde{y}(\tilde{\eta}_A\tilde{\eta}_P + \tilde{\eta}_H^2)b_\phi b + (e'_r - e'_z b_r)\tilde{\eta}_O\tilde{\eta}_H + e'_\phi b\tilde{\eta}_O\tilde{\eta}_P}{b\tilde{\eta}_O(\tilde{\eta}_P^2 + \tilde{\eta}_H^2)}\right), \tag{D.44}$$

$$e'_z = \frac{(e'_r b_\phi - e'_\phi b_r)b\tilde{\eta}_O\tilde{\eta}_H - (e'_r b_r + e'_\phi b_\phi)(\tilde{\eta}_A\tilde{\eta}_P + \tilde{\eta}_H^2)}{\tilde{\eta}_P(b^2\tilde{\eta}_O + \tilde{\eta}_A) + \tilde{\eta}_H^2}, \tag{D.45}$$

where

$$\tilde{y} \equiv \boldsymbol{e}\cdot\boldsymbol{b} = e'_r b_r + e'_\phi b_\phi + e'_z, \tag{D.46}$$

$$\tilde{\eta}_P \equiv \tilde{\eta}_O + \tilde{\eta}_A, \tag{D.47}$$

is the Pedersen diffusivity, and

$$b^2 \equiv \boldsymbol{b}\cdot\boldsymbol{b} = b_r^2 + b_\phi^2 + 1. \tag{D.48}$$

The adopted assumptions also imply $\tilde{\rho}w_z$, b_z and $w_{E\phi}$ are constant with height, with $\tilde{\rho}w_z = w_{z0}$[1], $b_z = 1$, $w_{E\phi} = -\epsilon_B$, where ϵ_B becomes an input parameter of the system, and $j_z \approx 0$.

[1] derived at the midplane, where $\tilde{\rho} = 1$. See also equation (D.70).

In addition to the above equations, the following are also included in order to enable the normalized position of the sonic point and the midplane vertical velocity w_{z0} to be calculated self-consistently as part of the solution

$$\frac{\mathrm{d}\tilde{z}_s}{\mathrm{d}\tilde{z}} = 0, \tag{D.49}$$

$$\frac{\mathrm{d}w_{z0}}{\mathrm{d}\tilde{z}} = 0. \tag{D.50}$$

D.2.1. Parameters

The following parameters fully characterize the disc solutions in our model.

(i) $\beta_0 \equiv 8\pi P/B_0$, the midplane ratio of the gas to magnetic pressures, a measure of the magnetic field strength.

(ii) $T(r)$, the isothermal temperature throughout the vertical disc column at radius r.

(iii) $\Sigma(r)$, the vertically integrated surface density at radius r, defined by

$$\Sigma(r) = 2\int_0^{z_s} \rho \mathrm{d}z, \tag{D.51}$$

which is imposed on the disc.

(iv) $\dot{M}_{acc}(r)$, the vertically integrated mass accretion rate through radius r, defined by

$$\dot{M}_{acc}(r) = -4\pi r \int_{-z_b}^{z_b} \rho v_r \mathrm{d}z. \tag{D.52}$$

(v) $\epsilon_B \equiv -cE_{\phi 0}/c_s B_0$, the normalized azimuthal component of the electric field, which measures the radial drift of the poloidal magnetic field lines.

(vi) $M_\star$, the mass of the central protostar.

Parameters (v) - (vi) are not listed predominantly in Chapters 2 and 3, as they are assumed to be $\epsilon_B = 0$ and $M_\star = M_\odot$ respectively.

D.2.2. Additional equations

In order to self-consistently solve the dimensionless set of equations for a specific vertically integrated surface density $\Sigma(r)$, and mass accretion rate $\dot{M}_{acc}(r)$, we must also include the normalized equations for the local surface density and mass accretion:

$$\frac{\mathrm{d}\sigma}{\mathrm{d}\tilde{z}} = -\tilde{\rho}, \tag{D.53}$$

$$\frac{\mathrm{d}\dot{m}_{acc}}{\mathrm{d}\tilde{z}} = \begin{cases} -2\pi\tilde{\rho}w_r & 0 \leq \tilde{z} \leq \tilde{z}_b \\ 0 & \tilde{z}_b < \tilde{z} \leq \tilde{z}_s \end{cases}, \tag{D.54}$$

where σ is the normalized local surface density

$$\sigma \equiv \frac{\Sigma(r,z)}{\rho_0 h_T}, \tag{D.55}$$

given

$$\Sigma(r,z) = \int_z^{z_s} \rho \mathrm{d}z, \tag{D.56}$$

and $\dot{m}_{acc}$ is the normalized local mass accretion rate

$$\dot{m}_{acc} \equiv \frac{\dot{M}_{acc}(r,z)}{r\rho_0 c_s h_T}, \tag{D.57}$$

given

$$\dot{M}_{acc}(r,z) = -2\pi r \int_z^{z_b} \rho v_r \mathrm{d}z. \tag{D.58}$$

Imposing values for $\Sigma(r)$ and $\dot{M}_{acc}$ transforms ρ_0 and ϵ into dependent variables, and as such, they must also be incorporated into the system of equations in such a way that they may be derived self-consistently as part of the solution. Hence we include

$$\frac{\mathrm{d}\rho_0}{\mathrm{d}\tilde{z}} = 0 \tag{D.59}$$

and

$$\frac{\mathrm{d}\epsilon}{\mathrm{d}\tilde{z}} = 0 \tag{D.60}$$

in the set of ODEs.

D.3. Boundary conditions

The complete set of equations consists of the set of twelve ODEs given by equations (D.35) – (D.40), (D.49) – (D.50), (D.53) – (D.54), and (D.59) – (D.60). This defines a two-point boundary value problem (BVP) for non-linear ODEs. In order to find a unique solution, twelve corresponding boundary conditions must be defined, either at the disc midplane or at the sonic point z_s. They are as follows:

At the midplane. Firstly we assign the radial and azimuthal magnetic field components b_r and b_ϕ with an odd symmetry, resulting in a vanishing value at the midplane. The remaining variables (excluding w_z) must have even (reflection) symmetry at the midplane to maintain consistency, resulting in vanishing derivatives at that location. We also define $\tilde{\rho} = 1$, which follows from the normalization of ρ and parametrize the midplane inward velocity with ϵ, which is later solved for internally as a result of prescribing the total mass accretion rate $\dot{M}_{acc}(r)$ (see Section D.4). Finally, the normalized surface density and mass accretion rate are defined in terms of the global input parameters $\Sigma(r)$ and $\dot{M}_{acc}(r)$.

$$b_{r0} = b_{\phi 0} = 0, \tag{D.61}$$

$$\left(\frac{\mathrm{d}w_r}{\mathrm{d}\tilde{z}}\right)_0 = \left(\frac{\mathrm{d}w_\phi}{\mathrm{d}\tilde{z}}\right)_0 = 0, \tag{D.62}$$

$$\tilde{\rho}_0 = 1, \qquad w_{r0} = -\epsilon \tag{D.63}$$

$$\sigma_0 = \frac{\Sigma(r)}{2\rho_0 h_T} \tag{D.64}$$

$$\dot{m}_{acc,0} = \frac{\dot{M}_{acc}(r)}{2r\rho_0 c_s h_T} \tag{D.65}$$

If we combine these boundary conditions with equations (D.35), (D.36), and (D.41) – (D.44), we arrive at the following expressions for $w_{\phi 0}$ and w_{Er0}, expressed in terms of the normalized diffusivities:

$$w_{\phi 0} = -\frac{\epsilon\tilde{\eta}_{H0}}{4\tilde{\eta}_{P0}} - \frac{(\epsilon - \epsilon_B)}{2\tilde{\eta}_{P0}} \tag{D.66}$$

$$w_{Er0} = \frac{\epsilon}{2}\left(\frac{\tilde{\eta}_{H0}^2 + \tilde{\eta}_{P0}^2}{\tilde{\eta}_{P0}}\right) + (\epsilon - \epsilon_B)\frac{\tilde{\eta}_{H0}}{\tilde{\eta}_{P0}} - w_{\phi 0}, \tag{D.67}$$

where

$$\tilde{\eta}_{P0} \equiv \tilde{\eta}_{O0} + \tilde{\eta}_{A0} \tag{D.68}$$

is the midplane Pedersen diffusivity.

At the sonic point. The sonic point is a critical point of equation (D.37), hence we can obtain a boundary condition at this point by imposing the regularity condition

$$\tilde{z}_s = \frac{2}{\beta_0 \tilde{\rho}_s}(j_{rs} b_{\phi s} - j_{\phi s} b_{rs}). \tag{D.69}$$

Additionally, the density at $\tilde{z}_s$ is given by

$$\tilde{\rho}_s = w_{z0}. \tag{D.70}$$

Finally, the local surface density and mass accretion rate vanish at the sonic point, hence

$$\sigma_s = 0 \tag{D.71}$$

and

$$\dot{m}_{acc,s} = 0. \tag{D.72}$$

D.4. Numerical solution of the disc equations

The two-point BVP is defined by the twelve equations in Section D.2 and corresponding boundary conditions in Section D.3. As the upper boundary at $\tilde{z} = \tilde{z}_s$ is a critical point, using a 'pure' shooting method — i.e. integrating from $\tilde{z} = 0$ to $\tilde{z}_s$ and trying to match boundary conditions at $\tilde{z}_s$ — is generally not feasible; the integration becomes highly erratic when approaching critical points. However, one can circumvent this problem by integrating simultaneously from both ends of the domain to an internal fitting point, which we employ in Chapter 2[2], based on earlier work by Wardle & Königl (1993) and Salmeron et al. (2011).

We begin the process of solution by providing the independent variables β_0, $T(r)$, $\Sigma(r)$, and $\dot{M}_{acc}(r)$, and supplying reasonable guesses for the four unknown variables $\tilde{z}_s$, w_{z0}, ρ_0 and ϵ. From here we can calculate the midplane boundary conditions and integrate the ODEs from the midplane towards $\tilde{z}_s$. If the guessed value of w_{z0} is too high, then w_z will diverge, and if it is too low, w_z peaks and begins to decrease with $\tilde{z}$, which is unphysical. This essentially brackets the correct value of w_{z0}, and hence we use an iterative bisection method to improve upon w_{z0} until the maximum z where successive integrations are converged, is close enough to the sonic point (where $w_z = 1$) to estimate the position of $\tilde{z}_s$ and the values of the variables there.

To complete the derivation of the solution with the approximate values of ρ_0 and ϵ, we renormalize z by the estimated position of the sonic point ($\hat{z} \equiv z/z_s$), and then simultaneously integrate from the midplane and sonic point to an intermediate fitting point (usually $\hat{z} \sim 0.7 - 0.9$), adjusting the guessed variables at each end iteratively until the solution converges.

We now have a matched solution for the variables $\tilde{z}_s$ and w_{z0}, however the values for ρ_0 and ϵ still remain guesses, resulting in a mismatch between the integrated Σ and $\dot{M}_{acc}$ of the solution, and the specified $\Sigma(r)$ and $\dot{M}_{acc}(r)$. To find the correct values for ρ_0 and ϵ, we create a two-dimensional

[2]This method is known as 'Shooting to a fitting point'. More information on shooting methods may be found in Chapter 18 of Press et al. (2007).

grid centred on the guessed values and solve for each combination of $[\rho_0, \epsilon]$, refining the grid until a solution is found that satisfies

$$\frac{|\,\Sigma - \Sigma(r)\,|}{\Sigma(r)} + \frac{|\,\dot{M}_{acc} - \dot{M}_{acc}(r)\,|}{\dot{M}_{acc}} < 1 \times 10^{-5}, \tag{D.73}$$

where Σ and $\dot{M}_{acc}$ are the integrated values from the solutions.

Stiff solutions

In Chapter 3, due to the increased stiffness of the ODEs resulting from calculating the diffusivity components self-consistently, we can no longer reliably integrate a reasonable distance across the domain. This therefore rules out both a single reverse integration from the sonic point $\tilde{z}_s$ back to the fitting point, and also any attempts to shoot from the midplane to $\approx 0.9\tilde{z}_s$ in one integration, to approximate variables at the sonic point. In this case we use a modified 'pure' shooting method, where the domain is partitioned into many discrete intervals, and move the code to quadratic precision to reduce overlap of successful integrations due to precision errors.

We begin similarly to the original method, with the bracketing of w_{z0} and subsequent bisection as far as possible, and save the extent of the integration where values and their derivatives are sufficiently converged. The largest z for which the iterations converge, denoted $\tilde{z}_1$, then becomes the starting point for another set of integrations in $\tilde{z}$, this time iteratively bisecting on $w_z(\tilde{z}_1)$. This process continues until we have an n such that

$$w_z(\tilde{z}_n) \geq 0.95, \tag{D.74}$$

i.e. the combined integrations reach at least 95 percent of the sonic point velocity. At this point we extrapolate from the integrated section up to the projected $\tilde{z}_s$ and iterate on the value of $\tilde{z}_s$ and the extrapolation method until the regularity condition at the sonic point is satisfied. Combined with the method of solving for ρ_0 and ϵ above, this completes the method of calculating the vertical structure of the disc for the models in Chapter 3.

Bibliography

Ádámkovics, M., Glassgold, A. E., & Meijerink, R. 2011, ApJ, 736, 143

Agra-Amboage, V., Dougados, C., Cabrit, S., & Reunanen, J. 2011, A&A, 532, A59

Anderson, J. M., Li, Z.-Y., Krasnopolsky, R., & Blandford, R. 2003, ApJ, 590, L107

Andrews, S. M., & Williams, J. P. 2005, ApJ, 631, 1134

—. 2007, ApJ, 659, 705

Armitage, P. J. 2015, preprint (arXiv:1509.06382)

Aso, Y., et al. 2015, ApJ, 812, 27

Aspin, C., Reipurth, B., Herczeg, G. J., & Capak, P. 2010, ApJL, 719, L50

Audard, M., et al. 2014, in Protostars and Planets VI, ed. H. Beuther, R. S. Klessen, C. P. Dullemond, & T. Henning (Univ. Arizona Press, Tucson), p. 387

Audit, E., & Hennebelle, P. 2005, A&A, 433, 1

—. 2010, A&A, 511, A76

Bacciotti, F., Mundt, R., Ray, T. P., Eislöffel, J., Solf, J., & Camezind, M. 2000, ApJL, 537, L49

Bacciotti, F., Ray, T. P., Mundt, R., Eislöffel, J., & Solf, J. 2002, ApJ, 576, 222

Bae, J., Nelson, R. P., & Hartmann, L. 2016, ApJ, 833, 126

Bai, X.-N. 2014, ApJ, 791, 137

Bai, X.-N. 2015, ApJ, 798, 84

—. 2016, ApJ, 821, 80

Bai, X.-N. 2017, ApJ, 845, 75

Bai, X.-N., & Goodman, J. 2009, ApJ, 701, 737

Bai, X.-N., & Stone, J. M. 2013a, ApJ, 767, 30

—. 2013b, ApJ, 769, 76

Bai, X.-N., & Stone, J. M. 2014, ApJ, 796, 31

—. 2017, ApJ, 836, 46

Balbus, S. A., & Hawley, J. 1998, Rev. Mod. Phys., 70, 1

Balbus, S. A., & Hawley, J. F. 1991, ApJ, 376, 214

Bally, J., Reipurth, B., & Davis, C. J. 2007, in Protostars and Planets V, ed. B. Reipurth, D. Jewitt, & K. Keil (Univ. Arizona Press, Tuscon), p. 215

Bans, A., & Königl, A. 2012, ApJ, 758, 100

Banzatti, A., Pascucci, I., Edwards, S., Fang, M., Gorti, U., & Flock, M. 2019, ApJ, 870, 76

Beck, T. L., Riera, A., Raga, A. C., & Reipurth, B. 2007, AJ, 133, 1221

Beetz, C., Schwarz, C., Dreher, J., & Grauer, R. 2008, Physics Letters A, 372, 3037

Bergin, E. A. 2011, in Physical Processes in Circumstellar Disks around Young Stars, ed. P. J. V. Garcia (Univ. Chicago Press, Chicago), p. 55

Béthune, W., Lesur, G., & Ferreira, J. 2017, A&A, 600, A75

Birnstiel, T., Dullemond, C. P., & Brauer, F. 2009, A&A, 503, L5

Bjerkeli, P., van der Wiel, M. H. D., Harsono, D., Ramsey, J. P., & Jørgensen, J. K. 2016, Nature, 540, 406

Bland-Hawthorn, J., Sutherland, R., Agertz, O., & Moore, B. 2007, ApJL, 670, L109

Blandford, R. D. 1976, MNRAS, 176, 465

Blandford, R. D., & Payne, D. G. 1982, MNRAS, 199, 883

Blandford, R. D., & Znajek, R. L. 1977, MNRAS, 179, 433

Bodenheimer, P. H. 2011, Principles of Star Formation (Springer-Verlag Berlin Heidelberg)

Bouvier, J., Matt, S. P., Mohanty, S., Scholz, A., Stassun, K. G., & Zanni, C. 2014, in Protostars and Planets VI, ed. H. Beuther, R. S. Klessen, C. P. Dullemond, & T. Henning (Univ. Arizona Press, Tucson), p. 433

Burkhart, B., & Lazarian, A. 2012, ApJL, 755, L19

Cabrit, S. 2007, in Star-Disk Interaction in Young Stars, ed. J. Bouvier & I. Appenzeller, Proc. IAU Symp. 243 (Cambridge Univ. Press, Cambridge, UK), p. 203

Cao, X., & Spruit, H. C. 2002, A&A, 385, 289

Carrasco-González, C., Rodríguez, L. F., Anglada, G., Martí, J., Torrelles, J. M., & Osorio, M. 2010, Science, 330, 1209

Casse, F., & Keppens, R. 2002, ApJ, 581, 988

—. 2004, ApJ, 601, 90

Cauley, P. W., Johns-Krull, C. M., Hamilton, C. M., & Lockhart, K. 2012, ApJ, 756, 68

Chabrier, G., Hennebelle, P., & Charlot, S. 2014, ApJ, 796, 75

Cho, W., & Kim, J. 2011, MNRAS, 410, L8

Coffey, D., Bacciotti, F., & Podio, L. 2008, ApJ, 689, 1112

Collins, D. C., Kritsuk, A. G., Padoan, P., Li, H., Xu, H., Ustyugov, S. D., & Norman, M. L. 2012, ApJ, 750, 13

Collins, D. C., Padoan, P., Norman, M. L., & Xu, H. 2011, ApJ, 731, 59

Combet, C., & Ferreira, J. 2008, A&A, 479, 481

Consolmagno, G. J., & Jokipii, J. R. 1978, Moon and Planets, 19, 253

Cooper, J., Bicknell, G., Sutherland, R., & Bland-Hawthorn, J. 2009, ApJ, 703, 330

Cranmer, S. R. 2008, ApJ, 689, 316

—. 2009, ApJ, 706, 824

D'Alessio, P., Calvet, N., Hartmann, L., Franco-Hernández, R., & Servín, H. 2006, ApJ, 638, 314

Dominik, C., & Dullemond, C. P. 2008, A&A, 491, 663

Draine, B. T., Roberge, W. G., & Dalgarno, A. 1983, ApJ, 264, 485

Dullemond, C. P., & Dominik, C. 2004, A&A, 421, 1075

Dullemond, C. P., & Dominik, C. 2005, A&A, 434, 971

Dullemond, C. P., Hollenbach, D., Kamp, I., & D'Alessio, P. 2007, in Protostars and Planets V, ed. B. Reipurth, D. Jewitt, & K. Keil (Univ. Arizona Press, Tucson), p. 555

Dzyurkevich, N., Flock, M., Turner, N. J., Klahr, H., & Henning, T. 2010, A&A, 515, 70

Eisloffel, J., & Mundt, R. 1997, AJ, 114, 280

Ellerbroek, L. E., Podio, L., Kaper, L., Sana, H., Huppenkothen, D., de Koter, A., & Monaco, L. 2013, A&A, 551, A5

Elmegreen, B. G. 2008, ApJ, 672, 1006

Elmegreen, B. G., & Scalo, J. 2004, ARA&A, 42, 211

Eswaran, V., & Pope, S. B. 1988, Comput. Fluids, 16, 257

Fang, M., et al. 2018, ApJ, 868, 28

Federrath, C. 2013a, MNRAS, 436, 1245

—. 2013b, MNRAS, 436, 3167

—. 2015, MNRAS, 450, 4035

Federrath, C., & Banerjee, S. 2015, MNRAS, 448, 3297

Federrath, C., Glover, S. C. O., Klessen, R. S., & Schmidt, W. 2008a, PhST, 132, 014025

Federrath, C., & Klessen, R. S. 2012, ApJ, 761, 156

—. 2013, ApJ, 763, 51

Federrath, C., Klessen, R. S., & Schmidt, W. 2008b, ApJL, 688, L79

—. 2009, ApJ, 692, 364

Federrath, C., Roman-Duval, J., Klessen, R. S., Schmidt, W., & Mac Low, M. 2010, A&A, 512, A81

Federrath, C., Schrön, M., Banerjee, R., & Klessen, R. S. 2014, ApJ, 790, 128

Ferreira, J. 1997, A&A, 319, 340

Ferreira, J. 2007, in Lecture Notes in Physics, Berlin Springer Verlag, Vol. 723, Jets from Young Stars I - Models and Constraints, ed. J. Ferreira, C. Dougados, & E. Whelan, 181

Ferreira, J., Dougados, C., & Cabrit, S. 2006, A&A, 453, 785

Ferreira, J., & Pelletier, G. 1993a, A&A, 276, 625

—. 1993b, A&A, 276, 637

Ferreira, J., & Pelletier, G. 1995, A&A, 295, 807

Ferreira, J., Pelletier, G., & Appl, S. 2000, MNRAS, 312, 387

Ferrière, K. M. 2001, Rev. Modern Phys., 73, 1031

Feynman, R. P. 1963, Feynman lectures on physics - Volume 1 (Addison-Wesley)

Fischera, J., & Dopita, M. 2005, ApJ, 619, 340

Flaherty, K. M., Hughes, A. M., Rosenfeld, K. A., Andrews, S. M., Chiang, E., Simon, J. B., Kerzner, S., & Wilner, D. J. 2015, ApJ, 813, 99

Flaherty, K. M., Hughes, A. M., Teague, R., Simon, J. B., Andrews, S. M., & Wilner, D. J. 2018, ApJ, 856, 117

Flaherty, K. M., et al. 2017, ApJ, 843, 150

Frank, A., et al. 2014, in Protostars and Planets VI, ed. H. Beuther, R. S. Klessen, C. P. Dullemond, & T. Henning (Univ. Arizona Press, Tucson), p. 451

Fromang, S., Latter, H. N., Lesur, G., & Ogilvie, G. I. 2013, A&A, 552, A71

Fromang, S., & Lesur, G. 2019, in EAS Publications Series, Vol. 82, EAS Publications Series, 391–413

Fromang, S., Terquem, C., & Balbus, S. A. 2002, MNRAS, 329, 18

Fung, J., & Chiang, E. 2017, ApJ, 839, 100

Gammie, C. F. 1996, ApJ, 457, 355

Garcia Lopez, R., Nisini, B., Giannini, T., Eislöffel, J., Bacciotti, F., & Podio, L. 2008, A&A, 487, 1019

Gazol, A., & Kim, J. 2013, ApJ, 765, 49

Giacalone, S., Teitler, S., Königl, A., Krijt, S., & Ciesla, F. J. 2019, ApJ, 882, 33

Glassgold, A. E., Najita, J., & Igea, J. 2004, ApJ, 615, 972

Glover, S. C. O., Federrath, C., Mac Low, M., & Klessen, R. S. 2010, MNRAS, 404, 2

Glover, S. C. O., & Mac Low, M.-M. 2007, ApJ, 659, 1317

Goodson, A. P., Böhm, K.-H., & Winglee, R. M. 1999, ApJ, 524, 142

Gregory, S. G., Donati, J.-F., Morin, J., Hussain, G. A. J., Mayne, N. J., Hillenbrand, L. A., & Jardine, M. 2012, ApJ, 755, 97

Gressel, O., Turner, N. J., Nelson, R. P., & McNally, C. P. 2015, ApJ, 801, 84

Hamann, F. 1994, ApJS, 93, 485

Hartigan, P., Edwards, S., & Ghandour, L. 1995, ApJ, 452, 736

Hayashi, C. 1981, Prog. Theor. Phys. Suppl., 70, 35

Hayashi, C., Nakazawa, K., & Nakagawa, Y. 1985, in Protostars and Planets II, ed. D. C. Black & M. S. Matthews (Univ. Arizona Press, Tucson), p. 1100

Hayashi, M. R., Shibata, K., & Matsumoto, R. 1996, ApJ, 468, L37

Hennebelle, P., & Audit, E. 2007, A&A, 465, 431

Hennebelle, P., & Chabrier, G. 2008, ApJ, 684, 395

—. 2011, ApJL, 743, L29

—. 2013, ApJ, 770, 150

Hirota, T., Machida, M. N., Matsushita, Y., Motogi, K., Matsumoto, N., Kim, M. K., Burns, R. A., & Honma, M. 2017, Nature Astronomy, 1, 0146

Hirth, G. A., Mundt, R., & Solf, J. 1997, A&AS, 126, 437

Hopkins, P. F. 2013a, MNRAS, 430, 1653

—. 2013b, MNRAS, 430, 1880

Hugoniot, P. H. 1887, J. l'Ecole Polytechnique, 57, 3

Igea, J., & Glassgold, A. E. 1999, ApJ, 518, 848

Jacquemin-Ide, J., Ferreira, J., & Lesur, G. 2019, arXiv e-prints, arXiv:1909.12258

Johns-Krull, C. M., & Gafford, A. D. 2002, ApJ, 573, 685

Kainulainen, J., Federrath, C., & Henning, T. 2013, A&A, 553, L8

Kitsionas, S., et al. 2009, A&A, 508, 541

Klahr, H., & Hubbard, A. 2014, ApJ, 788, 21

Klessen, R. S. 2000, ApJ, 535, 869

Konigl, A. 1989, ApJ, 342, 208

Königl, A. 1997, in ASP Conf. Ser., Vol. 121, IAU Colloq. 163: Accretion Phenomena and Related Outflows, ed. D. T. Wickramasinghe, G. V. Bicknell, & L. Ferrario (Astron. Soc. Pac., San Francisco), p. 551

Königl, A. 2004, ApJ, 617, 1267

Königl, A., & Pudritz, R. E. 2000, in Protostars and Planets IV, ed. V. Mannings, A. P. Boss, & S. S. Russell (Univ. Arizona Press, Tucson), p. 759

Königl, A., & Salmeron, R. 2011, in Physical Processes in Circumstellar Disks around Young Stars, ed. P. J. V. Garcia (Univ. Chicago Press, Chicago), p. 283

Königl, A., Salmeron, R., & Wardle, M. 2010, MNRAS, 401, 479

Konstandin, L., Girichidis, P., Federrath, C., & Klessen, R. S. 2012, ApJ, 761, 149

Kritsuk, A. G., & Norman, M. L. 2002, ApJL, 569, L127

Kritsuk, A. G., Norman, M. L., Padoan, P., & Wagner, R. 2007, ApJ, 665, 416

Kritsuk, A. G., Norman, M. L., & Wagner, R. 2011a, ApJL, 727, L20

Kritsuk, A. G., et al. 2011b, ApJ, 737, 13

Krumholz, M. R. 2014, Phys. Rep., 539, 49

Krumholz, M. R., & McKee, C. F. 2005, ApJ, 630, 250

Krumholz, M. R., et al. 2014, in Protostars and Planets VI, ed. H. Beuther, R. S. Klessen, C. P. Dullemond, & T. Henning (Univ. Arizona Press, Tucson), p. 243

Kuncic, Z., & Bicknell, G. V. 2004, ApJ, 616, 669

Kunz, M. W., & Lesur, G. 2013, MNRAS, 434, 2295

Lada, C. J. 1985, ARA&A, 23, 267

Lavalley-Fouquet, C., Cabrit, S., & Dougados, C. 2000, A&A, 356, L41

Lee, C.-F., et al. 2018, ApJ, 856, 14

Lemaster, M. N., & Stone, J. M. 2008, ApJL, 682, L97

Lesur, G., Ferreira, J., & Ogilvie, G. I. 2013, A&A, 550, A61

Lesur, G., Kunz, M. W., & Fromang, S. 2014, A&A, 566, A56

Lesur, G. R. J., & Latter, H. 2016, MNRAS, 462, 4549

Leung, P. K. C., & Ogilvie, G. I. 2019, MNRAS, 487, 5155

Li, Z.-Y. 1995, ApJ, 444, 848

—. 1996, ApJ, 465, 855

Li, Z.-Y., Banerjee, R., Pudritz, R. E., Jørgensen, J. K., Shang, H., Krasnopolsky, R., & Maury, A. 2014, in Protostars and Planets VI, ed. H. Beuther, R. S. Klessen, C. P. Dullemond, & T. Henning (Univ. Arizona Press, Tucson), p. 173

Lin, M.-K., & Youdin, A. N. 2015, ApJ, 811, 17

Long, M., Romanova, M. M., Kulkarni, A. K., & Donati, J.-F. 2011, MNRAS, 413, 1061

Long, M., Romanova, M. M., & Lovelace, R. V. E. 2007, MNRAS, 374, 436

—. 2008, MNRAS, 386, 1274

López-Cámara, D., & Raga, A. C. 2010, ApJ, 723, 449

Louvet, F., Dougados, C., Cabrit, S., Mardones, D., Ménard, F., Tabone, B., Pinte, C., & Dent, W. R. F. 2018, A&A, 618, A120

Lovelace, R. V. E. 1976, Nature, 262, 649

Lubow, S. H., Papaloizou, J. C. B., & Pringle, J. E. 1994, MNRAS, 268, 1010

Mac Low, M.-M. 1999, ApJ, 524, 169

Mac Low, M.-M., & Klessen, R. S. 2004, Rev. Modern Phys., 76, 125

Marcus, P. S., Pei, S., Jiang, C.-H., Barranco, J. A., Hassanzadeh, P., & Lecoanet, D. 2015, ApJ, 808, 87

Masson, C. R., & Chernin, L. M. 1993, ApJ, 414, 230

Matt, S., & Pudritz, R. E. 2005, ApJ, 632, L135

—. 2008, ApJ, 681, 391

Matt, S. P., Pinzón, G., Greene, T. P., & Pudritz, R. E. 2012, ApJ, 745, 101

Matzner, C. D., & McKee, C. F. 2000, ApJ, 545, 364

McGroarty, F., Ray, T. P., & Bally, J. 2004, A&A, 415, 189

McKee, C. F., & Ostriker, E. C. 2007, ARA&A, 45, 565

Micic, M., Glover, S. C. O., Federrath, C., & Klessen, R. S. 2012, MNRAS, 421, 2531

Mizuno, H., Markiewicz, W. J., & Voelk, H. J. 1988, A&A, 195, 183

Mohanty, S., & Shu, F. H. 2008, ApJ, 687, 1323

Molina, F. Z., Glover, S. C. O., Federrath, C., & Klessen, R. S. 2012, MNRAS, 423, 2680

Moll, R. 2012, A&A, 548, A76

Motogi, K., Sorai, K., Niinuma, K., Sugiyama, K., Honma, M., & Fujisawa, K. 2013, MNRAS, 428, 349

Najita, J. R., & Shu, F. H. 1994, ApJ, 429, 808

Nakagawa, Y., Nakazawa, K., & Hayashi, C. 1981, Icarus, 45, 517

Natta, A., Testi, L., Alcalá, J. M., Rigliaco, E., Covino, E., Stelzer, B., & D'Elia, V. 2014, A&A, 569, A5

Nelson, R. P., Gressel, O., & Umurhan, O. M. 2013, MNRAS, 435, 2610

Nolan, C. A., Federrath, C., & Salmeron, R. 2019, MNRAS, submitted

Nolan, C. A., Federrath, C., & Sutherland, R. S. 2015, MNRAS, 451, 1380

Nolan, C. A., Salmeron, R., Federrath, C., Bicknell, G. V., & Sutherland, R. S. 2017, MNRAS, 471, 1488

Nordlund, Å., & Padoan, P. 1999, in Interstellar Turbulence, ed. J. Franco & A. Carraminana (Cambridge University Press), 218

Offner, S. S. R., Clark, P. C., Hennebelle, P., Bastian, N., Bate, M. R., Hopkins, P. F., Moraux, E., & Whitworth, A. P. 2014, in Protostars and Planets VI, ed. H. Beuther, R. S. Klessen, C. P. Dullemond, & T. Henning (Univ. Arizona Press, Tucson), p. 53

Ostriker, E. C., Gammie, C. F., & Stone, J. M. 1999, ApJ, 513, 259

Ostriker, E. C., Stone, J. M., & Gammie, C. F. 2001, ApJ, 546, 980

Ouyed, R., & Pudritz, R. E. 1997a, ApJ, 482, 712

—. 1997b, ApJ, 484, 794

Ouyed, R., Pudritz, R. E., & Stone, J. M. 1997, Nature, 385, 409

Padoan, P., Federrath, C., Chabrier, G., Evans, II, N. J., Johnstone, D., Jørgensen, J. K., McKee, C. F., & Nordlund, Å. 2014, in Protostars and Planets VI, ed. H. Beuther, R. S. Klessen, C. P. Dullemond, & T. Henning (Univ. Arizona Press, Tucson), p. 77

Padoan, P., Jones, B. J. T., & Nordlund, A. P. 1997, ApJ, 474, 730

Padoan, P., & Nordlund, Å. 2011, ApJ, 730, 40

Passot, T., & Vázquez-Semadeni, E. 1998, PhRvE, 58, 4501

Pelletier, G., & Pudritz, R. E. 1992, ApJ, 394, 117

Perez-Becker, D., & Chiang, E. 2011, ApJ, 735, 8

Persson, M. V., Harsono, D., Tobin, J. J., van Dishoeck, E. F., Jørgensen, J. K., Murillo, N., & Lai, S.-P. 2016, A&A, 590, A33

Pfeil, T., & Klahr, H. 2019, ApJ, 871, 150

Pinte, C., et al. 2008, A&A, 489, 633

Poincaré, H. 1914, Science and method; translated by Francis Maitland (T. Nelson London), 288

Press, W. H., Teukolsky, S. A., Vetterling, W. T., & Flannery, B. P. 2007, Numerical Recipes 3rd Edition: The Art of Scientific Computing, 3rd edn. (Cambridge University Press)

Price, D. J., & Federrath, C. 2010, MNRAS, 406, 1659

Price, D. J., Federrath, C., & Brunt, C. M. 2011, ApJL, 727, L21

Pudritz, R. E., & Norman, C. A. 1983, ApJ, 274, 677

—. 1986, ApJ, 301, 571

Pudritz, R. E., Ouyed, R., Fendt, C., & Brandenburg, A. 2007, in Protostars and Planets V, ed. B. Reipurth, D. Jewitt, & K. Keil (Univ. Arizona Press, Tucson), p. 277

Pyo, T.-S., Hayashi, M., Kobayashi, N., Terada, H., & Tokunaga, A. T. 2009, ApJ, 694, 654

Pyo, T.-S., et al. 2003, ApJ, 590, 340

Qiu, K., Wyrowski, F., Menten, K. M., Güsten, R., Leurini, S., & Leinz, C. 2011, ApJ, 743, L25

Qiu, K., Zhang, Q., Beuther, H., & Yang, J. 2007, ApJ, 654, 361

Qiu, K., et al. 2008, ApJ, 685, 1005

Raga, A., & Murdin, P. 2002, Encyclopedia of Astronomy and Astrophysics (Cambridge University Press)

Raga, A. C., & Biro, S. 1993, MNRAS, 264, 758

Raga, A. C., Canto, J., Calvet, N., Rodriguez, L. F., & Torrelles, J. M. 1993, A&A, 276, 539

Rankine, W. J. M. 1870, R. Soc. Lond. Philos. Trans. Ser. I, 160, 277

Ray, T., Dougados, C., Bacciotti, F., Eislöffel, J., & Chrysostomou, A. 2007, in Protostars and Planets V, ed. B. Reipurth, D. Jewitt, & K. Keil (Univ. Arizona Press, Tucson), p. 231

Reipurth, B., Bally, J., & Devine, D. 1997, AJ, 114, 2708

Rigliaco, E., Pascucci, I., Gorti, U., Edwards, S., & Hollenbach, D. 2013, ApJ, 772, 60

Romanova, M. M., Long, M., Kulkarni, A. K., Kurosawa, R., Ustyugova, G. V., Koldoba, A. K., & Lovelace, R. V. E. 2007, in IAU Symposium, Vol. 243, Star-Disk Interaction in Young Stars, ed. J. Bouvier & I. Appenzeller, 277–290

Romanova, M. M., Long, M., Lamb, F. K., Kulkarni, A. K., & Donati, J.-F. 2011, MNRAS, 411, 915

Salmeron, R., & Ireland, T. R. 2012, E&PSL, 327, 61

Salmeron, R., Königl, A., & Wardle, M. 2007, MNRAS, 375, 177

—. 2011, MNRAS, 412, 1162

Salmeron, R., & Wardle, M. 2003, MNRAS, 345, 992

—. 2005, MNRAS, 361, 45

Sano, T., Miyama, S., Umebayashi, T., & Nakano, T. 2000, ApJS, 543, 486

Sano, T., & Stone, J. M. 2002, ApJ, 570, 314

Scalo, J., Vázquez-Semadeni, E., Chappell, D., & Passot, T. 1998, ApJ, 504, 835

Schmidt, W., Federrath, C., Hupp, M., Kern, S., & Niemeyer, J. C. 2009, A&A, 494, 127

Seifried, D., Banerjee, R., Klessen, R. S., Duffin, D., & Pudritz, R. E. 2011, MNRAS, 417, 1054

Seon, K.-I. 2012, ApJL, 761, L17

Shariff, K. 2009, Annu. Rev. Fluid Mech., 41, 283

Sheikhnezami, S., Fendt, C., Porth, O., Vaidya, B., & Ghanbari, J. 2012, ApJ, 757, 65

Shibata, K., & Uchida, Y. 1985, PASJ, 37, 31

—. 1986, PASJ, 38, 631

Shu, F. H., Lizano, S., Ruden, S. P., & Najita, J. 1988, ApJL, 328, L19

Shu, F. H., Najita, J., Ostriker, E., Wilkin, F., Ruden, S. P., & Lizano, S. 1994, ApJ, 429, 781

Shu, F. H., Najita, J. R., Shang, H., & Li, Z.-Y. 2000, in Protostars and Planets IV, ed. V. Mannings, A. P. Boss, & S. S. Russell (Univ. Arizona Press, Tucson), p. 789

Shull, J. M., & Draine, B. T. 1987, in Astrophysics and Space Science Library, Vol. 134, Interstellar Processes, ed. D. J. Hollenbach & H. A. Thronson, Jr. (Reidel, Dordrecht), 283

Simon, J. B., Bai, X.-N., Armitage, P. J., Stone, J. M., & Beckwith, K. 2013, ApJ, 775, 73

Simon, J. B., Bai, X.-N., Flaherty, K. M., & Hughes, A. M. 2018, ApJ, 865, 10

Simon, J. B., Lesur, G., Kunz, M. W., & Armitage, P. J. 2015, MNRAS, 454, 1117

Simon, M. N., Pascucci, I., Edwards, S., Feng, W., Gorti, U., Hollenbach, D., Rigliaco, E., & Keane, J. T. 2016, ApJ, 831, 169

Skinner, S. L., Audard, M., & Güdel, M. 2011, ApJ, 737, 19

Stanke, T., McCaughrean, M. J., & Zinnecker, H. 2000, A&A, 355, 639

Stone, J. M., Ostriker, E. C., & Gammie, C. F. 1998, ApJL, 508, L99

Suriano, S. S., Li, Z.-Y., Krasnopolsky, R., & Shang, H. 2017, MNRAS, 468, 3850

—. 2018, MNRAS, 477, 1239

Suriano, S. S., Li, Z.-Y., Krasnopolsky, R., Suzuki, T. K., & Shang, H. 2019, MNRAS, 484, 107

Sutherland, R. 2010, Ap&SS, 327, 173

Suzuki, T., Kaneda, H., Onaka, T., Nakagawa, T., & Shibai, H. 2010, A&A, 521, A48

Suzuki, T. K., & Inutsuka, S.-I. 2009, ApJ, 691, L49

Suzuki, T. K., Muto, T., & Inutsuka, S.-I. 2010, ApJ, 718, 1289

Tabone, B., et al. 2017, A&A, 607, L6

Teitler, S. 2011, ApJ, 733, 57

Turner, N. J., Fromang, S., Gammie, C., Klahr, H., Lesur, G., Wardle, M., & Bai, X.-N. 2014, in Protostars and Planets VI, ed. H. Beuther, R. S. Klessen, C. P. Dullemond, & T. Henning (Univ. Arizona Press, Tucson), p. 411

Uchida, Y., & Shibata, K. 1985, PASJ, 37, 515

Umebayashi, T., & Nakano, T. 1981, PASJ, 33, 617

—. 1990, MNRAS, 243, 103

Urpin, V. 2003, A&A, 404, 397

Ustyugova, G. V., Koldoba, A. V., Romanova, M. M., Chechetkin, V. M., & Lovelace, R. V. E. 1995, ApJ, 439, L39

Vázquez-Semadeni, E. 1994, ApJ, 423, 681

Wada, K., & Norman, C. A. 2001, ApJ, 547, 172

Wagner, A., & Bicknell, G. 2011, ApJ, 728, 29

Wang, L., Bai, X.-N., & Goodman, J. 2019, ApJ, 874, 90

Wardle, M. 1997, in ASP Conf. Ser., Vol. 121, IAU Colloq. 163: Accretion Phenomena and Related Outflows, ed. D. T. Wickramasinghe, G. V. Bicknell, & L. Ferrario (Astron. Soc. Pac., San Francisco), p. 561

Wardle, M. 1999, MNRAS, 307, 849

Wardle, M. 2007, Ap&SS, 311, 35

Wardle, M., & Königl, A. 1993, ApJ, 410, 218

Wardle, M., & Ng, C. 1999, MNRAS, 303, 239

Wardle, M., & Salmeron, R. 2012, MNRAS, 422, 2737

Watson, D. M., et al. 2016, ApJ, 828, 52

Whelan, E. T., Ray, T. P., Bacciotti, F., Natta, A., Testi, L., & Randich, S. 2005, Nature, 435, 652

Whelan, E. T., Ray, T. P., Comeron, F., Bacciotti, F., & Kavanagh, P. J. 2012, ApJ, 761, 120

White, M. C., McGregor, P. J., Bicknell, G. V., Salmeron, R., & Beck, T. L. 2014, MNRAS, 441, 1681

Williams, J. P., & Cieza, L. 2011, ARA&A, 49, 67

Woitas, J., Ray, T. P., Bacciotti, F., Davis, C. J., & Eislöffel, J. 2002, ApJ, 580, 336

Wurster, J., Bate, M. R., & Price, D. J. 2018, MNRAS, 480, 4434

Zanni, C., Ferrari, A., Rosner, R., Bodo, G., & Massaglia, S. 2007, A&A, 469, 811

Zanni, C., & Ferreira, J. 2011, ApJ, 727, L22

—. 2013, A&A, 550, A99

Zhang, Q., Sridharan, T. K., Hunter, T. R., Chen, Y., Beuther, H., & Wyrowski, F. 2007, A&A, 470, 269

Zhang, Y., et al. 2018, ApJ, 864, 76

Zsom, A., Ormel, C. W., Dullemond, C. P., & Henning, T. 2011, A&A, 534, A73